$YBa_2Cu_3O_7$ Josephson Nano Devices Fabricated by Focused Helium Ion Beam Irradiation

Dissertation
der Mathematisch-Naturwissenschaftlichen Fakultät
der Eberhard Karls Universität Tübingen
zur Erlangung des Grades eines
Doktors der Naturwissenschaften
(Dr. rer. nat.)

vorgelegt von
Christoph Schmid
aus Lauingen a. d. Donau

Tübingen
2026

Gedruckt mit Genehmigung der Mathematisch-Naturwissenschaftlichen Fakultät der Eberhard Karls Universität Tübingen.

Tag der mündl. Qualifikation:	18.06.2026
Dekan:	Prof. Dr. Thilo Stehle
1. Berichterstatter:	Prof. Dr. Reinhold Kleiner
2. Berichterstatter:	Prof. Dr. Sebastian Kempf

Abstract

Superconducting electronics enables quantum-accurate metrology, ultra-sensitive magnetometry, and terahertz (THz) devices. The established Nb technologies are constrained by a low operating temperature and a limited high-field/high-frequency performance. In the framework of this dissertation, a fabrication platform for high-transition-temperature superconducting nano-devices based on epitaxially grown $YBa_2Cu_3O_7$ (YBCO) films patterned by focused helium-ion-beam (He-FIB) irradiation is described. He-FIB irradiation locally displaces oxygen atoms in YBCO and allows to continuously tune the superconducting properties without material removal, enabling direct-write creation of weak links, resistive regions, and insulating barriers with nanometer-scale precision.

This thesis accumulates four publications that together provide a deeper insight into the well-established barrier-type Josephson junction and a spectrum of applications. Single JJs and JJ arrays embedded in antenna structures are presented to realize a THz detector, which could lay the foundation of a high-transition-temperature voltage standard. Furthermore, a superconducting diode with record figures of merit is presented. To broaden the range of possible applications, He-FIB induced YBCO resistors are presented, which allow for the fabrication of nano constriction-type Josephson junctions on the resolution limit of the He-FIB. These ultra-small junctions are investigated in SQUIDs and THz antennas to demonstrate their feasibility.

Kurzfassung

Supraleitende Bauelemente ermöglichen quantengenaue Metrologie, hochempfindliche Magnetometrie und Terahertz-Anwendungen. Etablierte Niob-Technologien sind jedoch durch niedrige Betriebstemperaturen sowie eine begrenzte Verwendbarkeit bei hohen Magnetfeldern oder hohen Frequenzen eingeschränkt. Diese Dissertation entwickelt eine Fertigungsplattform für Hochtemperatursupraleiter zu Realisierung von Nanobauelementen auf Basis von epitaktischem $YBa_2Cu_3O_7$ (YBCO), strukturiert mittels Bestrahlung eines fokussierten Helium-Ionenstrahls (He-FIB). He-FIB-Bestrahlung deplatziert in YBCO lokal Sauerstoffatome und beeinflusst dadurch die supraleitenden Eigenschaften im bestrahlten Bereich. Dies ermöglicht die Fabrikation von Josephson Barrieren, resistiven Bereichen und isolierenden Barrieren mit nanometergenauer Präzision.

Die Arbeit umfasst vier Publikationen, die gemeinsam ein vertiefendes Verständnis der bereits etablierten Fabrikation von Barrieren-Josephson-Kontakten in YBCO und einigen Anwendungen liefern. Einzelne Josephson-Kontakte und Josephson-Kontakt-Arrays werden in Antennenstrukturen integriert, um einen Terahertz (THz)-Detektor zu realisieren, welcher die Grundlage für einen zukünftigen Hochtemperatursupraleiter-Spannungsstandard legen könnte. Darüber hinaus wird eine durch He-FIB-Bestrahlung induzierte supraleitende Diode mit herausragenden Spezifikationen vorgestellt. Zur Erweiterung der Bandbreite möglicher Anwendungen dienen He-FIB-induzierte YBCO-Widerstände, die den Weg zu Nano-Josephson-Kontakten an der Auflösungsgrenze des He-FIB geebnet haben. Diese ultrakleinen Kontakte werden in SQUIDs und THz-Antennen getestet, um ihre Realisierbarkeit zu demonstrieren.

List of publications

This is a cumulative thesis based on the work published in the four papers listed below. Publication 1 and 2 describe basic properties and parameter spread of so-called barrier Josephson junctions fabricated by He-FIB irradiation. Both work towards an implementation of a high-critical-temperature voltage standard using a Josephson junction array embedded in antenna structures. Publication 3 utilizes the barrier writing process to fabricate a superconducting diode with record figures of merit. The first realization of a constriction-type Josephson junction in YBCO is demonstrated in Publication 4. All publications are attached at the end of the thesis.

Appended publications

Publication 1 M. Pröpper, D. Hanisch, **C. Schmid**, P. J. Ritter, M. Neumann, E. Goldobin, D. Koelle, R. Kleiner, M. Schilling, B. Hampel
THz Properties of He-FIB $YBa_2Cu_3O_{7-x}$ Josephson Junctions
IEEE Trans. Appl. Supercond. **34**, 1100505 (2024)

Publication 2 M. Pröpper, D. Hanisch, **C. Schmid**, M. Neumann, P. J. Ritter, M.-A. Tucholke, E. Goldobin, D. Koelle, R. Kleiner, M. Schilling, B. Hampel
High-T_c Josephson Junction Arrays Fabricated by He-FIB
IEEE Trans. Appl. Supercond. **35**, 1100105 (2025)

Publication 3 **C. Schmid**, A. Jozani, R. Kleiner, D. Koelle, E. Goldobin
$YBa_2Cu_3O_7$ Josephson diode fabricated by focused-helium-ion-beam irradiation
Phys. Rev. Appl. **24**, 014041 (2025)

Publication 4 **C. Schmid**, C. Buckreus, D. Haas, M. Pröpper, R. Hutt, C. Magén, D. Hanisch, M. Karrer, M. Schilling, D. Koelle, R. Kleiner, E. Goldobin
$YBa_2Cu_3O_7$ nano-constriction Josephson junctions and SQUIDs fabricated by focused helium-ion-beam irradiation
arXiv:2511.19197 (2025)

Publications not included in this thesis

Publication 5 M. Karrer, B. Aichner, K. Wurster, C. Magén, **C. Schmid**, R. Hutt, B. Budinská, O. V. Dobrovolskiy, R. Kleiner, W. Lang, E. Goldobin, D. Koelle
Vortex matching at 6 T in $YBa_2Cu_3O_{7-\delta}$ thin films by imprinting a 20-nm periodic pinning array with a focused helium-ion beam
Phys. Rev. Appl. **22**, 014043 (2024)

Publication 6 F. Tahouni-Bonab, M. Hepting, T. Luibrand, G. Cristiani, **C. Schmid**, G. Logvenov, B. Keimer, R. Kleiner, D. Koelle, S. Guénon
Nonvolatile multistate electrothermal resistive switching in a strongly correlated insulator thin-film device
Phys. Rev. Appl. **24**, 034014 (2025)

Publication 7 M. Pröpper, M.-A. Tucholke, D. Hanisch, **C. Schmid**, P. J. Ritter, M. Neumann, E. Goldobin, D. Koelle, R. Kleiner, M. Schilling, B. Hampel
Shunting $YBa_2Cu_3O_{7-x}$ Josephson Junctions and Arrays Fabricated by He-FIB
IEEE Trans. Appl. Supercond. **36**, 1100206 (2025)

Publication 8 M. Pröpper, M.-A. Tucholke, **C. Schmid**, O. Kieler, M. Neumann, P. J. Ritter, E. Goldobin, D. Koelle, R. Kleiner, M. Schilling, B. Hampel
Toward a Voltage Standard using $YBa_2Cu_3O_{7-x}$ *Josephson Junction Arrays Fabricated by He-FIB*
IEEE Trans. Appl. Supercond. **36**, 1400106 (2026)

Publication 9 T. Cosgrove, M. Pröpper, **C. Schmid**, E. Goldobin, D. Koelle, R. Kleiner, M. Schilling, B. Hampel, R. Taylor
Design and Performance of a 10-GHz HTS He-FIB JJ Mixer on LSAT
IEEE Trans. Appl. Supercond. **36**, 1400106 (2026)

Publication 10 K. Fohmann, T. J. Glebe-Märklin, B. Wilde, M. Kazouini, **C. Schmid**, D. Koelle, R. Kleiner, D. Bothner
Dually tunable YBCO coplanar waveguide resonators based on helium-ion-generated Josephson inductances
arXiv:2605.30425 (2026)

Publication 11 B. Aichner, S. Koch, P. A. Korner, M. Karrer, K. Wurster, **C. Schmid**, U. Kentsch, R. Kleiner, E. Goldobin, D. Koelle, W. Lang
Tailoring the properties of $YBa_2Cu_3O_{7-x}$ *thin films by 30 keV* He^+ *irradiation: An enabling route to superconducting device nanopatterning*
arXiv:2606.14588 (2026)

Contents

List of Acronyms

ac alternating current

AIBs amorphous insulating barriers

bJJ barrier Josephson junction

cJJ constriction Josephson junction

CPR current–phase relation

dc direct current

EBL electron-beam lithography

He-FIB helium focused ion beam

HTS high-temperature superconductor

IVC current-voltage characteristics

JJ Josephson junction

nanoSQUID nanoscale SQUID

RSJ resistively shunted junction

ScD superconducting diode

SQUID superconducting quantum interference device

YBCO $YBa_2Cu_3O_{7-x}$

1 Introduction

Superconducting electronics has evolved from a niche subfield of low-temperature physics into a central technology platform for precision metrology, quantum information processing, and high-sensitivity detection. A decisive step was the discovery of the Josephson effect in 1962[1]. It showed that a macroscopic quantum phase difference between two superconductors separated by a weak link gives rise to a dissipationless supercurrent and characteristic dynamical phenomena. The resulting device, the Josephson junction (JJ), rapidly became a standard building block of superconducting circuits[2]. Today, Josephson junctions underpin technologies ranging from Josephson voltage standards[3,4] and ultra-sensitive superconducting interference device (SQUID) magnetometers[5,6] to superconducting qubits[7], parametric amplifiers[8], and terahertz (THz) detectors[9].

The broader significance of JJ-based devices is reflected in major scientific milestones, including the demonstration of macroscopic quantum tunneling and quantized energy levels in superconducting circuits by Devoret, Martinis, and Clarke[10–12], which was honored with the last year's Nobel prize in physics. These experiments showed that superconducting circuits may behave as macroscopic quantum systems, laying the foundation for quantum information technologies and reinforcing the central role of the Josephson junction in modern quantum science[13,14]. As research pushes toward higher frequencies, stronger magnetic fields, and more complex architectures, the requirements for Josephson-junction materials and fabrication techniques rise in step. Among the most significant application domains driving these developments are nanoscale SQUID (nanoSQUID) magnetometry, nonreciprocal superconducting circuits, and THz devices[15–17].

Direct current (dc) SQUIDs, consisting of a superconducting ring intersected by two Josephson junctions, sketched in Fig. 1.1(a), form the basis of an ultra-sensitive flux sensing device. To operate the device, a dc bias is applied. Any flux, penetrating the SQUID hole induces currents in the superconducting ring, which modulate the junctions critical currents, whereas the SQUID switches from superconducting to the voltage state.

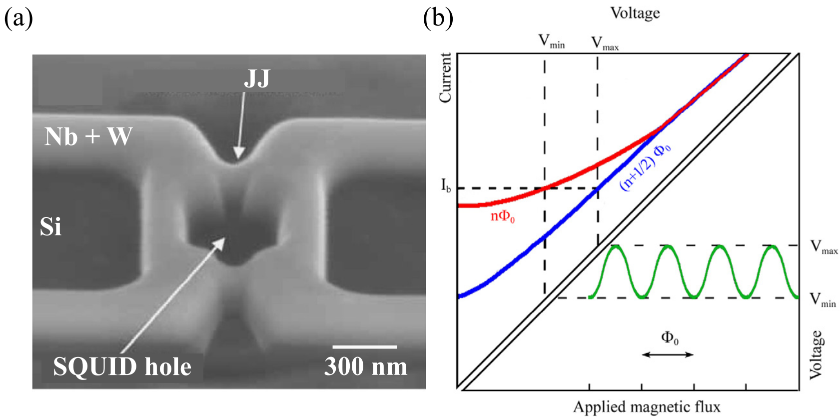

Figure 1.1: (a) Scanning electron micrograph of a W-covered Nb dc SQUID with two nanojunctions patterned in the SQUID loop. (b) The upper left part shows current-voltage characteristics of a dc SQUID for applied flux of $\Phi_0/2$ and Φ_0 threading the SQUID loop. For a fixed current bias (flowing from left to right in (a)) the resulting voltage modulation with applied magnetic flux is depicted in the lower right part of the figure. The figures are reprinted from Ref.[18], with permission from Elsevier.

This happens due to fluxoid quantization in the superconducting ring and the non-linearity of the Josephson junctions. For a fixed bias current, the SQUID shows a modulating voltage V dependent on the applied flux Φ, see Fig.1.1(b). The point of maximum slope in the $V(\Phi)$-curve corresponds to the device's highest sensitivity and thus defines the preferred operating point. Readout electronics, such as flux-locked loop, allow to operate at this very point over huge changes in the penetrating flux by feeding back flux to the SQUID. This offers unparalleled magnetic-flux sensitivity, where optimized SQUIDs rms flux noise can reach down to $1\,\mu\Phi_0/\sqrt{\mathrm{Hz}}$ or lower[18–20], enabling applications ranging from scanning probe microscopy to biomagnetic detection and geophysical surveying[21]. Continued advances in nanoscale SQUIDs have pushed sensitivities toward the single-spin regime while enabling sub-100-nm spatial resolution using SQUID-on-

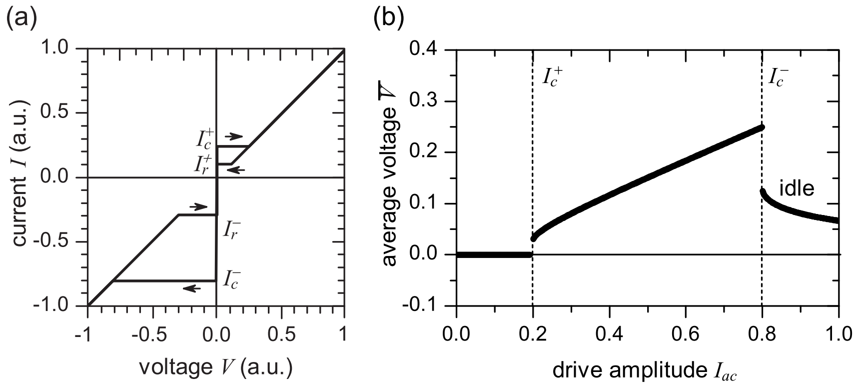

Figure 1.2: (a) Modeled IVC featuring a linear voltage branch with a slope of $1/R_\mathrm{n}$. The critical currents used for plotting are $I_\mathrm{c}{}^+ = 0.2$, $I_\mathrm{c}{}^- = 0.8$, $I_\mathrm{r}^+ = 0.1$ and $I_\mathrm{r}^- = 0.3$. (b) Rectification curve acquired by applying a sinusoidal driving current with the form of $I = I_\mathrm{ac}\,\sin(\omega t)$ to the IVC in (a). Averaging over one period of the driving current at an amplitude I_ac in (a) yields one data point in (b). The dashed lines indicate the switching currents from the IVC in (a). The range between the dashed lines defines the rectification window, in which the device operates as a superconducting diode the most efficiently. Both graphs are adapted from Ref. [26] and modified. © 2016 American Physical Society.

tip devices[22,23]. Major progress has also come from integrating these nano-SQUIDs into scanning cantilevers, allowing simultaneous atomic-force microscopy operation and magnetic imaging, and even mapping local temperature variations of the sample. This SQUID-on-lever technology was successfully integrated on the Nb platform within an European collaborative project known as FIBsuperprobes[24,25]. The reported Nb device realized remain challenged by temperatures above ten kelvin, magnetic fields of several tesla, and scaling constraints, which gives rise to another material platform for further optimization.

At the same time, interest in engineered nonreciprocity has revived research on Josephson devices whose critical currents depend on the current direction. Such devices, nowadays reffered to as superconducting diodes

(ScDs), characterized by $I_{c,+} \neq I_{c,-}$ (see Fig.1.2(a)), represent a promising building block for nonreciprocal superconducting circuits. To achieve a ScD, one has to enforce both time reversal and inversion symmetry breaking within the Josephson junction, which generally follows from an asymmetric current-phase relation[27]. This can be accomplished through several distinct mechanisms. Experimental realizations include spin–orbit coupling combined with Zeeman fields[28], field-free symmetry breaking in van der Waals heterostructures[29], fluxon-induced Josephson potential asymmetry[30], asymmetric SQUID potentials[31–33], and many more[16,34]. To exemplify the working principle of the ScD, one can simply drive such a device with an alternating or even a noise current source and measure the rectified dc voltage, see Fig. 1.2(b). For testing the conversion efficiency of the diode, an additional counter current can be applied, which weakens the diode effect and reveals its performance under load[26]. These demonstrations highlight the technological potential of ScDs leading to superconducting electronics in the form of computer chips, direction-selective quantum sensors, rectifiers and other quantum devices[27]. It also raises the question whether a purely noise-driven rectifier can be used to generate energy. Typically the reported ScDs rely on low-critical-temperatures (low-T_c) materials or complex multilayer heterostructures and face challenges in scalability, with the exception of asymmetric SQUIDs realized in YBCO[31,35]. Mostly they present ratios of the critical currents of a factor three or smaller. This motivates the search for Josephson diodes based on high-T_c superconductors and more scalable architectures.

A further major application area lies in Josephson-based THz detection and mixing. THz frequencies, normally defined in the range of 0.1 THz to 10 THz, which has been pursued since the early days of superconducting electronics[36,37]. Furthermore, the ac Josephson effect builds the fundamental metrology unit volt in the International System of Units[4]. The gauge experiment emphasizes thousands of junctions connected in series to generate a huge voltage output signal with low noise properties, excited at frequencies of several tens of GHz[38]. The linear relation between the excitation frequency f and the voltage drop V across the devices is determined solely by the fundamental constant of the flux quantum Φ_0:

$$f = \frac{V}{\Phi_0}. \tag{1.1}$$

The number of JJs required to reach a certain voltage can be reduced by employing higher excitation frequencies, for instance in the terahertz range. Therefore, excitation frequencies reaching the THz regime are desirable. High-T_c superconductors offer intrinsic advantages in this frequency range. Due to their huge energy gap, corresponding to the maximum voltage applicable without Cooper pair breaking, higher excitation frequencies compared to low-T_c superconductors are achievable, see Eq. (1.1). Moreover, operating such detectors in the 40 K to 77 K range, rather than at 4 K, substantially simplifies cryogenic system design and expands their potential for portable or space-based applications[39].

Historically, these diverse application domains have mainly relied on Nb as the material platform of choice. For more than four decades, Nb thin-film technology has provided excellent uniformity, compatibility with multilayer processing, and stable oxide barriers[40]. Standard Nb/AlO_x/Nb tunnel junctions provide well-controlled current-voltage characteristics (IVCs), predictable critical current densities j_c, and compatibility with large-scale superconducting integrated circuits[41,42]. A lot of applications like SQUIDs[5], logic families (RSFQ, RQL)[43], and metrological Josephson arrays[4] continue to rely on this robust technology.

Nevertheless, Nb suffers from intrinsic limitations. Its critical temperature of $T_c \approx 9.2$ K restricts operation to liquid-helium temperatures. Although modern cryocoolers can reach 4 K, the associated power consumption, size, and vibration mitigation remain significant obstacles for portable devices. Operation at temperatures above 20 K, achievable with more compact and efficient cryocoolers, is therefore technologically attractive[39]. Another key constraint of Nb thin-film Josephson technology is its restricted robustness in applied magnetic fields. For operation in high magnetic fields, the film thickness has to be reduced which comes with major drawbacks in e.g. the noise performance of a SQUID[44]. High-T_c YBCO, with much higher field tolerance, is therefore particularly attractive for applications requiring operation in the tesla regime.

These limitations motivate the exploration of superconductors with higher critical temperatures, higher critical magnetic fields, and large depairing current densities. $YBa_2Cu_3O_7$ (YBCO), with $T_c \approx 90\,K$, is a promising candidate. It enables operation in the technologically attractive temperature range up to several tens of kelvin, supports large critical current densities up to $90\,MA/cm^2$, maintains robust superconductivity in high magnetic fields of several tens of tesla[45–47]. These properties promise advantages for e.g. nanoscale devices, THz detectors, and diode-like Josephson applications. The first successful attempts of realizing a JJ by integrating a barrier in YBCO incorporated grain-boundary, ramp-edge and planar-sandwich type JJs[48]. Grain-boundary Josephson junctions[49–51] enabled high-T_c SQUIDs at 77 K. These techniques suffer from parameter scatter and possess limited scalability due to the decreased j_c caused by the barrier. Early attempts of YBCO nanowires and Dayem bridges, fabricated by electron-beam lithography (EBL) and ion milling[52–54], enabled structures with widths below 200 nm. A major breakthrough by the Chalmers group demonstrating reproducible nanowires as narrow as 40 nm[55–60] and later grooved Dayem bridges[61] set the limits of nanostructuring so far. Interestingly, a protective encapsulation has improved environmental robustness[62], but etch-induced damage and oxygen loss continue to limit reproducibility of device structures below $\sim 50\,nm$.

Parallel developments in low-T_c nanoSQUIDs have achieved single-spin sensitivity using constriction-type Josephson junctions or three-dimensional nanobridges[22,23,63]. Achieving similar nanoscale control in YBCO, while leveraging its higher operating temperature and superior magnetic field tolerance, remains an open challenge.

Recent work has demonstrated that focused helium ion beam (He-FIB) irradiation provides a powerful approach to overcome the fabrication bottlenecks of nanopatterning YBCO [64–66]. By 30 keV focused He^+ beam irradiation, the chain oxygen atoms in YBCO get locally displaced, enabling direct-write tuning of superconductivity without material removal[67]. On the large scale, this was already shown in the pre-era of the He-FIB, realized with a He^+ implanter[68,69]. By controlling the irradiation dose, the properties of YBCO can be continuously transformed from superconducting to insulating state, see Fig. 2.9. The few-nanometer beam spot

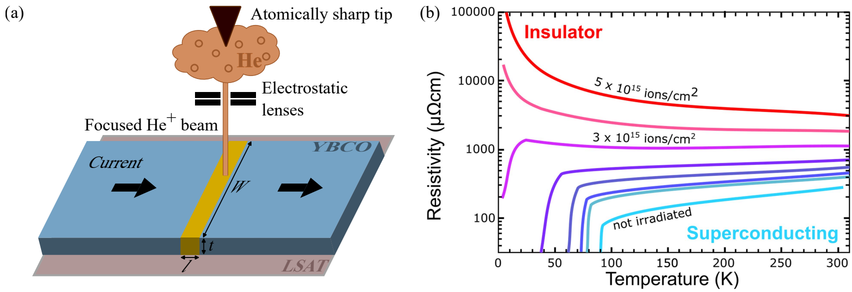

Figure 1.3: (a) Schematic of the He-FIB, irradiating a YBCO microbridge. The yellow area indicates the area which is irradiated be the He ions. (b) Temperature dependence of the resistivity of a 75 keV He^+-implanter irradiated YBCO thin film for various doses. The irradiation area is 50 x 50 mm^2 at a film thickness of 100 nm. By varying the dose, the resistivity can be systematically tuned from superconducting to insulating state. (b) is adapted from Ref. [70]. © 2023 IEEE.

size of the He-FIB and minimal lateral damage enable the patterning of Josephson barriers and insulating trenches with unequalled resolution[65]. This approach allows the realization of Josephson devices such as JJs and SQUIDs[65] and expands possibly in further electrical components like resistors, inductors and capacitors[70]. Several studies have successfully realized planar Josephson junctions and e.g. nanoSQUIDs entirely fabricated by He-FIB patterning, highlighting its promise for scalable, high-precision YBCO nanostructures[65,71–75].

Despite this progress, the fabrication of He-FIB induced barrier Josephson junctions (bJJ) exhibiting reproducible junction parameters remain challenging. In the beginning, the technology faced a problem of persistent change in Josephson parameter after device fabrication. This issue was successfully addressed by an additional annealing step in a subsequent process[76]. The progress in pushing device scale down to 10 nm is still ongoing, while state-of-the-art He-FIB nano bJJs[66] are stuck at the same limit as EBL structured JJs[60].

This thesis focuses on the favorable high-T_c superconductor YBCO and the novel fabrication technique of He-FIB irradiation to tackle the limits of state-of-the-art superconducting devices. **Publication 1**, emphasizes the huge advantage of He-FIB patterned bJJs in YBCO by presenting the critical current I_c and the normal state resistance R_n dependence on the irradiation dose. Consequently, the size and the junction parameters I_c and R_n are easily adaptable to the device design, highlighting the flexibility of this fabrication technique. The designated goal is to realize a THz detector in a high-T_c superconductor using a bJJ. The realization of a high-T_c THz detector has already been successfully implemented using grain-boundary JJs[77], which motivates to establish high-T_c superconductors for the voltage standard. He-FIB irradiation offers substantial benefits for device miniaturization and design flexibility, as it enables arbitrary nanoscale positioning and size of the irradiated regions. This motivates the goal of realizing comparable results using bJJs, which is achieved by integrating such bJJs into the feedpoint of a lithographically microstructured antenna design.

To optimize coupling efficiency, the aim is to match junction and antenna impedances, while maintaining a high critical current required for large Shapiro steps. Further, the publication investigates the characteristic frequency f_c dependence on the irradiation dose. Conclusively, the junction response to microwave and THz radiation is demonstrated by clear Shapiro steps at frequencies up to 1.4 THz. Building on this results, **Publication 2**, extends the scope from individual devices to large-scale arrays aimed at improving quantum-based voltage standards. Here, a meander structure comprising 79 YBCO Josephson junctions, all fabricated with the same He-FIB dose, is realized. The work addresses a subtle fact about reproducibility of the He-FIB irradiation technique, which has been never discussed in detail in prior studies. The fabrication process exhibits a considerable spread in the junction parameters, which underlying origin is not yet fully understood. The statistical spread of I_c and R_n across the array at5 K is presented and quantified. Measuring subsets of junctions whose parameters match within the few-percent level required for coherent operation show promising results. The arrays are driven with GHz and THz radiation at 20 K, revealing synchronized Shapiro steps originating from multiple junctions. This is highly promising for metrological applications enabling a voltage standard operable at THz frequencies and temperatures of several tens of kelvin.

Publication 3 exploits He-FIB nanostructuring to realize a high-T_c Josephson diode with strongly nonreciprocal critical currents. The device is based on an in-line YBCO Josephson junction where the bias current flows in line to the JJ barrier length. By He-FIB irradiation the Josephson barrier and insulating barriers in a single-layer superconductor are created. The insulating barriers shape the current path in a way that the bias current induces a magnetic self-field to the JJ that gives rise to the diode effect. Utilizing this unique geometry in combination with an external magnetic field, a Josephson diode is realized that outperforms previously reported devices in terms of asymmetry and output power. Integrating this concept in a high-T_c superconductor opens new prospects for a noise-driven superconducting diode, as demonstrated by simulations. Within these noteworty results, the miniaturization limits were pushed further, achieving device areas below $1\,\mu m^2$.

Publication 4 shifts the focus to barrierless constriction Josephson junctions (cJJs) to push the boundaries of miniaturization. Starting from epitaxial YBCO films, normal-conducting regions are defined using tailored He-FIB doses, resulting in YBCO resistors. This approach allows the fabrication of nanometer-wide superconducting constrictions between irradiated regions. The work demonstrates cJJs with lateral dimensions down to the order of ten nanometer or even below, operable up to the boiling point of liquid nitrogen (77 K). The successful incorporation of such cJJs in nanoSQUIDs and THz antennas highlights the potential of a new state-of-the-art fabrication process to realize nano-devices.

Taken together, these four publications advance the state-of-the-art fabrication methods in several directions. The results demonstrate that He-FIB nanopatterning enables deterministic control of YBCO Josephson junction parameters from the single-junction to the array level. They show that both barrier-type and constriction-type Josephson junction can be integrated into nanoSQUIDs and THz antenna structures, providing a high-T_c Josephson diode with competitive figures of merit.

2 Summary of publications and contributions

2.1 Publication 1: THz Properties of He-FIB $YBa_2Cu_3O_{7-x}$ Josephson Junctions

This publication focuses on the ability of a He-FIB induced JJ in YBCO, working as a detector for electromagnetic waves in the THz regime. Furthermore, the dependency of the dose on the electrical properties are investigated, which supports the findings of earlier reports[65].

Due to both the high energy gap of YBCO[78] and the large $I_c R_n$ product of YBCO JJs[65], the material exhibits notable capability to operate at frequencies in the THz range[79,80]. The high critical temperature of YBCO also offers the benefit of lower cooling requirements compared to low-T_c superconductors.

Barrier-type JJs were embedded in 3 µm-wide prepatterned microbridges, fabricated with different irradiation doses. With a four-terminal sensing scheme, IVCs were measured at 5 K. Extracting I_c and R_n in the linear regime of the IVC, their dependence ofn the He-FIB dose can be investigated, see Fig. 2.1. On a linear scale for I_c and R_n , the dose dependence emerges exponentially and inverse exponentially, respectively. This supports earlier findings about He-FIB structured bJJs[65]. Furthermore, a scaling of the $I_c R_n$ product with the critical current density j_c of $j_c^{0.5\pm0.1}$ is observed, supporting the commonly reported behavior of YBCO JJs[48]. Figure 2.1 already indicates parameter scatter associated with the He-FIB fabrication technique of JJs. Investigation of the temperature dependence shows, that the resistance remains nearly constant, while the critical current decreases with increasing temperature. This feature can be practically used to tune I_c or $I_c R_n$ of the bJJs to adapt them to measurement requirements. Operating temperatures of ≈ 50 K seem to be realizable with the He-FIB fabricated JJs.

This preliminary test was used subsequently to determine the optimum fabrication parameters for realizing a bJJ suitable for THz detection. The high $I_c R_n$ product, as derived from the data, already indicates the suitability of these junctions for THz applications. The characteristic

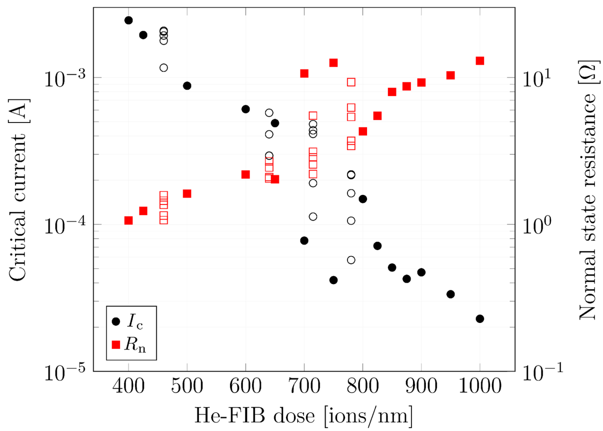

Figure 2.1: I_c (circles) and R_n (squares) values of the 3 µm-wide YBCO junctions for different doses. To investigate in the junction parameter spread, subsets of devices were irradiated with the same dose (open symbols). The measurements were performed at 5 K. © 2024 IEEE.

frequency of the JJ can be easily obtained with

$$f_c = \frac{2\, e\, I_c\, R_n}{h}, \tag{2.1}$$

including the elementary charge e and Planck's constant h. Using a range of JJs integrated in microbridges, transport measurements under microwave excitation were performed, revealing flat and wide Shapiro steps. Under THz excitation, either no detection or only barely significant signals are measured. However, embedding the bJJs in u-shaped antennas optimized for coupling THz signals showed a huge improvement of the coupling efficiency. At 1, 1.3 and 1.4 THz, a strong excitation signal in the form of Shapiro steps in the IVCs is observed, cf. Fig.2.2. This results support to the feasibility of He-FIB fabricated JJs building a high-T_c voltage standard.

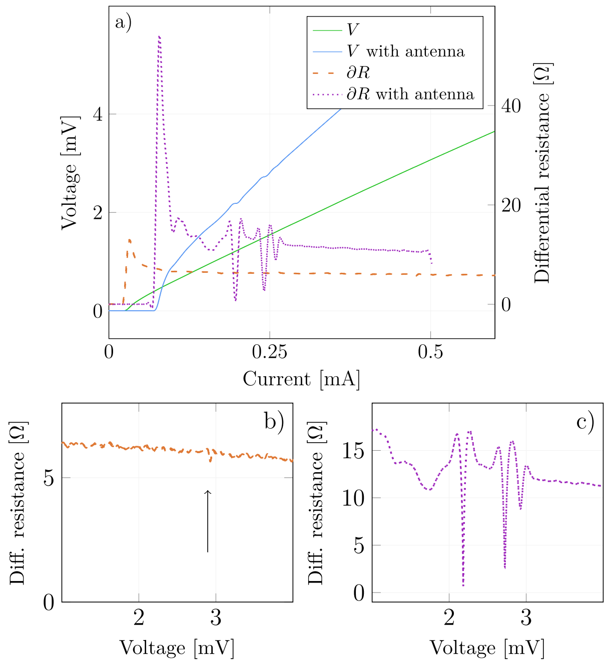

Figure 2.2: (a) Comparison of the irradiation of a single Josephson junction with and without a u-shaped antenna at 20 K. (b) and (c) show enlarged views of the differential resistance versus voltage curves without and with antenna over the investigated frequency range 1 THz, 1.3 THz and 1.4 THz. The arrow in (b) marks the little dip which is caused by the 1.4 THz excitation of the laser. © 2024 IEEE.

Contributions

This work was carried out in cooperation with M. Pröpper, D. Hanisch, P. J. Ritter, M. Neumann, E. Goldobin, D. Koelle, R. Kleiner, M. Schilling, B. Hampel. The chip fabrication, microstructuring, characterization of the devices, evaluation of the data and manuscript preparation was done by the group of TU Braunschweig. I contributed by supporting the layout design, inducing JJs by He-FIB to finalize the devices and participated in several constructive meetings to discuss the projects issues, further improvement and research goals.

2.2 Publication 2: High-T_c Josephson Junction Arrays Fabricated by He-FIB

This publication presents progress towards a voltage standard based on the high-T_c superconductor YBCO under THz excitation. Due to their large superconducting energy gap and its high critical temperature, YBCO-based devices are operable under higher excitation frequencies and therefore require fewer JJs while reducing the need for extensive cooling. In addition, the parameter spread of He-FIB–induced bJJs are investigated.

State-of-the-art voltage standards at NIST and PTB rely on Nb-based JJ technology[3,4]. These systems employ thousands of junctions operated at excitation frequencies of several tens of GHz to generate output voltages of several volts at 4.2 K[38]. This correlation is expressed in the following equation

$$V = n\frac{h}{2\,e}f, \tag{2.2}$$

where f the applied frequency and n either the harmonic number of the Shapiro step or the number of JJs connected in series. Clearly, achieving high output voltages requires either a large number of Josephson junctions or a high excitation frequency. The presentation of a voltage standard using the beneficial high-T_c properties of YBCO were already highlighted by Klushin et al.[77]. Using a YBCO JJ array comprising 620 grain-boundary junctions, they demonstrated voltage steps up to 100 µV at approximately 79 K under excitation frequencies of several tens of GHz.

In this work, a 50 nm-thick YBCO thin film was patterned into a meandering microstrip connecting seventy-nine 2 µm-wide microbridges in series. Additional leads attached to the turns of the meander enable voltage sensing and current biasing either individually or across arbitrary subsets of neighboring JJs, see Fig. 2.3. Each microbridge was irradiated with a single He-FIB line at a dose of 695 ions/nm to induce a Josephson barrier. This value was determined based on the previously reported exponential dependence of bJJ parameters on the irradiation dose[65] and extrapolated from earlier studies on similar samples in **Publication 1**.

In the single-line irradiation approach, individual pixels are scanned with a defined dwell time and pitch. To minimize the effects of thermal

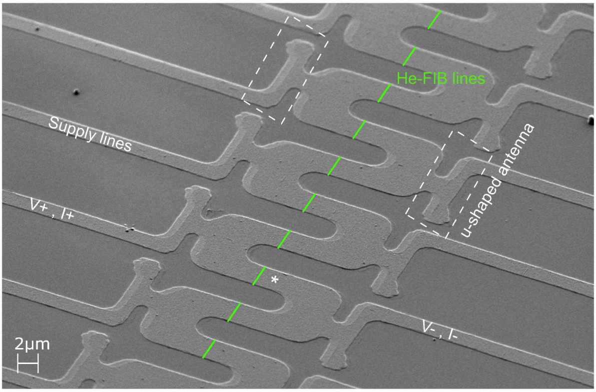

Figure 2.3: Scanning electron micrograph of the meander structure composed of of 2 µm-wide and 10 µm-long YBCO microbridges. The green lines indicate the He-FIB–irradiated regions. For illustration, the voltage and current connections for the four-terminal measurement of the JJ marked with an asterisk are shown.

stage drift (1 nm/s), each pixel was irradiated only once. This strategy prevents lateral smearing of the irradiated region, although minor line bending can still occur in extreme cases.

The large number of fabricated He-FIB JJs provides valuable insight into the parameter variation inherent to this fabrication technique, see Fig. 2.4. The mean values of the critical current and normal resistance were determined as $I_c = 120\,\mu A$ and $R_n = 5.4\,\Omega$, respectively. The corresponding standard deviations were $\sigma_{I_c} = 78\,\mu A$ (60%) and $\sigma_{R_n} = 1.25\,\Omega$ (25%). This parameter spread is roughly twice as large as those reported in previous studies[81,82]. However, the spread in these reports was estimated by simulations based on a single IVC of the entire array measured at 77 K, rather than from individual junction IVCs obtained at 5 K. Due to noise rounding of the IVCs, the I_c values are less distinguishable.[83].

During patterning, the He-FIB focus was readjusted after every five junctions, which could introduce slight variations due to human-induced

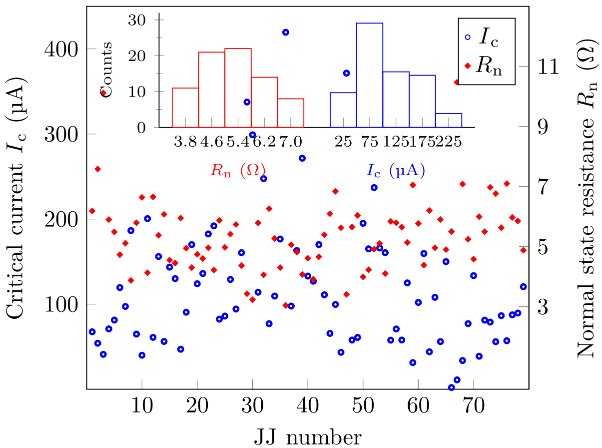

Figure 2.4: Critical current (I_c) and normal resistance (R_n) of individual JJs in the meander array as a function of junction number at 5 K. The inset shows the corresponding histograms of both parameter distributions. © 2025 IEEE.

systematic errors. However, a statistical comparison of these five-JJ groups with the overall dataset revealed no significant correlations.

To achieve a substantial output voltage, many JJs must contribute coherently to the measured signal. Substantial overlap of Shapiro steps requires identical voltage drops over a specific current range, highlighting uniform junction properties as a key challenge for high-T_c technology. To address this, sub-arrays with less than 10% parameter spread were selected. Despite their similar dc characteristics, their response to microwave excitation varied noticeably. The best-performing two-JJ array exhibited superimposed Shapiro steps up to 165 µV at 20 K.

A three-JJ sub-array was further investigated under THz excitation at 1.04 THz and 20 K. Differential resistance data obtained from the IVCs show a distinct dip at the expected voltage of 6.45 mV shown in Fig. 2.5, confirming the array's response to THz irradiation.

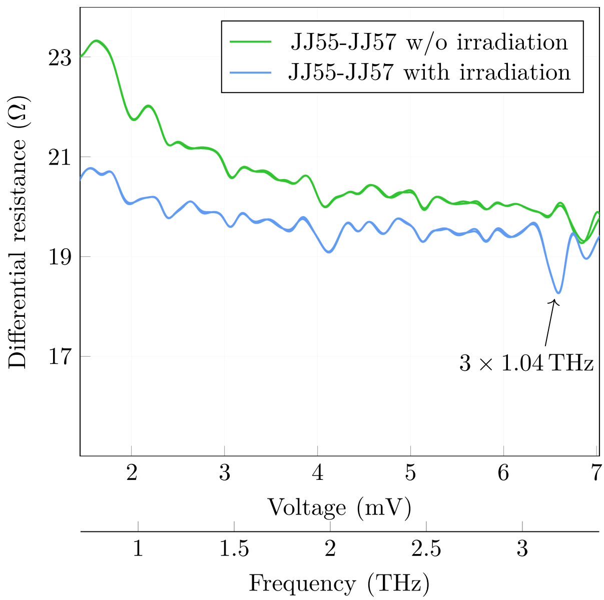

Figure 2.5: Back and forth sweep of differential resistance is plotted versus the frequency. The frequency is obtained by the measured voltage, whereas the differential resistance is extracted from an IVC measurement. The plot compares the data of a three-JJ array with and without THz irradiation, measured at20 K. The dip in the blue curve indicates the synchronization of the three JJs. © 2025 IEEE.

Contributions

This work carried out in cooperation with M. Pröpper, D. Hanisch, M. Neumann, P. J. Ritter, M.-A. Tucholke, E. Goldobin, D. Koelle, R. Kleiner, M. Schilling and B. Hampel. The chip design, fabrication, microstructuring, measurements and manuscript preparation were performed by the group of TU Braunschweig. My contribution comprised the He-FIB patterning of all junctions as well as providing conceptual input and guidance on the realization and optimization of the devices.

2.3 Publication 3: $YBa_2Cu_3O_{7-x}$ Josephson diode fabricated by focused-helium-ion-beam irradiation

This publication presents the realization of a sub-μm Josephson diode in the high-T_c superconductor YBCO, exhibiting a remarkable asymmetry value $\mathcal{A}$, defined as the ratio between negative and positive critical currents. The diode was fabricated in a single irradiation step, leveraging the versatility of the He-FIB for both nanopatterning and creating barrier junctions.

Barone and Paternò previously suggested that feeding a bias current along a meandering path with a Josephson junction of length l, placed at the turning point, will induce a self-field effect on the junction[2]. This leads, even at zero-field to a non-uniform phase distribution along the junction, resulting in a skewed I_c versus field modulation. Let's consider the invariant phase difference at a position x along a short JJ ($l < 4\lambda_J$), where λ_J is the Josephson penetration depth,

$$\phi(x) = \frac{2\pi}{\Phi_0} d_{\text{eff}}\, B\, x = 2\pi f\, \frac{x}{l}. \tag{2.3}$$

Here, $\Phi = B d_{\text{eff}}\, l$ is the total magnetic flux threading the JJ, where d_{eff} is the effective thickness of the barrier. $f = f_\Phi = \frac{\Phi}{\Phi_0}$ is the normalized flux in the case of a simple JJ without any special geometry. This expression leads to the typical Fraunhofer pattern in the I_c versus flux modulation.

$$\phi(x) = \frac{2\pi}{\Phi_0} d_{\text{eff}}\, B\, x = 2\pi f\, \frac{x}{l}. \tag{2.4}$$

Here, $f = f_\Phi = \frac{\Phi}{\Phi_0}$ is the normalized flux in the case of a simple JJ without any special geometry. $\Phi = B\, d_{\text{eff}}\, l$ is the total magnetic flux threading the JJ, where d_{eff} is the effective thickness of the barrier. This expression leads to the typical Fraunhofer pattern in the I_c versus flux modulation.

By placing this JJ in an inline geometry, an additional contribution by the "self-field effect" is acquired. This implies that the inhomogeneous current distribution near the junction generates an additional magnetic field that influences the phase. The devices operate in the thin-film limit,

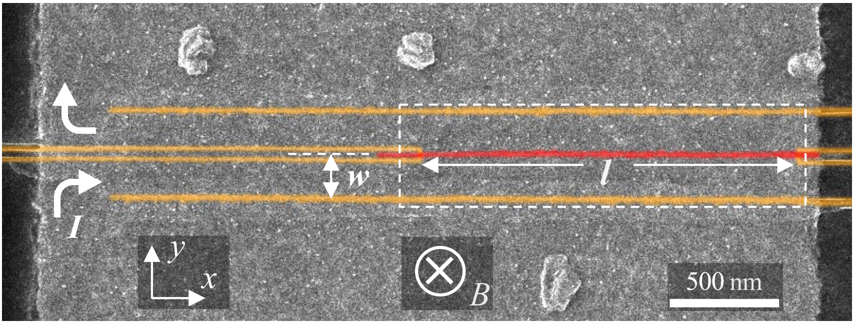

Figure 2.6: Secondary-electron HIM image of a reference microbridge with the same geometry as the reported device. For better visibility, the reference microbridge was irradiated with a higher dose to make the irradiation tracks visible. The tracks are colored to indicate the amorphous walls (golden) and the Josephson barrier (red). The thick arrows show the direction of bias current flow. The width of the YBCO bridge (grey) is W, JJ length is l, and the distance between the JJ barrier and the upper and lower amorphous walls is w. The dashed white rectangle shows the essential scale of the diode. © 2025 American Physical Society.

where the film thickness d is much smaller than the London penetration depth λ_L ($d \ll \lambda_\mathrm{L}$). Therefore, the self-field is rather referred to a self-induced phase gradient caused by the bias current, leading to $f = f_\Phi + f_\mathrm{I}\, i$, where $i = \frac{I}{I_\mathrm{c}}$ is the normalized critical current. f_I defines the in-line geometry parameter

$$f_I = \frac{\Phi_{I_\mathrm{c}}}{\Phi_0} = \frac{L\, I_\mathrm{c}}{\Phi_0} \overset{L=L_\mathrm{K}}{=} \frac{1}{4\pi}\left(\frac{l}{\lambda_\mathrm{J}}\right)^2, \tag{2.5}$$

where L is the inductance carrying the current I_c. The inductance is assumed to be purely kinetic, arising from the confinement of the superconducting electrodes along the barrier ($w < \lambda_\mathrm{L}$). The kinetic inductance follows the definition $L_\mathrm{k} = \mu_0 \lambda_\mathrm{L}^2 \frac{l}{w\,d}$, with l the length of the barrier and w the width of the superconducting electrodes. Considering the bias current entering through the bottom confinement, the current induces a large phase difference on the left side of the barrier, see Fig. 2.6. Farther to the right, where the current has already decreased significantly, the contribution from current flowing through the inductance becomes negligible.

The superposition of the self-induced phase gradient from the bias current and the field-induced phase gradient by the applied magnetic field results in a skewed dependence in the $I_c(B)$ behavior, see Fig. 2.7(b). Equation (2.5) identifies the tuning parameters for the device, namely l and λ_J. To sustain a single-valued CPR the condition $f_I < 1$ must be satisfied. This criterion yields an optimum value $f_I = \frac{\pi}{4}$ to maximize the asymmetry value $\mathcal{A}$, which defines the target specifications for the device $l \approx \pi\,\lambda_J$.

For the realization of the superconducting diode, a 30 nm-thick YBCO film grown on a LSAT substrate and capped with 20 nm of Au was used. In a 4 µm-wide microbridge an inline JJ design was embedded, depicted in Fig. 2.6. Both a high dose to nanopattern amorphous insulating barriers (AIBs) of the device and a moderate dose to form the Josephson junction was applied by means of He-FIB irradiation. To maximize L_k, the trench width w was minimized to 200 nm, which approaches the practical limit for the distance between insulating walls. Due to amorphization of the YBCO crystal caused by the huge irradiation dose[84], further reducing w would shrink the yield of working devices. The barrier Josephson junction, induced by an irradiation dose of 530 ions/nm with a length $l = 1750$ nm exhibited a symmetric critical current, $I_{c+} \approx |I_{c-}| \approx 10$ µA at zero magnetic field, cf. Fig. 2.7(a). Applying an external out-of-plane magnetic field to the junction unveils the asymmetric nature of the device, shown in Fig. 2.7(b). The highest obtained asymmetry is $\mathcal{A} \approx 7$ was achieved at the optimal magnetic field. This defines the operating point of the ScD.

To demonstrate the rectification in a quasistatic deterministic regime, the ScD is driven with a sinusoidal current $I(t) = I_{ac}\,\sin(2\pi f_D t)$ with the $f_D =$ 200 Hz. The voltage signal is averaged over one period of the driving current and presented in Fig. 2.8(a). As long as $I_{ac} < I_{c,+}, I_{c,-}$, no rectification takes place, since the device remains entirely in the superconducting state. When I_{ac} exceeds the lower absolute critical current ($I_{c,+} < I_{ac} < I_{c,-}$), rectification increases with the applied ac bias. In the idle case, the rectified voltage reaches a maximum value of 212 µV. For I_{ac} exceeding the critical

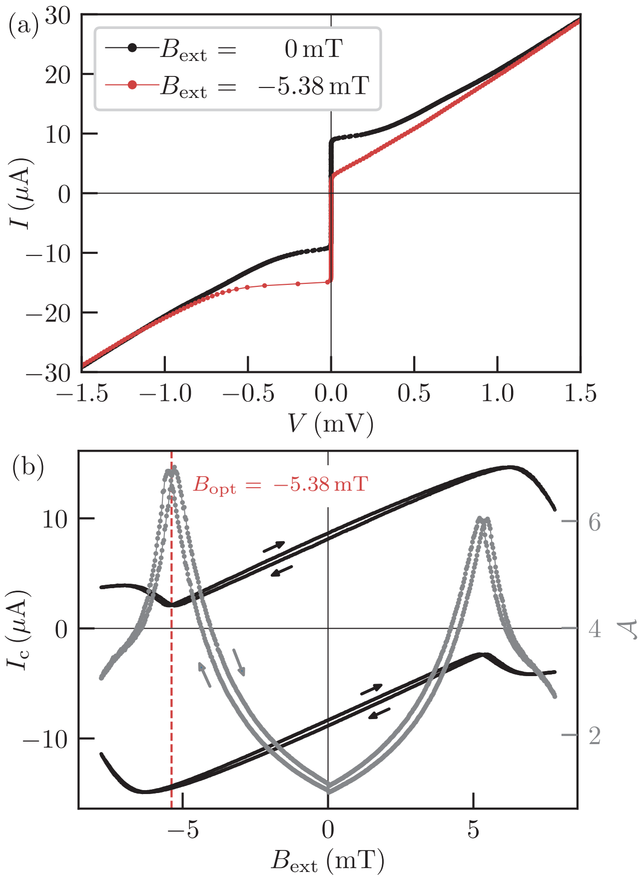

Figure 2.7: (a) IVCs at $B = 0$ (black) and at optimal applied magnetic field B_{opt} (red). $I_{c+}(0) \approx |I_{c-}(0)| \approx 10\,\mu A$, while $I_{c+}(B_{opt}) \approx 2.0\,\mu A$ and $|I_{c-}(B_{opt})| \approx 14.2\,\mu A$ (taken from IVCs with a voltage criterion of $1\,\mu V$), which results in $\mathcal{A}(B_{opt}) \approx 7$. (b) $I_{c\pm}(B)$ measured in both magnetic-field sweep directions (black) and $\mathcal{A}(B)$ (grey), numerically calculated from the $I_{c\pm}(B)$ data. The optimum magnetic field $B_{opt} \approx -5.38\,mT$. © 2025 American Physical Society.

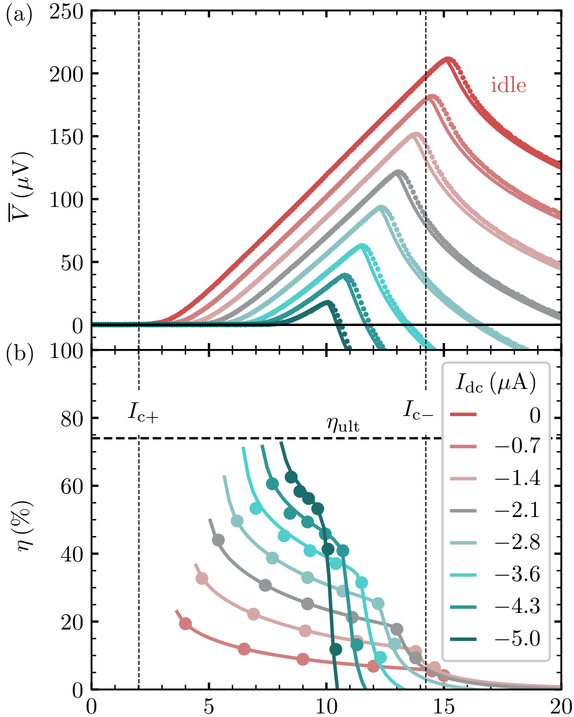

Figure 2.8: Performance of the ScD versus ac drive amplitude I_{ac} ($f_D = 200\text{Hz}$) at $B = B_{opt}$, for different values of counter current $I_{dc} \leq 0$. Panels show: (a) rectification curves $\bar{V}(I_{ac})$, (b) efficiency $\eta(I_{ac})$. Symbols represent experimental data; lines are calculated from the high-resolution experimental IVC. © 2025 American Physical Society.

currents of the device, the rectification decreases as the opposite voltage compensates in the average voltage signal. To test the load capacity of the ScD, this measurement was repeated with an additional counter current I_{dc}. This enabled the investigation of parameters like the output power, the input power and the efficiency of the device. At the maximum counter current, the efficiency approached to the ultimately achievable efficiency $\eta_{\mathrm{ult}} = \frac{\mathcal{A}+1}{\mathcal{A}-1} \approx 75\%$[26,85], see Fig.2.8(b). All measurement data were compared with simulated curves, extracted solely from IVC data at the optimal magnetic field. The simulated and measured curves show an excellent agreement, which enables the prediction of the optimal working point for the device by simulation rather than time-consuming electrical characterization.

Finally, rectification for a random driving force (noise) is numerically calculated based on the experimental IVC. The driving force follows a Gaussian distribution $G(I,\sigma) = \frac{1}{\sqrt{2\pi\sigma}} \exp(-\frac{I^2}{2\sigma^2})$, where σ represents the amplitude. The integrated region was limited to the range of $\pm 3\sigma$, revealing the beginning of the rectification at about $\sigma \approx 3\,\mu\mathrm{A}$. The maximum rectified voltage achieved by noise-driving the diode without any load was $115\,\mu\mathrm{V}$. Interestingly, the approached efficiency for the device was also the ultimate efficiency limit. These results predict that the diode can function as a noise rectifier at temperatures of several tens of kelvin.

Contributions

This work was carried out in cooperation with A. Jozani, R. Kleiner, D. Koelle and E. Goldobin. A. Jozani performed the measurements and contributed to data analysis and simulations. My contribution include device fabrication, data analysis, simulations, supervision, and manuscript preparation.

2.4 Publication 4: $YBa_2Cu_3O_{7-x}$ nano-constriction Josephson junctions and SQUIDs fabricated by focused helium-ion-beam irradiation

This publication tackles the downscaling limits of Josephson junctions realized in YBCO thin films. Successful implementation of constriction-type Josephson junctions in conventional superconductors like Al and Nb has been accomplished since decades. The aim was to establish a fabrication technique which enables such cJJs also in a high-T_c superconductor. To realize a constriction-type JJ, the constriction has to be on the order of the coherence length, which is only a few nanometers for YBCO. The only established method for manipulating materials at this scale is the He-FIB[64], whereas EBL nanostructuring limit stuck at ≈ 50 nm over a decade[60]. Irradiation of the YBCO crystal with the He-FIB leads to a local suppression of superconductivity. Applying a line scan across a prestructured microbridge in the YBCO thin film enables both structuring of Josephson barriers[64,65] and AIBs, depending on the irradiation dose. The latter suppresses any current flow providing a convenient approach for nanopatterning YBCO thin films. However, AIBs come with a drawback. For high irradiation doses, the crystal starts to amorphize, which induces mechanical stress even in the vicinity of the irradiated region[65,84]. The affected region reduces the resolution of the He-FIB from a few nanometers to roughly 50 nm to 100 nm. Thus, this commonly used He-FIB strategy for nanopatterning is not suitable for the creation of a constriction-type junction.

To cope with this problem, the novel approach of applying He^+ irradiation to an area rather than a single line was explored. The goal was to remain below the amorphization threshold to sustain the YBCO crystallinity, while suppressing any current transport in the irradiated region by increasing the barrier thickness. Using this approach, a dose series on $l = 30$ nm long rectangles within $W = 2$ µm wide microbridges was conducted, as presented in Fig. 2.9(a).

With increasing dose D_a, the T_c decreases. By approaching $D_a \approx 34\,\mathrm{ions/nm}^2$, resistance R shows roughly constant behavior over the temperature range $8\,\mathrm{K} < T < 89\,\mathrm{K}$. This provides an promising fabrication

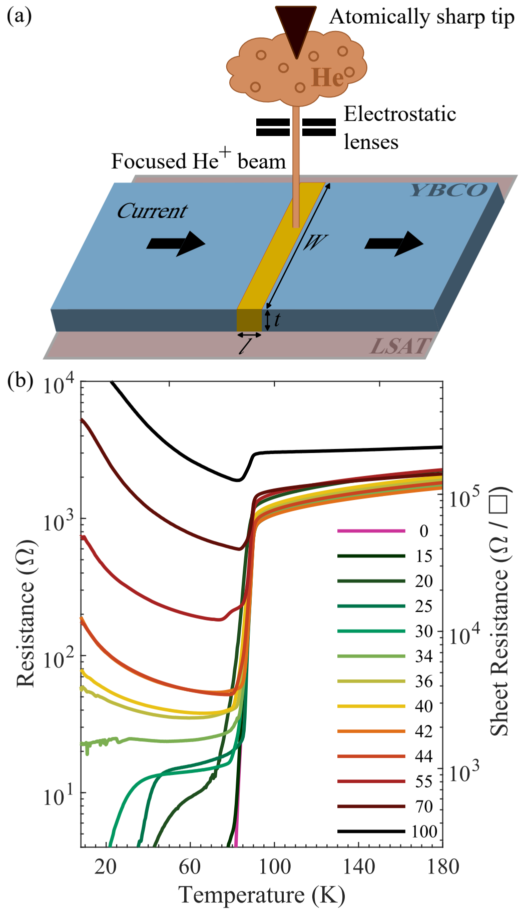

Figure 2.9: (a) Sketch of YBCO microbridge showing the He-FIB-irradiated area of length l and width W. The film thickness is $t = 30\,\mathrm{nm}$. (b) Resistance R versus temperature curves of microbridges containing irradiated regions ($l = 30\,\mathrm{nm}$, $W = 2\,\mu\mathrm{m}$) exposed with different areal doses D_a (color indicates dose in ions/nm^2). R was measured at a constant bias current $I = 1\,\mu\mathrm{A}$. The right vertical axis shows RW/l, which corresponds to the sheet resistance of the irradiated region below $T_{\mathrm{c},0}$, where $\square$ denotes a geometrical square area of thin film.

recipe for modeling a ultra-small constriction junction in the YBCO thin films. Apart from that, these new-found YBCO resistors can serve as circuit components, allowing straightforward integration into He-FIB–fabricated devices.

The knowledge gained from the YBCO resistors was subsequently applied to realize the patterning concept for a cJJ, see Fig. 2.10(c) inset. To illustrate the precision of the He-FIB in transferring a pattern onto the YBCO surface, the effectively applied dose was simulated. Therefore, the He-FIB spot size was assumed to have a Gaussian distribution with $\sigma = 3\,\mathrm{nm}$. All irradiated pixels of the patterning map were convoluted accordingly, cf. Fig. 2.10(a). A cross-sectional cut through the center of the cJJ, see Fig. 2.10(b), exemplifies the smearing of the patterning map edges as a consequence of the finite resolution of the He-FIB. A tunneling behavior at the edges of the cJJs is concluded, while for very small cJJs ($w < 20\,\mathrm{nm}$) the central region also exhibits a slight suppression of T_c. This suppression is caused by the edge damaging or degradation during nanopatterning, which is a familiar problem with cJJs fabrication[25,63].

Using this patterning concept, a series of cJJs was successfully fabricated exhibiting the smallest nominal junction width of $w = 6\,\mathrm{nm}$. At $T = 4.2\,\mathrm{K}$, the Josephson parameters turned out to be $I_\mathrm{c} = 10.8\,\mu\mathrm{A}$ and $R_\mathrm{n} = 240\,\Omega$, exhibiting an ideal RSJ-like current-voltage characteristic. These parameters correspond to a characteristic voltage of $V_\mathrm{c} = 2.6\,\mathrm{mV}$, which is remarkably high for a YBCO JJ with such a low I_c[66]. Thus, these junctions are highly suitable for THz applications, which was also successfully realized in the form of a THz detector. Several antennas with cJJs at their feedpoint were fabricated and excited by a far-infrared laser. This revealed Shapiro steps at several millivolts.

Furthermore, a nanoSQUID, entirely fabricated by He-FIB irradiation on a $2\,\mu\mathrm{m}$-wide microbridge is presented. With a central hole of only $100 \times 100\,\mathrm{nm}^2$, cJJs with $w = 12\,\mathrm{nm}$ are embedded on both sides of the hole symmetrically, see the inset of Fig. 2.11(a). The SQUID showed a modulation depth of 58% at a maximum critical current $I_\mathrm{c} = 6.5\,\mu\mathrm{A}$ at zero magnetic field. At optimal bias current, the SQUID exhibited a large voltage to flux transfer function V_Φ of $6\,\mathrm{mV}/\Phi_0$, see Fig. 2.11(b). This highlights the huge sensitivity of the produced nanoSQUID and

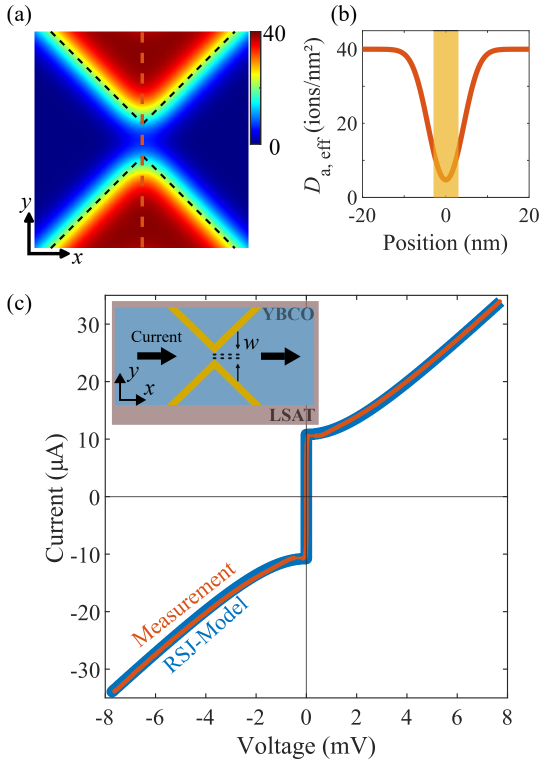

Figure 2.10: YBCO cJJ: (a) Color plot of effective dose $D_{\mathrm{a,eff}}(x, y)$ calculated for a constriction with $w = 6\,\mathrm{nm}$ and using a He-FIB spot size of $\sigma = 3\,\mathrm{nm}$ in a 40 x $40\,\mathrm{mm}^2$ region around the constriction. The dashed lines indicate the nominal edges of the irradiated areas (triangles) with a design distance of $w = 6\,\mathrm{nm}$ between the tips. The $D_{\mathrm{a,eff}}(0, y)$ profile, indicated by the orange dashed line, is shown in (b). The yellow area indicates the cJJ width w. (c) The orange IVC corresponds to a cJJ irradiated with $D_{\mathrm{a}} = 40\,\mathrm{ions/nm}^2$ and $w = 6\,\mathrm{nm}$, measured at $T = 4.2\,\mathrm{K}$. The blue IVC shows a RSJ-fit with a critical current $I_{\mathrm{c}} = 10.8\,\mu\mathrm{A}$ and a junction resistance $R_{\mathrm{n}} = 240\,\Omega$. The inset presents a sketch of the bridge geometry, where the yellow regions indicate the He-FIB-irradiated resistive areas (100 nm wide) defining the banks of a cJJ with the nominal constriction width w.

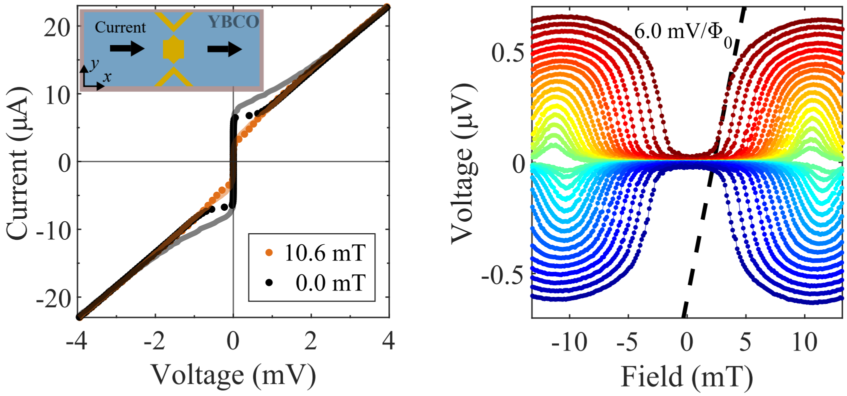

Figure 2.11: YBCO dc SQUID with cJJs: (a) Experimental (dots) and simulated (lines) IVCs of the nanoSQUID at zero magnetic field (black) and at $B = 10.6\,\mathrm{mT}$ (orange). The inset shows a schematic of a YBCO microbridge with the He-FIB irradiation pattern (yellow) realizing a SQUID. (b) Voltage versus applied magnetic field dependence at different bias currents through the nanoSQUID from $I = -6.8\,\mu\mathrm{A}$ (dark blue) to $I = 6.6\,\mu\mathrm{A}$ (dark red). The measurements were performed at $T \approx 4.2\,\mathrm{K}$.

prospects low flux noise S_Φ due to $S_\Phi = \frac{S_V}{|V_\Phi|}$. The measured IVCs and $I_c(B)$ dependence were compared with a theoretical model based on the Langevin equation for phase dynamics. This resulted in an effective screening parameter of $\beta_L^{\mathrm{eff}} \approx 0.9$. Comparison with 3D-MLSI[86] simulations indicates, that the main contribution to the inductance arises from the additional non-Josephson inductance in the constrictions. Therefore, the SQUID loop inductance can be neglected. The current-phase-relations of the cJJs appear slightly multi-valued, but almost identical for both cJJs.

Subsequently, the temperature dependence of the cJJ parameters were investigated. A set of junctions was characterized at different temperatures to determine about the operable temperature range and the dependence of the critical current I_c. All junctions are operable up to several tens of kelvin, which highlight the feasibility for applications with compact cooling requirements. The junctions with the highest $I_c(4\,\mathrm{K}) \sim 100\,\mu\mathrm{A}$ reach up to temperatures of $\sim 70\,\mathrm{K}$. However, at temperatures close to the junction T_c the thermal energy gets comparable to the Josephson energy, which limits applicability. The temperature dependence of the critical current follows closely the Bardeen equation reported in earlier studies[87].

2.4 **Publication 4:** *$YBa_2Cu_3O_{7-x}$ nano-constriction Josephson junctions and SQUIDs fabricated by focused helium-ion-beam irradiation*

Contributions

This work was carried out in cooperation with the group of M. Schilling at TU Braunschweig. Film growth and the measurements for temperature dependence and THz excitation were conducted there, primarily performed by M. Pröpper in assistance from D. Hanisch. R. Hutt and C. Magén provided a TEM analysis of He-FIB irradiated YBCO lamellas. C. Buckreus, D. Haas and M. Karrer supported parts of the data acquisition and evaluation and performed preliminary and subsequent measurements to support a deeper understanding of the topic. R. Kleiner performed the numerical simulations. I contributed to the paper by the device design, device fabrication, experimentation, data analysis and manuscript preparation.

3 Conclusion

This thesis establishes He-FIB nanopatterning of YBCO as a versatile platform for the fabrication of high-T_c Josephson devices. Building on the limitations of conventional Nb technology at high frequencies, high magnetic fields, and elevated temperatures, as well as challenges in nanofabrication, the thesis demonstrates that the combination of YBCO and He-FIB patterning can address several of these bottlenecks simultaneously. Irradiation by He-FIB of different dose enables continuous tuning of superconductivity without material removal. The He-FIB fabrication process is employed to tailor different device architectures and functionalities. The four publications composing this work cover single junctions, large-scale arrays, nonreciprocal Josephson devices, and nanometer-scale constriction junctions integrated into SQUIDs and THz antennas, addressing a broad range of applications relevant to metrology, sensing and superconducting circuit engineering.

Publication 1 emphasizes the high flexibility of He-FIB nanopatterning. Josephson parameters such as I_c and R_n can be easily tuned via the He-FIB irradiation dose. This provides the freedom to design these parameters according to experimental requirements. In addition, Josephson junctions can be positioned arbitrarily, opening a new perspective for device design. This has provided the foundation for a broad range of Josephson devices[65,71–75]. **Publication 1 and 2** successfully employ this technique to advance towards a high-T_c voltage standard. Building on these results and ongoing work[88,89], a solution for voltage standard is presented which comes with significant advantages. While state-of-the-art voltage standard need around 70,000 JJs to achieve 10V[38], a YBCO-based voltage standard require only 7000 JJs, assuming the same excitation frequency of 500 GHz, which lies at the lower end of the feasible frequency range. Additionally, thanks to nanofabrication technique, each JJ occupies less space, which pushes the miniaturization of the device even further. Complementary, the YBCO voltage standard operates at convenient cryogenic temperatures of several ten kelvins, which is realizable in portable cooling setups. As reported in **Publication 1**, a single JJ was successfully integrated in a lithographically structured THz antenna, measuring Shapiro steps at THz excitation. **Publication 2** then extends this approach from single JJs to multi-JJ arrays. A series array of 79 JJs enclosed by antenna structures were fabricated. A subset of JJs successfully established a operable THz detector. With that, a solid foundation for the high-T_c voltage standard was realized. Subsequently, **Publication 2** also pinpoints a crucial limitation of the fabrication technique, which is the junction-to-junction variation of the Josephson parameters. The publication firstly reports the significant spread in these parameters experimentally, illustrating the major challenge associated with YBCO JJs. Such variability in the fabrication of YBCO JJs is already well known for other junction types, such as grain-boundary[48,49] or ramp-type junctions[90,91] and unfortunately persists with He-FIB fabrication. The low yield in terms of fulfilling parameter specifications limits the technology to build the foundation of future Josephson circuit design. Only with extra post-processing of the devices, one can reduce this problem. Namely for single JJs is the variation of the JJ width and consequently the JJ parameters. In the case of multiple JJs with small spacing, such as in JJ arrays, one approach is the shunting of the devices, which mitigates the spread in the resistance. This remains an active research topic, representing one step forward towards the high-T_c voltage standard[88,89].

Publication 3 shifts the focus from reciprocal Josephson elements to engineered nonreciprocity by breaking time-reversal and inversion symmetry. This symmetry breaking is not achieved by adding complex multilayer heterostructures or materials with strong intrinsic spin–orbit coupling, but instead by an intentionally engineered device geometry within a single-layer YBCO thin film. By means of He-FIB irradiation, insulating barriers to confine the current path and a Josephson barrier compose a ScD with record values. This in-line geometry revealed an asymmetry value of approximately 7, outperforming almost all reported ScDs. Furthermore, the rectified voltages and efficiency values highlight the feasibility of this device to rectify noise. The possibility of operation in higher temperatures supports this outlook. Due to the small form factor, the device is easily upscalable, leading to proportionally higher rectified voltages. This opens a realistic perspective for integrating diode-like Josephson elements into future high-frequency and sensor circuits where nonreciprocity is valuable[92].

The results of **Publication 3** also highlight clear next steps. A primary challenge is to translate the diode effect from externally biased operation towards concepts with built-in phase biasing or reduced dependence on global magnetic fields, which would facilitate integration into compact circuit environments and scanning-probe platforms. This could be realized by placing a vortex close to the in-line JJ, as in Ref.[93] or by using an adjacent modulation line. Furthermore, systematic studies of microwave response and high-frequency rectification behavior will be essential to position high-T_c diodes within the broader landscape of nonreciprocal superconducting circuit elements.

Publication 4 addresses the miniaturization frontier by developing barrierless constriction Josephson junctions in YBCO reaching the ten-nanometer regime and remaining operational up to liquid-nitrogen temperatures. This is a decisive step, since the reproducibility in conventional cuprate nanofabrication typically degrades rapidly below $\sim 50\,\mathrm{nm}$ due to etch-induced damage, oxygen loss, and process-related edge degradation. The He-FIB cJJ approach presents a promising fabrication technique by creating normal-conducting regions through controlled irradiation doses. Thereby the continuity of the superconducting film is preserved, avoiding amorphization or extensive heating due to huge irradiation doses. By sculpting resistive areas around a narrow superconducting constriction, **Publication 4** enables a new class of high-T_c weak links whose relevant dimensions are determined by the He-FIB resolution rather than by lithographic and etching limits. The publication presents the smallest cJJ ever realized in a high-T_c superconductor, accompanied by outstanding Josephson parameters. Revealing a characteristic voltage of only $2.6\,\mathrm{mV}$ for the smallest junction, these cJJs are highly suitable for applications, such as SQUIDs and THz detectors. These examples were successfully realized with promising figures of merit. This novel fabrication technique pushes the miniaturization almost an order of magnitude beyond the common fabrication frontier with EBL and Ar-ion milling[56,60]. The results could advance the field of scanning SQUID microscopy, specifically SQUID-on-lever designs, as already realized in the EU-funded project FIBsuperprobes[25]. Higher operational temperatures and magnetic fields, alongside stronger miniaturization, should give this scanning microscopy approach a new dimension. The realization of a constriction junction in a d-wave superconductor also opens the opportunity to realize a π-JJ[94], which is currently under investigation. The necessity of a constriction in the order of the coherence length had represented a major bottleneck for a long time in this research field, which could now be addressed by the presented fabrication technique. This advancement would feed right into the field of superconducting digital logic and memory[95].

In summary, the presented publications demonstrate that He-FIB nanopatterning is much more versatile than merely fabricating Josephson barriers in YBCO. Using the toolbox of bJJs, cJJs, YBCO resistors, and insulating barriers, the work delivers antenna-integrated THz-responsive junctions, the first detailed reproducibility analysis of a He-FIB-written high-T_c array based on individual-junction measurements, a high-T_c Josephson diode with strong nonreciprocity engineered in a planar architecture, and ten-nanometer-scale constriction junctions that enable genuine high-T_c nano Josephson circuits. Initial experiments show, that an additional Au layer on top of the YBCO thin film or as shunt resistors could optimize the parameter spread, as also observed in other FIB techniques[44,96,97]. Promisingly, the disorder caused by He-FIB irradiation can be utilized not only in YBCO. Materials like NbN, NbTiN, MgB_2 and BSCCO have also demonstrated feasibility with this fabrication technique[98–102]. The results thus mark an important step towards a mature high-T_c Josephson technology that can complement and potentially surpass the established Nb-based platform.

Declaration on the use of generative AI

For the revision of grammar and spelling errors as well as the translation of individual text sections, the large language models ChatGPT 4.0 and ChatGPT 5.1 were used.

Bibliography

[1] B. D. Josephson, "Possible new effects in superconductive tunnelling", Phys. Lett. **1**, 251–253 (1962).

[2] A. Barone and G.釀Paternò, Physics and application of the Josephson effect (John Wiley and Sons, New York, 1982).

[3] A. Rüfenacht, N. E. Flowers-Jacobs, and S. P. Benz, "Impact of the latest generation of Josephson voltage standards in ac and dc electric metrology", Metrologia **55**, S152–S173 (2018).

[4] R. Behr, O. Kieler, J. Kohlmann, F. Müller, and L. Palafox, "Development and metrological applications of Josephson arrays at PTB", Meas. Sci. Technol. **23**, 124002 (2012).

[5] J. Clarke and A. I. Braginski, eds., The squid handbook, volume i: fundamentals and technology of squids and squid sy (Wiley-VCH, Weinheim, 2004).

[6] R. Kleiner, D. Koelle, F. Ludwig, and J. Clarke, "Superconducting quantum interference devices: State of the art and applications", Proc. IEEE **92**, 1534–1548 (2004).

[7] J. Koch, T. M. Yu, J. Gambetta, A. A. Houck, D. I. Schuster, J. Majer, A. Blais, M. H. Devoret, S. M. Girvin, and R. J. Schoelkopf, "Charge-insensitive qubit design derived from the Cooper pair box", Phys. Rev. A **76**, 042319 (2007).

[8] J. Aumentado, "Superconducting Parametric Amplifiers: The State of the Art in Josephson Parametric Amplifiers", IEEE Microw. Mag. **21**, 45–59 (2020).

[9] J. R. Tucker and M. J. Feldman, "Quantum detection at millimeter wavelengths", Rev. Mod. Phys. **57**, 1055–1113 (1985).

[10] M. H. Devoret, J. M. Martinis, D. Esteve, and J. Clarke, "Resonant Activation from the Zero-Voltage State of a Current-Biased Josephson Junction", Phys. Rev. Lett. **53**, 1260–1263 (1984).

[11]J. M. Martinis, M. H. Devoret, and J. Clarke, "Energy-Level Quantization in the Zero-Voltage State of a Current-Biased Josephson Junction", Phys. Rev. Lett. **55**, 1543–1546 (1985).

[12]J. Clarke, A. N. Cleland, M. H. Devoret, D. Esteve, and J. M. Martinis, "Quantum Mechanics of a Macroscopic Variable: The Phase Difference of a Josephson Junction", Science **239**, 992–997 (1988).

[13]M. H. Devoret and R. J. Schoelkopf, "Superconducting Circuits for Quantum Information: An Outlook", Science **339**, 1169–1174 (2013).

[14]P. Krantz, M. Kjaergaard, F. Yan, T. P. Orlando, S. Gustavsson, and W. D. Oliver, "A quantum engineer's guide to superconducting qubits", Appl. Phys. Rev. **6**, 021318 (2019).

[15]M. J. Martínez-Pérez and D. Koelle, "NanoSQUDs: Basics & recent advances", Phys. Sci. Rev. **2**, 20175001 (2017).

[16]M. Nadeem, M. S. Fuhrer, and X. Wang, Superconducting Diode Effect – Fundamental Concepts, Material Aspects, and I Jan. 2023.

[17]A. I. Braginski, "Superconductor Electronics: Status and Outlook", J. Supercond. Nov. Magn. **32**, 23–44 (2019).

[18]C. Granata and A. Vettoliere, "Nano Superconducting Quantum Interference device: A powerful tool for nanoscale investigations", Phys. Rep. **614**, 1–69 (2016).

[19]J. Clarke, "Josephson Junction Detectors", Science **184**, 1235–1242 (1974).

[20]C. D. Tesche and J. Clarke, "Dc SQUID: Noise and optimization", J. Low Temp. Phys. **29**, 301–331 (1977).

[21]R. L. Fagaly, "Superconducting quantum interference device instruments and applications", Rev. Sci. Instrum. **77**, 101101 (2006).

[22]D. Vasyukov, Y. Anahory, L. Embon, D. Halbertal, J. Cuppens, L. Neeman, A. Finkler, Y. Segev, Y. Myasoedov, M. L. Rappaport, M. E. Huber, and E. Zeldov, "A scanning superconducting quantum interference device with single electron spin sensitivity", Nat. Nanotechnol. **8**, 639–644 (2013).

[23]Y. Anahory, H. R. Naren, E. O. Lachman, S. B. Sinai, A. Uri, L. Embon, E. Yaakobi, Y. Myasoedov, M. E. Huber, R. Klajn, and E. Zeldov, "SQUID-on-tip with single-electron spin sensitivity for high-field and ultra-low temperature nanomagnetic imaging", Nanoscale **12**, 3174–3182 (2020).

[24]K. Bagani, A. Vervelaki, D. Jetter, A. Devarakonda, M. A. Tschudin, B. Gross, D. G. Chica, D. A. Broadway, C. R. Dean, X. Roy, P. Maletinsky, and M. Poggio, "Imaging Strain-Controlled Magnetic Reversal in Thin CrSBr", Nano Lett. **24**, 13068–13074 (2024).

[25]T. Weber, D. Jetter, J. Ullmann, S. A. Koch, S. F. Pfander, K. Kress, A. Vervelaki, B. Gross, O. Kieler, U. Drechsler, P. R. Baral, A. Magrez, R. Kleiner, A. W. Knoll, M. Poggio, and D. Koelle, "Advanced SQUID-on-lever scanning probe for high-sensitivity magnetic microscopy with sub-100-nm spatial resolution", Phys. Rev. Appl. **24**, 054041 (2025).

[26]E. Goldobin, R. Menditto, D. Koelle, and R. Kleiner, "Model I–V curves and figures of merit of underdamped deterministic Josephson ratchets", Phys. Rev. E **94**, 032203 (2016).

[27]Y. Zhang, Y. Gu, P. Li, J. Hu, and K. Jiang, "General Theory of Josephson Diodes", Phys. Rev. X **12**, 041013 (2022).

[28]C. Baumgartner, L. Fuchs, A. Costa, S. Reinhardt, S. Gronin, G. C. Gardner, T. Lindemann, M. J. Manfra, P. E. Faria Junior, D. Kochan, J. Fabian, N. Paradiso, and C. Strunk, "Supercurrent rectification and magnetochiral effects in symmetric Josephson junctions", Nat. Nanotechnol. **17**, 39–44 (2022).

[29]H. Wu, Y. Wang, Y. Xu, P. K. Sivakumar, C. Pasco, U. Filippozzi, S. S. P. Parkin, Y.-J. Zeng, T. McQueen, and M. N. Ali, "The field-free Josephson diode in a van der Waals heterostructure", Nature **604**, 653–656 (2022).

[30]M. Beck, E. Goldobin, M. Neuhaus, M. Siegel, R. Kleiner, and D. Koelle, "High-Efficiency Deterministic Josephson Vortex Ratchet", Phys. Rev. Lett. **95**, 090603 (2005).

[31]A. Sterck, S. Weiss, and D. Koelle, "SQUID ratchets: basics and experiments", Appl. Phys. A **75**, 253–262 (2002).

[32]A. Sterck, D. Koelle, and R. Kleiner, "Rectification in a Stochastically Driven Three-Junction SQUID Rocking Ratchet", Phys. Rev. Lett. **103**, 047001 (2009).

[33]F. Paolucci, G. De Simoni, and F. Giazotto, "A gate- and flux-controlled supercurrent diode effect", Appl. Phys. Lett. **122**, 042601 (2023).

[34]M. Davydova, S. Prembabu, and L. Fu, "Universal Josephson diode effect", Sci. Adv. **8**, eabo0309 (2022).

[35]S. Weiss, D. Koelle, J. Müller, R. Gross, and K. Barthel, "Ratchet effect in dc SQUIDs", Europhys. Lett. **51**, 499 (2000).

[36]J. R. Tucker, "Quantum limited detection in tunnel junction mixers", IEEE J. Quantum Electron. **15**, 1234–1258 (1979).

[37]O. Harnack, S. Beuven, M. Darula, H. Kohlstedt, M. Tarasov, E. Stephansov, and Z. Ivanov, "HTS mixers based on the Josephson effect and on the hot-electron bolometric effect", IEEE Trans. Appl. Supercond. **9**, 3765–3768 (1999).

[38]F. Mueller, R. Behr, T. Weimann, L. Palafox, D. Olaya, P. D. Dresselhaus, and S. P. Benz, "1 V and 10 V SNS Programmable Voltage Standards for 70 GHz", IEEE Trans. Appl. Supercond. **19**, 981–986 (2009).

[39]H. Ter Brake and G. Wiegerinck, "Low-power cryocooler survey", Cryogenics **42**, 705–718 (2002).

[40]S. K. Tolpygo, "Superconductor digital electronics: Scalability and energy efficiency issues (Review Article)", Low Temp. Phys. **42**, 361–379 (2016).

[41]K. Likharev and V. Semenov, "RSFQ logic/memory family: a new Josephson-junction technology for sub-terahertz-clock-frequency digital systems", IEEE Trans. Appl. Supercond. **1**, 3–28 (1991).

[42]Cryogenic Electronics and Quantum Information Processing (CEQIP) International Focus Team,
International Roadmap for Devices and Systems (IRDS): 2023 Update — Cryogenic
tech. rep., Accessed: 2026-01-23 (IEEE, 2023).

[43]S. K. Tolpygo, V. Bolkhovsky, T. J. Weir, L. M. Johnson, M. A. Gouker, and W. D. Oliver, "Fabrication Process and Properties of Fully-Planarized Deep-Submicron Nb/Al-AlO_x/Nb Josephson Junctions for VLSI Circuits", IEEE Trans. Appl. Supercond. **25**, 1101312 (2015).

[44]T. Schwarz, J. Nagel, R. Wölbing, M. Kemmler, R. Kleiner, and D. Koelle, "Low-Noise Nano Superconducting Quantum Interference Device Operating in Tesla Magnetic Fields", ACS Nano **7**, 844–850 (2013).

[45]M. K. Wu, J. R. Ashburn, C. J. Torng, P. H. Hor, R. L. Meng, L. Gao, Z. J. Huang, Y. Q. Wang, and C. W. Chu, "Superconductivity at 93 K in a new mixed-phase Y-Ba-Cu-O compound system at ambient pressure", Phys. Rev. Lett. **58**, 908–910 (1987).

[46]A. Stangl, A. Palau, G. Deutscher, X. Obradors, and T. Puig, "Ultra-high critical current densities of superconducting YBa2Cu3O7-δ thin films in the overdoped state", Sci. Rep. **11**, 8176 (2021).

[47]B. Oh, K. Char, A. D. Kent, M. Naito, M. R. Beasley, T. H. Geballe, R. H. Hammond, A. Kapitulnik, and J. M. Graybeal, "Upper critical field, fluctuation conductivity, and dimensionality of $YBa_2Cu_3O_{7-x}$", Phys. Rev. B **37**, 7861–7864 (1988).

[48]R. Gross, L. Alff, A. Beck, O. Froehlich, D. Koelle, and A. Marx, "Physics and technology of high temperature superconducting josephson junctions", IEEE Trans. Appl. Supercond. **7**, 2929–2935 (1997).

[49]H. Hilgenkamp and J. Mannhart, "Grain boundaries in high-T_c superconductors", Rev. Mod. Phys. **74**, 485–549 (2002).

[50]F. Tafuri and J. R. Kirtley, "Weak links in high critical temperature superconductors", Reports on Progress in Physics **68**, 2573 (2005).

[51] F. Tafuri, D. Massarotti, L. Galletti, D. Stornaiuolo, D. Montemurro, L. Longobardi, P. Lucignano, G. Rotoli, G. P. Pepe, A. Tagliacozzo, and F. Lombardi, “Recent Achievements on the Physics of High-T_C Superconductor Josephson Junctions: Background, Perspectives and Inspiration”, J. Supercond. Nov. Magn. **26**, 21–41 (2013).

[52] J. Schneider, H. Kohlstedt, and R. Wördenweber, “Nanobridges of optimized $YBa_2Cu_3O_7$ thin films for superconducting flux-flow type devices”, Appl. Phys. Lett. **63**, 2426–2428 (1993).

[53] G. Papari, F. Carillo, D. Stornaiuolo, L. Longobardi, F. Beltram, and F. Tafuri, “High critical current density and scaling of phase-slip processes in YBaCuO nanowires”, Supercond. Sci. Technol. **25**, 035011 (2012).

[54] P. Larsson, B. Nilsson, and Z. G. Ivanov, “Fabrication and transport measurements of $YBa_2Cu_3O_{7-x}$ nanostructures”, J. Vac. Sci. Technol. B **18**, 25–31 (2000).

[55] S. Nawaz, R. Arpaia, T. Bauch, and F. Lombardi, “Approaching the theoretical depairing current in $YBa_2Cu_3O_{7-x}$ nanowires”, Physica C **495**, 33–38 (2013).

[56] R. Arpaia, S. Nawaz, F. Lombardi, and T. Bauch, “Improved nanopatterning for YBCO nanowires approaching the depairing current”, IEEE Trans. Appl. Supercond. **23**, 1101505–1101505 (2013).

[57] R. Arpaia, M. Arzeo, R. Baghdadi, E. Trabaldo, F. Lombardi, and T. Bauch, “Improved noise performance of ultrathin YBCO Dayem bridge nanoSQUIDs”, Supercond. Sci. Technol. **30**, 014008 (2016).

[58] R. Arpaia, D. Golubev, R. Baghdadi, R. Ciancio, G. Dražić, P. Orgiani, D. Montemurro, T. Bauch, and F. Lombardi, “Transport properties of ultrathin $YBa_2Cu_3O_{7-\delta}$ nanowires: A route to single-photon detection”, Phys. Rev. B **96**, 064525 (2017).

[59] S. Nawaz, R. Arpaia, F. Lombardi, and T. Bauch, “Microwave response of superconducting $YBa_2Cu_3O_{7-\delta}$ nanowire bridges sustaining the critical depairing current: Evidence of Josephson-like Behavior”, Phys. Rev. Lett. **110**, 167004 (2013).

[60]E. Trabaldo, R. Arpaia, M. Arzeo, E. Andersson, D. Golubev, F. Lombardi, and T. Bauch, "Transport and noise properties of YBCO nanowire based nanoSQUIDs", Supercond. Sci. Technol. **32**, 073001 (2019).

[61]E. Trabaldo, S. Ruffieux, E. Andersson, R. Arpaia, D. Montemurro, J. F. Schneiderman, A. Kalaboukhov, D. Winkler, F. Lombardi, and T. Bauch, "Properties of grooved Dayem bridge based $YBa_2Cu_3O_{7-\delta}$ superconducting quantum interference devices and magnetometers", Appl. Phys. Lett. **116**, 132601 (2020).

[62]H. Ma, H. Wang, Y. Wang, Z. Luo, Z. Li, Y. Wang, X. Du, C. Yang, J. Huang, C. Wu, N. Li, X. Wang, Y. Liu, and P. Li, "Minimal Damage and Tunable Fabrication of Atomic-Scale Ultrathin $YBa_2Cu_3O_{7-\delta}$ Nanowires with High Uniformity", Small Struct. **6**, 2400661 (2025).

[63]K. Uhl, D. Hackenbeck, J. Peter, R. Kleiner, D. Koelle, and D. Bothner, "Niobium quantum interference microwave circuits with monolithic three-dimensional nanobridge junctions", Phys. Rev. Appl. **21**, 024051 (2024).

[64]S. A. Cybart, E. Y. Cho, T. J. Wong, B. H. Wehlin, M. K. Ma, C. Huynh, and R. C. Dynes, "Nano Josephson superconducting tunnel junctions in $YBa_2Cu_3O_{7-\delta}$ directly patterned with a focused helium ion beam", Nat. Nanotechnol. **10**, 598–602 (2015).

[65]B. Müller, M. Karrer, F. Limberger, M. Becker, B. Schröppel, C. J. Burkhardt, R. Kleiner, E. Goldobin, and D. Koelle, "Josephson junctions and SQUIDs created by focused helium-ion-beam irradiation of $YBa_2Cu_3O_7$", Phys. Rev. Appl. **11**, 044082 (2019).

[66]E. Y. Cho, Y. W. Zhou, J. Y. Cho, and S. A. Cybart, "Superconducting nano Josephson junctions patterned with a focused helium ion beam", Appl. Phys. Lett. **113**, 022604 (2018).

[67]I. A. Zaluzhnyy, U. Goteti, B. K. Stoychev, R. Basak, E. S. Lamb, E. Kisiel, T. Zhou, Z. Cai, M. V. Holt, J. W. Beeman, E. Y. Cho, S. Cybart, O. G. Shpyrko, R. Dynes, and A. Frano, "Structural changes in $YBa_2Cu_3O_7$ thin films modified with He^+-focused ion beam

for high-temperature superconductive nanoelectronics", ACS Appl. Nano Mater. **7**, 15943–15949 (2024).

[68] W. Lang, M. Dineva, M. Marksteiner, T. Enzenhofer, K. Siraj, M. Peruzzi, J. D. Pedarnig, D. Bäuerle, R. Korntner, E. Cekan, E. Platzgummer, and H. Loeschner, "Ion-beam direct-structuring of high-temperature superconductors", Microelectron. Eng. **83**, 1495–1498 (2006).

[69] W. Lang, M. Marksteiner, M. Bodea, K. Siraj, J. Pedarnig, R. Kolarova, P. Bauer, K. Haselgrübler, C. Hasenfuss, I. Beinik, and C. Teichert, "Ion beam irradiation of cuprate high-temperature superconductors: systematic modification of the electrical properties and fabrication of nanopatterns", Nuclear Instruments and Methods in Physics Research Section B: Beam Interactions with Materials and Atoms **272**, 300–304 (2012).

[70] N. Sarkar and S. A. Cybart, "Design Rules for Resistors, Capacitors and Inductors Fabricated From Single Layer Y-Ba-Cu-O Thin Films With Focused Helium Ion Beam Irradiation", IEEE Trans. Appl. Supercond. **33**, 1101305 (2023).

[71] E. Y. Cho, H. Li, J. C. LeFebvre, Y. W. Zhou, R. C. Dynes, and S. A. Cybart, "Direct-coupled micro-magnetometer with Y-Ba-Cu-O nano-slit SQUID fabricated with a focused helium ion beam", Appl. Phys. Lett. **113**, 162602 (2018).

[72] E. Y. Cho, Y. W. Zhou, M. M. Khapaev, and S. A. Cybart, "Investigation of Arrays of Two-Dimensional High-T_C SQUIDs for Optimization of Electrical Properties", IEEE Trans. Appl. Supercond. **29**, 1601304 (2019).

[73] H. Li, H. Cai, E. Y. Cho, S. J. McCoy, Y.-T. Wang, J. C. LeFebvre, Y. W. Zhou, and S. A. Cybart, "High-transition-temperature nanoscale superconducting quantum interference devices directly written with a focused helium ion beam", Appl. Phys. Lett. **116**, 070601 (2020).

[74] J. C. LeFebvre, E. Cho, H. Li, H. Cai, and S. A. Cybart, "Flux focused series arrays of long Josephson junctions for high-dynamic range magnetic field sensing", J. Appl. Phys. **131**, 163902 (2022).

[75]K. Uhl, D. Hackenbeck, C. Füger, R. Kleiner, D. Koelle, and D. Bothner, “A flux-tunable $YBa_2Cu_3O_7$ quantum interference microwave circuit”, Appl. Phys. Lett. **122**, 182603 (2023).

[76]M. Karrer, K. Wurster, J. Linek, M. Meichsner, R. Kleiner, E. Goldobin, and D. Koelle, “Temporal evolution of electric transport properties of $YBa_2Cu_3O_{7-\delta}$ Josephson junctions produced by focused-helium-ion-beam irradiation”, Phys. Rev. Appl. **21**, 014065 (2024).

[77]A. M. Klushin, M. He, M. Y. Levitchev, V. V. Kurin, and N. Klein, “Optimization of the coupling of mm wave power to arrays of high-T_c Josephson junctions”, J. Phys.: Conf. Ser. **97**, 012268 (2008).

[78]R. Hackl, W. Gläser, P. Müller, D. Einzel, and K. Andres, “Light-Scattering Study of the Superconducting Energy Gap in $YBa_2Cu_3O_7$ Single Crystals”, Phys. Rev. B **38**, 7133–7136 (1988).

[79]A. Cortez, E. Y. Cho, H. Li, D. Cunnane, B. Karasik, and S. A. Cybart, “High-Frequency Properties of Y-Ba-Cu-O Josephson Junctions Fabricated with Helium Ion Beam Irradiation”, in 2019 IEEE International Superconductive Electronics Conference (ISEC) (July 2019), pp. 1–3.

[80]Y. Divin, O. Volkov, V. Pavlovskii, U. Poppe, and K. Urban, “Terahertz spectral analysis by ac Josephson Effect in high-$\mathrm{T_c}$ bicrystal junctions”, IEEE Trans. Appl. Supercond. **11**, 582–585 (2001).

[81]J. C. LeFebvre, E. Cho, H. Li, K. Pratt, and S. A. Cybart, “Series arrays of planar long josephson junctions for high dynamic range magnetic flux detection”, AIP Advances **9**, 105215 (2019).

[82]J. C. LeFebvre and S. A. Cybart, “Large-Scale Focused Helium Ion Beam Lithography”, IEEE Trans. Appl. Supercond. **31**, 1100404 (2021).

[83]T. A. Fulton and L. N. Dunkleberger, “Lifetime of the zero-voltage state in Josephson tunnel junctions”, Phys. Rev. B **9**, 4760–4768 (1974).

[84] M. Karrer, B. Aichner, K. Wurster, C. Magén, C. Schmid, R. Hutt, B. Budinská, O. V. Dobrovolskiy, R. Kleiner, W. Lang, E. Goldobin, and D. Koelle, "Vortex matching at 6 T in $YBa_2Cu_3O_{7-\delta}$ thin films by imprinting a 20-nm periodic pinning array with a focused helium-ion beam", Phys. Rev. Appl. **22**, 014043 (2024).

[85] M. Knufinke, K. Ilin, M. Siegel, D. Koelle, R. Kleiner, and E. Goldobin, "Deterministic Josephson vortex ratchet with a load", Phys. Rev. E **85**, 011122 (2012).

[86] M. Khapaev, A. Kidiyarova-Shevchenko, P. Magnelind, and M. Kupriyanov, "3D-MLSI: software package for inductance calculation in multilayer superconducting integrated circuits", IEEE Trans. Appl. Supercond. **11**, 1090–1093 (2001).

[87] J. Bardeen, "Critical Fields and Currents in Superconductors", Rev. Mod. Phys. **34**, 667–681 (1962).

[88] M. Pröpper, M.-A. Tucholke, D. Hanisch, C. Schmid, P. J. Ritter, M. Neumann, E. Goldobin, D. Koelle, R. Kleiner, M. Schilling, and B. Hampel, "Shunting $YBa_2Cu_3O_{7-x}$ Josephson Junctions and Arrays Fabricated by He-FIB", IEEE Trans. Appl. Supercond. **36**, 1100206 (2026).

[89] M. Pröpper, M.-A. Tucholke, C. Schmid, O. Kieler, M. Neumann, P. J. Ritter, E. Goldobin, D. Koelle, R. Kleiner, M. Schilling, and B. Hampel, "Toward a Voltage Standard Using $YBa_2Cu_3O_{7-x}$ Josephson Junction Arrays Fabricated by He-FIB", IEEE Trans. Appl. Supercond., 1400106 (2026).

[90] J. Yoshida, H. Katsuno, S. Inoue, and T. Nagano, "Current transport in interface-engineered high-$\underline{T}$c Josephson junctions", Physica C: Superconductivity **367**, 260–266 (2002).

[91] S. K. H. Lam, J. Lazar, J. Du, and C. P. Foley, "Critical current variation in $YBa_2Cu_3O_{7-x}$ step-edge junction arrays on MgO substrates", Supercond. Sci. Technol. **27**, 055011 (2014).

[92] R. A. Hovhannisyan, A. Lotfian, T. Golod, and V. M. Krasnov, "Demonstration of an optical microwave rectification by a superconducting diode with near 100% efficiency", arXiv:2508.21696 (2025).

[93] T. Golod and V. M. Krasnov, "Demonstration of a superconducting diode-with-memory, operational at zero magnetic field with switchable nonreciprocity", Nat. Commun. **13**, 3658 (2022).

[94] A. Gumann and N. Schopohl, "Phase diagram of geometric d -wave superconductor Josephson junctions", Phys. Rev. B **79**, 144505 (2009).

[95] D. S. Holmes, A. M. Kadin, and M. W. Johnson, "Superconducting Computing in Large-Scale Hybrid Systems", Computer **48**, 34–42 (2015).

[96] J. Nagel, K. B. Konovalenko, M. Kemmler, M. Turad, R. Werner, E. Kleisz, S. Menzel, R. Klingeler, B. Büchner, R. Kleiner, and D. Koelle, "Resistively shunted $YBa_2Cu_3O_7$ grain boundary junctions and low-noise SQUIDs patterned by a focused ion beam down to 80 nm linewidth", Supercond. Sci. Technol. **24**, 015015 (2011).

[97] Y. Shibata, S. Nomura, H. Kashiwaya, S. Kashiwaya, R. Ishiguro, and H. Takayanagi, "Imaging of current density distributions with a Nb weak-link scanning nano-SQUID microscope", Sci. Rep. **5**, 15097 (2015).

[98] L. Kasaei, T. Melbourne, V. Manichev, L. C. Feldman, T. Gustafsson, K. Chen, X. X. Xi, and B. A. Davidson, "MgB_2 Josephson junctions produced by focused helium ion beam irradiation", AIP Adv. **8**, 075020 (2018).

[99] Y.-T. Wang, J. C. LeFebvre, E. Y. Cho, S. J. McCoy, H. Li, G. Gu, K. Kadowaki, and S. A. Cybart, "Fabrication of $Bi_2Sr_2CaCu_2O_{8+x}$ -Plane Josephson Junctions by a Focused Helium Ion Beam", IEEE Trans. Appl. Supercond. **31**, 1100104 (2021).

[100] H. Li, H. Cai, J. Forman, R. Cheng, G. Hughes, H. Walker, M. C. Hamilton, L. Chen, W. Zhang, L. You, and S. A. Cybart, "Transport Properties of NbN Thin Films Patterned With a Focused Helium Ion Beam", IEEE Trans. Appl. Supercond. **33**, 1100904 (2023).

[101] D. Yin, X. Cai, T. Xu, R. Sun, Z. Chen, Y. Han, L. Tian, Y. Wang, Y. Zhang, and Z. Gan, "MgB_2 Josephson Junctions fabricated by Focused Helium Ion Beam with different irradiation doses on SiC and MgO substrates", Physica C Supercond. **623**, 1354532 (2024).

[102] A. Ruhtinas and I. J. Maasilta, "Highly tunable NbTiN Josephson junctions fabricated with focused helium ion beam", Phys. Rev. Res. **7**, 043252 (2025).

Appended publications

Publication 1

Reproduced with permission from
M. Pröpper *et al.*, IEEE Trans. Appl. Supercond. **34**, 1100505 (2024)

THz Properties of He-FIB $YBa_2Cu_3O_{7-x}$ Josephson Junctions

M. Pröpper, D. Hanisch, C. Schmid, P. J. Ritter, M. Neumann, E. Goldobin, D. Koelle, R. Kleiner, M. Schilling, and B. Hampel

***Abstract*—Josephson junctions with customizable parameters, including critical current I_c and normal state resistance R_n, hold great promise across a wide range of applications. Notably, high-temperature superconductors like $YBa_2Cu_3O_{7-x}$ have been interesting since their discovery due to their simplified cooling requirements. $YBa_2Cu_3O_{7-x}$ Josephson junctions can operate within the terahertz (THz) frequency range, rendering them highly suitable for various applications. To maximize their suitability at these high frequencies, it is imperative to precisely determine their THz parameters. Helium focused ion beam (He-FIB) technology is a very promising fabrication method for customizable Josephson junctions. It allows precise control of the He-FIB dose during the fabrication of Josephson junctions and facilitates the fine-tuning of I_c and R_n. This study presents the fabrication process of $YBa_2Cu_3O_{7-x}$ Josephson junctions using He-FIB irradiation and explores the variations of parameters with dose, evaluating their suitability within the THz range. Also, the scattering of parameters of He-FIB Josephson junctions fabricated with the same He-FIB dose is investigated. Additionally, we examine the high-frequency properties of such junctions and scrutinize the associated Shapiro steps within the THz frequency spectrum. We observe an exponential relationship between I_c and the He-FIB dose. Moreover, Shapiro steps emerge under the influence of radiation spanning from 40 GHz to as high as 1.4 THz.**

***Index Terms*—Josephson junction, HTS, $YBa_2Cu_3O_{7-x}$, He-FIB, Shapiro step, THz.**

Manuscript received 26 September 2023; revised 14 December 2023 and 5 January 2024; accepted 8 January 2024. Date of publication 12 January 2024; date of current version 26 January 2024. This work was supported in part by the Braunschweig International Graduate School of Metrology–B-IGSM, in part by the DFG Research Training Group GrK 1952/2 "Metrology for Complex Nanosystems," in part by the Laboratory for Emerging Nanometrology–LENA, in part by the Deutsche Forschungsgemeinschaft (DFG, German Research Foundation, under Germany's Excellence Strategy–EXC-2123 QuantumFrontiers–390837967, in part by DFG through Project under Grants KL930/17-1 and GO 1106/6-1, in part by the COST actions FIT4NANO under Grant CA19140, in part by SUPERQUMAP under Grant CA21144, in part by the Volkswagen Foundation and the Ministry of Science and Culture of Lower Saxony through "Quantum Valley Lower Saxony Q1" (QVLS-Q1), and in part by the MWK, Federal State of Lower Saxony, Germany, within the project "QuanTec". *(Corresponding author: M. Pröpper.)*

M. Pröpper, D. Hanisch, P. J. Ritter, M. Neumann, M. Schilling, and B. Hampel are with the Institut für Elektrische Messtechnik und Grundlagen der Elektrotechnik, Technische Universität Braunschweig, 38106 Braunschweig, Germany (e-mail: m.proepper@tu-braunschweig.de).

C. Schmid, E. Goldobin, D. Koelle, and R. Kleiner are with the University of Tübingen, Physikalisches Institut, Center for Quantum Science (CQ) and LISA+, 72076 Tübingen, Germany.

Color versions of one or more figures in this article are available at https://doi.org/10.1109/TASC.2024.3353143.

Digital Object Identifier 10.1109/TASC.2024.3353143

I. Introduction

High-temperature superconductors (HTS) have emerged as a fascinating class of materials with immense potential. Among the HTS, yttrium barium copper oxide ($YBa_2Cu_3O_{7-x}$) stands out due to its high critical temperature T_c, which significantly reduces the cooling requirements, and its capability to operate at frequencies up to 5 THz [1]. These remarkable properties make $YBa_2Cu_3O_{7-x}$ an attractive candidate for many applications. The fabrication process is crucial for achieving high reproducibility, in terms of critical current I_c and normal state resistance R_n of the Josephson junctions. $YBa_2Cu_3O_{7-x}$ Josephson junctions can be fabricated by many different methods. One commonly used method is the epitaxial growth of $YBa_2Cu_3O_{7-x}$ films on bicrystal substrates, where the Josephson junction emerges at the grain boundary [2]. The junction parameters are highly dependent on the grain boundary because defects can lead to a high spread in the I_c values of the Josephson junctions [3]. This variation can be overcome by subsequent modification of the junction width, e.g. by using gallium focused ion beam [4]. However, bicrystal substrates limit the design possibilities because the Josephson junctions can only emerge at the grain boundary.

A promising approach for manufacturing Josephson junctions involves the use of a helium focused ion beam (He-FIB) [5]. The beam is employed to directly write the Josephson junctions into the superconducting film. This forms a non superconducting barrier due to suppression of the order parameter. Previous studies have shown that the parameters of Josephson junctions scale with He-FIB dose and thus, are customizable [6]. Josephson junctions fabricated by He-FIB have already been implemented in various applications ranging from SQUIDs [7] to SFQ [8] systems. Initial investigations of Josephson junctions fabricated by He-FIB have demonstrated their applicability in the high frequency range up to 40 GHz [9] and even extending into the THz domain [10]. However, the resulting Shapiro steps are still relatively small and not very flat. Therefore, further investigations of He-FIB Josephson junctions are needed for high-frequency applications.

This study focuses on the examination of Josephson junctions created using He-FIB on prepatterned $YBa_2Cu_3O_{7-x}$ thin film microbridges. We concentrate on analyzing the Josephson junction characteristics for various doses and assess their applicability for high frequencies. The scattering of parameters I_c and R_n of Josephson junctions fabricated with the same He-FIB dose was also investigated. In addition, we examined the Josephson junctions at THz frequencies in our THz microscope [11].

II. Device Fabrication

The $YBa_2Cu_3O_{7\text{-}x}$ thin films were deposited by a pulsed laser deposition (PLD) process from polycrystalline targets on single crystal $(LaAlO_3)_{0.3}(Sr_2TaAlO_6)_{0.7}$ (LSAT) substrates. The $10 \times 10\,\text{mm}^2$ substrates were mounted in the vacuum chamber of the PLD system. The substrates were heated to a temperature of 840 °C in an oxygen partial pressure of 12 Pa. The laser fluence on the target is $2\,\text{J/cm}^2$ [12]. In this study, our PLD process results in c-axis oriented 50 nm thin $YBa_2Cu_3O_{7\text{-}x}$ films. T_c of the film is measured in a liquid nitrogen cooled dipstick by means of a susceptibility measurement. The films exhibit a T_c of 89 K with a transition width of 1 K. Uniform and smooth $YBa_2Cu_3O_{7\text{-}x}$ thin films are required for the fabrication of He-FIB Josephson junctions as the beam needs to pass evenly through the $YBa_2Cu_3O_{7\text{-}x}$ film. Thus, the mean roughness of the $YBa_2Cu_3O_{7\text{-}x}$ layer is examined by an atomic force microscope. These measurements show flat surfaces with only small precipitates of Y_2O_3. Afterwards a 150 nm gold cap layer is sputtered on the sample. The patterning of the sample is conducted by a standard photolithography process. In the first etching step the gold and the underlying $YBa_2Cu_3O_{7\text{-}x}$ layer are etched. This step is performed in an argon ion etching system optimized for a gentle etching process. The next step is to remove the gold layer in the area where the Josephson junctions are to be written. TechniEtch, a chemical etchant, is used for this purpose. TechniEtch consists of potassium iodide and iodide. Previous studies of a potassium iodide and iodide solution have shown, that the $YBa_2Cu_3O_{7\text{-}x}$ film quality and the T_c are not affected by the etchant [13]. This result could also be seen in our studies using TechniEtch.

An issue associated with He-FIB Josephson junctions is that the correlation between dose and the resulting Josephson junction properties cannot be extrapolated from one substrate to another, even if they share the same material and patterning process [6], [14]. Accordingly, it is necessary to have additional structures on a substrate so that preliminary calibrations can be carried out. This can be easily done with multiple designs on one chip. The patterning process results in two identical designs on one sample. The design consists of one ground electrode, which connects six branches of five 3 µm wide $YBa_2Cu_3O_{7\text{-}x}$ bridges. Each of the bridges can be measured individually in a four terminal sensing scheme. In Fig. 1 one branch with five bridges is shown. The shared ground electrode is visible on the left, while the individual supply lines are situated on the right side. Furthermore, the design includes orientation markers above and below the bridges for the He-FIB process. It can be seen that the gold was only etched off the $YBa_2Cu_3O_{7\text{-}x}$ bridges while there is still gold on the supply lines.

After patterning the $YBa_2Cu_3O_{7\text{-}x}$ microbridges, He-FIB irradiation is done in a *Zeiss Orion NanoFab* helium ion microscope with an acceleration voltage of 30 keV. For irradiation a beam current of 1 pA is used. The diameter of the focused ion beam is about 5 nm. By scanning the beam over the sample, barriers can be written into the thin $YBa_2Cu_3O_{7\text{-}x}$ film to form Josephson junctions. The dwell time per pixel was varied to set different dose values (ions/nm). Due to the Gaussian FIB intensity profile, different doses lead to different Josephson junction barrier thicknesses [6]. Recent studies have shown that postannealing at a certain oxygen pressure can be used to stabilize the Josephson junction properties [14]. This has not been done in this study but will be considered in the future.

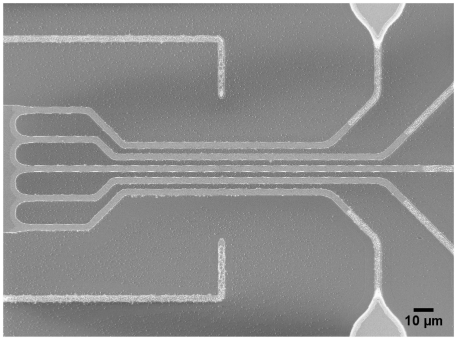

Fig. 1. Scanning electron microscopy image of a branch with five 3 µm wide $YBa_2Cu_3O_{7\text{-}x}$ bridges and He-FIB markers above and below the bridges.

In this study, a dose range of 400 to 1000 ions/nm was examined. Additionally, some of these doses were written multiple times to examine the spread of the resulting Josephson junction properties.

III. Experimental Setup

For the characterization of the samples we use four terminal sensing in a mobile pulse tube cryocooler setup, which can cool the sample down to 3 K. A sinusoidal bias current with an amplitude in the range of 10 nA to 30 mA can be applied and the voltage drop across the Josephson junctions is measured. In this study, the value of the critical current I_c is determined when surpassing the 10 µV threshold. The normal state resistance R_n is determined by examining the differential resistance of the curve at large currents $(10{\cdot}I_c)$. Based on these parameters the characteristic frequency f_c of the Josephson junctions can be calculated using (1).

$$f_c = \frac{2 \cdot e \cdot I_c \cdot R_n}{h} \tag{1}$$

The equation consists of the Josephson junction parameters R_n and I_c, the elementary charge e and Planck's constant h. The investigation of the characteristic frequency is interesting as it impacts the characteristic of the Josephson junction when irradiated with an external high frequency field. In the described measurement setup it is possible to excite the samples with a high frequency field of up to 40 GHz with a *Rohde & Schwarz SMB100 A* signal generator. The irradiation of the sample leads to a suppression of I_c and additionally to steps of constant

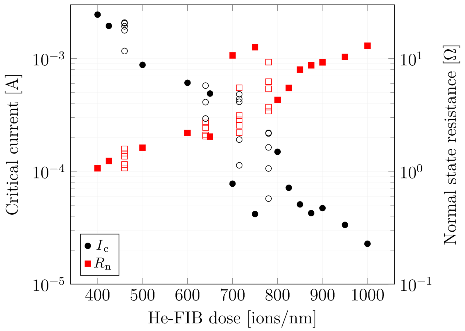

Fig. 2. I_c (circles) and R_n (squares) values of the 3 µm wide $YBa_2Cu_3O_{7-x}$ junctions vs. He-FIB dose. Open symbols show results for devices irradiated with the same dose. The measurements were taken at 5 K.

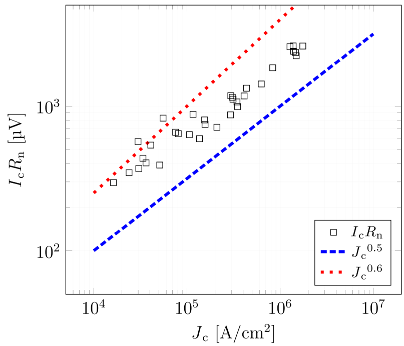

Fig. 3. $I_c R_n$ values of the 3 µm wide $YBa_2Cu_3O_{7-x}$ junctions vs. critical current density J_c at 5 K. For comparison with the measurements in [17] the scaling of I_cR_n with $J_c^{0.5}$ is shown as dashed and $J_c^{0.6}$ as dotted line.

TABLE I
KEY PARAMETERS OF HE-FIB $YBA_2CU_3O_{7-x}$ JOSEPHSON JUNCTIONS WITH DIFFERENT DOSES AT 5 K

Dose [ions/nm]	I_c [µA]	R_n [Ω]	f_c [GHz]
400	2450	1.07	1261.83
600	609	2.19	643.51
800	149	4.28	307.27
1000	22.8	13.04	143.34

voltage, so called Shapiro steps [15]. The voltage of these steps (2) is based only on natural constants and the applied frequency f_{hf}.

$$U = f_{hf} \cdot \frac{h}{2 \cdot e} \quad . \tag{2}$$

In order to obtain wide and flat steps, the ratio of the applied external frequency f_{hf} and the characteristic frequency f_c (3) must be taken into account.

$$\Omega_{hf} = \frac{f_{hf}}{f_c} \tag{3}$$

The size of the Shapiro steps primarily depends on the normalized drive frequency Ω_{hf} and the irradiation power. Wide and flat Shapiro steps at minimal power are achieved, when Ω_{hf} is close to unity. The required power correlates with I_c. This means that besides the requirement of $\Omega_{hf} = 1$, I_c should match the high frequency current in the Josephson junction induced by the external radiation. [16]

Based on (2) irradiation with higher frequency leads to a higher step's voltage. For the investigation of the influence of irradiation with THz frequencies, the samples can be measured in the THz microscope [11]. The sample is cooled with a pulse tube cryocooler to about 20 K and irradiated by an optically pumped far-infrared laser (*FIRL-100 by Edinburgh Instruments*) system.

IV. RESULTS AND DISCUSSION

First of all, we measured the bridges irradiated with different He-FIB doses on the same chip to investigate the relation between dose, I_c and R_n. The sample under test is measured by four terminal sensing. During cooling, T_c was also determined, which was still around 89 K for all bridges, regardless of the He-FIB dose. The characterization measurements are performed at 5 K. In Fig. 2 the measurements for different doses on the same chip are shown. I_c values are depicted as circles and R_n values as squares. Data for devices produced with different doses are shown as full symbols, and data for devices with same doses are shown as open symbols.

These measurements show an exponential relationship between the dose and the critical current. This is similar to the studies of different misorientation angles in grain boundary Josephson junctions [18]. Fig. 2 shows that there is a significant scatter of I_c values for all doses under test. The relative spread increases with higher doses. R_n increases with higher doses and also scales exponentially with the dose.

For most applications not only I_c and R_n are important but also their product. In Fig. 3 the I_cR_n values of the 3 µm wide $YBa_2Cu_3O_{7-x}$ junctions versus the critical current density J_c at 5 K are depicted. J_c is derived from I_c using the width of the bridge and the $YBa_2Cu_3O_{7-x}$ film thickness, assuming a uniform current distribution. From this, it can be derived that the scatter of the I_cR_n values is not as significant as in Fig. 2. The measurement data from these He-FIB Josephson junctions also match the extensive data from Ref. [17]. There it was shown that the I_cR_n product is proportional to $J_c^{0.5\pm0.1}$. This is also the case for most of the Josephson junctions depicted in Fig. 2 since they lay between the dashed $J_c^{0.5}$ and the dotted $J_c^{0.6}$ line.

From these preliminary tests, the characteristic frequency f_c of the Josephson junctions can be calculated using (1). In Table I the dependence of some key parameters of Josephson junctions at 5 K on the He-FIB dose is shown. From this, it can be deduced that a very wide range of frequencies can be covered with the used dose span.

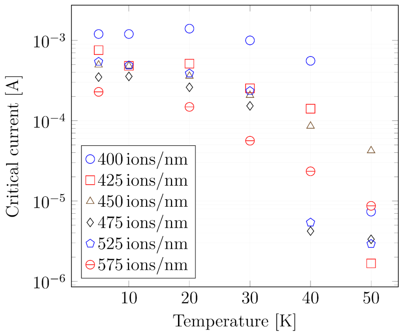

Fig. 4. I_c over temperature for different He-FIB doses.

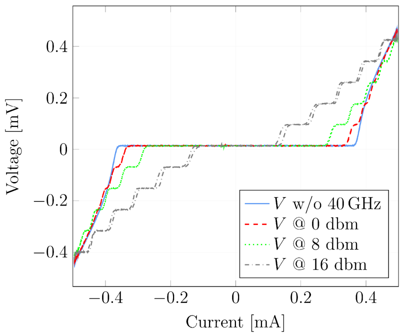

Fig. 5. IV-characteristic of a He-FIB Josephson junction in a microbridge irradiated with 40 GHz at different power levels at 30 K.

Measurements of I_c at variable temperatures are performed in the range of 5 K to 50 K. These measurements are shown in Fig. 4, where I_c is plotted logarithmically versus temperature. It can be seen that I_c decreases significantly with increasing temperature. Meanwhile R_n stays nearly constant in this temperature range. Thus, this behavior is very similar to the behavior of grain boundary Josephson junctions [19].

Further examinations address the impact of external high-frequency stimuli on the sample. For this purpose, the samples were excited with microwaves at different frequencies and powers. In Fig. 5 the IV-characteristic of a junction irradiated with 40 GHz at different power levels is shown. These measurements were performed at 30 K using a Josephson junction written with a dose of 450 ions/nm. The measurements are conducted at 30 K because the I_c is lower at this temperature with about 360 µA, while R_n stays nearly constant at about 1.7 Ω, which leads to a smaller f_c of 295 GHz. Ω_{hf} is thus closer to 1 with the applied frequency of 40 GHz.

The suppression of I_c becomes obvious at this measurement. The curve without external irradiation has the largest I_c. The

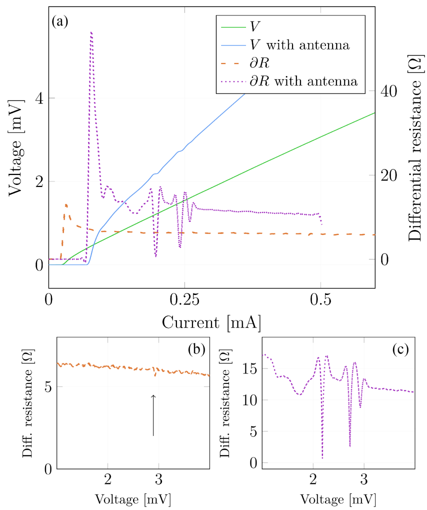

Fig. 6. Comparison of the irradiation of a single Josephson junction with and without an u-shape antenna at 20 K (a). Enlarged representations of the differential resistance vs. voltage curves without (b) and with antenna (c) over the range of frequencies investigated (1 THz, 1.3 THz, and 1.4 THz).

power level correlates clearly with increasing suppression of I_c. Flat and wide Shapiro steps can be seen at different power levels. At the highest power, hysteretic behavior can be seen, which may be explained by internal heating.

Based on the preliminary investigations, junctions with different suitable properties (high f_c with small I_c) at 20 K are used for the investigation in the THz microscope. The laser used in the THz microscope can emit several different frequencies that can be adjusted [11]. In this experiment, the laser emits the frequencies 1 THz, 1.3 THz and 1.4 THz. The suppression of I_c caused by the THz radiation can be seen for each of the examined Josephson junctions. Josephson junctions with a rather small I_c of about 100 µA (without irradiation) and high R_n of about 10 Ω at 20 K also show a very small dip in the differential resistance versus voltage curve caused by the applied frequency of 1.4 THz (see Fig. 6(b)). This phenomenon has also been demonstrated in previous studies [10] where the junctions have been irradiated with 2.5 THz. It can be guessed that the coupling efficiency of the junctions to the THz radiation is low and therefore Shapiro steps do not form with the used design (see Fig. 1). This can be improved by using antenna structures with the Josephson junction in its feed point. To enhance input coupling of the THz radiation, we have investigated another sample whose design includes antennas. U-shape antennas optimized for a high coupling efficiency in the THz range are used [20]. The junctions are directly written with He-FIB with a dose of 535 ions/nm, which results in a I_c of approximately 100 µA (without irradiation) at 20 K. This also leads to a high R_n

of about 7 Ω, which matches the impedance of the antenna (10 Ω) quite well thus increasing the coupling efficiency. A comparison between the IV-characteristic and the differential resistance ∂R of a single junction and a junction in the feed point of an u-shape antenna is shown in Fig. 6.

The measurement with an u-shape antenna shows Shapiro steps at 1 THz, 1.3 THz and 1.4 THz. From this it can be derived that the u-shape antennas lead to a better coupling efficiency to the Josephson junction.

V. Conclusion

In this work, we have demonstrated the fabrication process of $YBa_2Cu_3O_{7-x}$ He-FIB Josephson junctions and analyzed the critical current, normal state resistance and the characteristic frequency of these junctions. Further measurements with THz radiation have been conducted resulting in a small dip in the differential resistance over current for a single bridge due to a low coupling efficiency. Measurements of a $YBa_2Cu_3O_{7-x}$ Josephson junction embedded in a u-shape antenna shows clear Shapiro steps at 1 THz, 1.3 THz and 1.4 THz. It can be concluded that the He-FIB process is well suited in conjunction with $YBa_2Cu_3O_{7-x}$to fabricate Josephson junctions with customizable properties and thus is promising for the development of THz sensitive Josephson junctions.

References

[1] Y. Divin, O. Volkov, V. Pavlovskii, U. Poppe, and K. Urban, "Terahertz spectral analysis by ac Josephson effect in high-T_c bicrystal junctions," *IEEE Trans. Appl. Supercond.*, vol. 11, no. 1, pp. 582–585, Mar. 2001.

[2] H. Hilgenkamp and J. Mannhart, "Grain boundaries in high-T_c superconductors," *Rev. Mod. Phys.*, vol. 74, pp. 485–549, 2002.

[3] H. Burkhardt, O. Brugmann, A. Rauther, F. Schnell, and M. Schilling, "Very Large $YBa_2Cu_3O_7$-Josephson-junction-arrays," *IEEE Trans. Appl. Supercond.*, vol. 9, no. 2, pp. 3153–3156, Jun. 1999.

[4] D. Hanisch, M. Pröpper, P. J. Ritter, M. Tollkühn, M. Schilling, and B. Hampel, "High-T_c Josephson junction arrays for THz applications," *IEEE Trans. Appl. Supercond.*, vol. 33, no. 5, Aug. 2023, Art. no. 1501105.

[5] S. A. Cybart et al., "Nano Josephson superconducting tunnel junctions in $YBa_2Cu_3O_{7-\delta}$ directly patterned with a focused helium ion beam," *Nature Nanotechnol.*, vol. 10, no. 7, pp. 598–602, 2015.

[6] B. Müller et al., "Josephson junctions and SQUIDs created by focused helium-ion-beam irradiation of $YBa_2Cu_3O_7$," *Phys. Rev. Appl.*, vol. 11, no. 4, 2019, Art. no. 044082.

[7] E. Y. Cho, J. LeFebvre, R. C. Dynes, and S. A. Cybart, "Micrometer scale Y-Ba-Cu-O SQUID arrays fabricated with a focused helium ion beam," *IEEE Trans. Appl. Supercond.*, vol. 30, no. 9, Oct. 2020, Art. no. 1100403.

[8] H. Cai, H. Li, E. Y. Cho, J. C. LeFebvre, and S. A. Cybart, "$YBa_2Cu_3O_7$ single flux quantum flip flop directly written with a focused helium ion beam," *IEEE Trans. Appl. Supercond.*, vol. 31, no. 5, Aug. 2021, Art. no. 7200205.

[9] F. Couëdo et al., "Dynamic properties of high-T_c superconducting nanojunctions made with a focused helium ion beam," *Sci. Rep.*, vol. 10, 2020, Art. no. 10256.

[10] A. Cortez, E. Y. Cho, H. Li, D. Cunnane, B. Karasik, and S. A. Cybart, "High-frequency properties of Y-Ba-Cu-O Josephson junctions fabricated with helium ion beam irradiation," in *Proc. IEEE Int. Superconductive Electron. Conf.*, 2019, pp. 1–3.

[11] M. Tollkühn, P. J. Ritter, M. Schilling, and B. Hampel, "THz microscope for three-dimensional imaging with superconducting Josephson junctions," *Rev. Sci. Instrum.*, vol. 93, no. 4, 2022, Art. no. 043708.

[12] M. Schilling, A. Guillaume, J. M. Scholtyssek, and F. Ludwig, "Design of experiments for highly reproducible pulsed laser deposition of $YBa_2Cu_3O_{7-\delta}$," *J. Phys. D: Appl. Phys.*, vol. 47, no. 3, 2014, Art. no. 034008.

[13] W. Eidelloth and R. L. Sandstrom, "Wet etching of gold films compatible with high T_c superconducting thin films," *Appl. Phys. Lett.*, vol. 59, pp. 1632–1634, 1991.

[14] M. Karrer et al., "Temporal evolution of electric transport properties of YBCO Josephson junctions produced by focused Helium ion beam irradiation," 2023, *arXiv:2304.02749*.

[15] S. Shapiro, "Josephson currents in superconducting tunneling: The effect of microwaves and other observations," *Phys. Rev. Lett.*, vol. 11, no. 2, pp. 80–82, 1963.

[16] R. L. Kautz, "Shapiro steps in large-area metallic-barrier Josephson junctions," *J. Appl. Phys.*, vol. 78, no. 9, pp. 5811–5819, 1995.

[17] R. Gross, L. Alff, A. Beck, O. Froehlich, D. Koelle, and A. Marx, "Physics and technology of high temperature superconducting Josephson junctions," *IEEE Trans. Appl. Supercond.*, vol. 7, no. 2, pp. 2929–2935, Jun. 1997.

[18] S. Graser, P. J. Hirschfeld, T. Kopp, R. Gutser, B. M. Andersen, and J. Mannhart, "How grain boundaries limit supercurrents in high-temperature superconductors," *Nature Phys.*, vol. 6, no. 8, pp. 609–614, 2010.

[19] A. Beck et al., "Fabrication and superconducting transport properties of bicrystal grain boundary Josephson junctions on different substrates," *IEEE Trans. Appl. Supercond.*, vol. 5, no. 2, pp. 2192–2195, Jun. 1995.

[20] P. J. Ritter et al., "Antenna designs for efficient coupling to Josephson junctions for THz microscopy," *IEEE Trans. Appl. Supercond.*, vol. 33, no. 5, Aug. 2023, Art. no. 1800705.

Publication 2

Reproduced with permission from
M. Pröpper *et al.*, IEEE Trans. Appl. Supercond. **35**, 1100105 (2025)

High-T_c Josephson Junction Arrays Fabricated by He-FIB

Max Pröpper, Dominik Hanisch, Christoph Schmid, Marius Neumann, Paul Julius Ritter, Marc-André Tucholke, Edward Goldobin, Dieter Koelle, Reinhold Kleiner, Meinhard Schilling, and Benedikt Hampel

***Abstract*—The development of a fabrication process for Josephson junctions (JJs) using a direct-write helium-focused ion beam (He-FIB) technique provides the opportunity to control parameters such as the critical current I_c and normal-state resistance R_n of individual JJs in $YBa_2Cu_3O_{7-x}$ JJ arrays. Such arrays could be used as a voltage calibration standard that is operated at higher temperatures and higher driving frequencies than the currently used niobium JJ arrays. This study presents the fabrication process of 79 $YBa_2Cu_3O_{7-x}$ JJs in a meander array design using a direct writing He-FIB process with the same irradiation dose for all JJs. In this design, each of the JJs can be measured individually, and adjacent JJs that exhibit similar and suitable parameters for a voltage standard array can be measured in series. The scattering of the JJ parameters was investigated at 5 K and resulted in a spread in I_c of about 60% and in R_n of 25%. However, a couple of subarrays with a spread lower than 10% could be found. In addition, these JJ subarrays were irradiated with high-frequency radiation in the GHz and THz range at a temperature of 20 K and synchronization of up to three JJs was observed in both frequency ranges.**

***Index Terms*—He-FIB, HTS, JJ array, josephson junction (JJ), Shapiro step, THz, $YBa_2Cu_3O_{7-x}$.**

I. Introduction

Accurate calibration of our fundamental physical units is essential and a never-ending challenge of optimization. The voltage forms one of these building blocks of the International System of Units. The ac Josephson effect is used to define the unit of voltage, based on the response of Josephson junctions (JJs) to external high-frequency excitation. This response results in the formation of constant voltage steps in the current-voltage characteristic, known as Shapiro steps [1]. The voltage output for the corresponding bias current, only depends on natural constants and frequency

$$V = n \cdot \frac{h}{2 \cdot e} \cdot f. \quad (1)$$

Eq. (1) consists of Planck's constant h, the elementary charge e, the applied frequency f, and an integer n, which corresponds either to the harmonic number of the Shapiro step or the number of JJs measured in series. State-of-the-art voltage standards at NIST [2] and PTB [3] are based on niobium JJ technologies. These standards use arrays with thousands of JJs with almost identical properties connected in series, and excited at frequencies of around 20 GHz at NIST [4] and up to 70 GHz at PTB [5]. This enables output voltages of up to 10 V. These voltage standards are usually operated at or below liquid helium temperatures (4.2 K) by using e.g. a pulse tube cryocooler or a wet cryostat with liquid helium. However, by reducing the cooling requirements, the operation of a voltage standard could be simplified and made more cost-effective. Using high-temperature superconductors like yttrium barium copper oxide ($YBa_2Cu_3O_{7-x}$) would significantly lower the cooling demands, as the critical temperature T_c of $YBa_2Cu_3O_{7-x}$ is above the boiling point of liquid nitrogen (77 K). Another advantage when using $YBa_2Cu_3O_{7-x}$ is its capability to be operated at frequencies up to 5 THz [6] due to a larger energy gap compared to niobium. Higher frequencies reduce the required amount of JJs for the same output voltage compared to the niobium JJ arrays. Previous work by Klushin et al. [7] demonstrated a $YBa_2Cu_3O_{7-x}$-based voltage standard that showed a 170 µA wide and 100 mV high Shapiro step at 79.2 K. Their sample was irradiated with a frequency of 77.465 GHz. $YBa_2Cu_3O_{7-x}$ JJs can be fabricated in many different ways, such as grain-boundary JJs [8], which is the technology used by Klushin et al. [7]. A recently emerging method to fabricate $YBa_2Cu_3O_{7-x}$ JJs is the direct writing process using a focused helium ion beam (He-FIB) [9], [10]. The scanning of the beam across the sample leads to small localized modifications in the $YBa_2Cu_3O_{7-x}$, resulting in a suppression of superconductivity that can be used to fabricate Josephson barriers [11]. Earlier works have shown that the ion fluence is decisive whether a metallic or insulating

Received 25 September 2024; revised 6 December 2024; accepted 9 December 2024. Date of publication 12 December 2024; date of current version 26 December 2024. This work was supported in part by the Braunschweig International Graduate School of Metrology—B-IGSM, in part by the Laboratory for Emerging Nanometrology—LENA, in part by Deutsche Forschungsgemeinschaft (DFG, German Research Foundation, under Germany's Excellence Strategy—EXC-2123 QuantumFrontiers—390837967, in part by DFG via project under Grant KL930/17-1 and Grant GO 1106/6-1, in part by COST actions FIT4NANO under Grant CA19140 and SUPERQUMAP under Grant CA21144, and in part by Volkswagen Foundation and the Ministry of Science and Culture of Lower Saxony through "Quantum Valley Lower Saxony Q1" under Grant QVLS-Q1. *(Corresponding author: Max Pröpper.)*

Max Pröpper, Dominik Hanisch, Marius Neumann, Paul Julius Ritter, Marc-André Tucholke, Meinhard Schilling, and Benedikt Hampel are with the Institut für Elektrische Messtechnik und Grundlagen der Elektrotechnik, Technische Universität Braunschweig, 38106 Braunschweig, Germany (e-mail: m.proepper@tu-braunschweig.de).

Christoph Schmid, Edward Goldobin, Dieter Koelle, and Reinhold Kleiner are with the Physikalisches Institut, Center for Quantum Science (CQ) and LISA+, University of Tübingen, 72076 Tübingen, Germany.

Color versions of one or more figures in this article are available at https://doi.org/10.1109/TASC.2024.3516741.

Digital Object Identifier 10.1109/TASC.2024.3516741

barrier emerges in the $YBa_2Cu_3O_{7-x}$ film [12]. Initial investigations of He-FIB JJs have demonstrated their applicability to GHz and THz frequencies with small and non-flat Shapiro steps [13], [14]. In previous studies [15], we were able to show flat Shapiro steps in the GHz and THz range with He-FIB JJs. As already pointed out by Klushin et al., $YBa_2Cu_3O_{7-x}$ He-FIB JJ arrays are promising for high-temperature superconducting JJ voltage standards [16]. He-FIB $YBa_2Cu_3O_{7-x}$ JJ arrays, which increase the sensitivity of magnetic detectors were already demonstrated [17], [18]. Further studies of He-FIB JJ arrays consisting of 20 JJs have been reported. Irradiation of this array with 17 GHz resulted in a wide Shapiro step at approximately 700 μV [9]. Even though they were not analyzed for the application in a voltage calibration standard. For voltage standard applications, it is essential to investigate the requirements for synchronization of He-FIB JJs so that the flat Shapiro steps of JJs in an array add up to larger voltages.

These JJ arrays are biased with a current I and the voltage V is measured across all JJs. Thus, the measurement of a JJ array reflects the sum of the individual characteristics of the JJs within the array. This necessitates that the JJs have similar properties, such as critical current I_c and normal state resistance R_n, to ensure coherent behavior. Otherwise, one JJ could fail to display a Shapiro step while the other does under the same excitation. Another requirement is, that the I_c of individual JJs should be relatively large to minimize the influence of noise [16]. Furthermore it has to be taken into account that the Josephson energy must exceed the thermal energy by a large margin (≈ 200) in order to have stable Shapiro steps [19]. Since the Josephson energy is directly correlated to I_c it becomes obvious that large I_c values are preferred especially at higher temperatures. Several previous studies have given different information for the allowed spread of parameters which allows multiple JJs to be synchronized or phase locked. A spread of 7% in the I_c values was presented [20]. Another study showed that the I_c values can scatter by 30% as long as the R_n values are very similar, which can be achieved by shunting [7]. Another important factor is that all JJs inside an array need to be irradiated with the same high-frequency amplitude to behave similarly and form the Shapiro step at the same bias current value [5]. The frequency of that signal is also very important, which can be understood by introducing two equations that describe the characteristic frequency f_c of the JJs and the normalized drive frequency Ω_{hf}. The characteristic frequency f_c of the JJs is based on their parameters I_c and R_n and can be calculated using (2)

$$f_c = I_c \cdot R_n \cdot \frac{2 \cdot e}{h}. \qquad (2)$$

The relation of the external high frequency f_{hf} and the characteristic frequency f_c is shown in (3)

$$\Omega_{hf} = \frac{f_{hf}}{f_c}. \qquad (3)$$

The width and flatness of the Shapiro steps are optimal when the JJs are operated close to f_c, i.e. $\Omega_{hf} \approx 1$. A value for $\Omega_{hf} > 1$ implies that higher high-frequency signal amplitudes are necessary to achieve similar results [21]. Previous studies on $YBa_2Cu_3O_{7-x}$ JJ arrays have shown that the maximum width of the Shapiro steps could be observed at Ω_{hf} values of $1 \ldots 2$ [22]. For JJs inside an array to synchronize at $\Omega_{hf} < 1$, the spread in the I_c values needs to be very small [21].

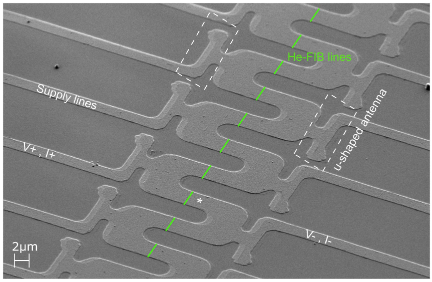

Fig. 1. Scanning electron micrograph of the meander structure with the 2 μm wide and 10 μm long $YBa_2Cu_3O_{7-x}$ microbridges. In green the He-FIB lines are shown. As example, the voltage and current connections for the four-terminal sensing scheme of the JJ marked with an asterisk are shown.

This study focuses on the examination of JJs and JJ arrays fabricated using He-FIB on prepatterned $YBa_2Cu_3O_{7-x}$ thin film microbridges. The analysis focuses on the specific JJ parameters required to achieve synchronization of Shapiro steps in JJ arrays. Therefore, the scattering of parameters like I_c and R_n was investigated. The potential arrays were examined at 20 K with high-frequency excitation up to 40 GHz in a mobile cryocooler test setup and at 1 THz in a THz microscope setup [23].

II. Device Fabrication

The investigations in this study are based on a uniform and smooth 50 nm thin $YBa_2Cu_3O_{7-x}$ film on an $(LaAlO_3)_{0.3}(Sr_2TaAlO_6)_{0.7}$ substrate. The film's root mean square surface roughness of approximately 0.8 nm was measured with an atomic force microscope. The $YBa_2Cu_3O_{7-x}$ film has a 25 nm silver and 55 nm gold cap layer on top. The fabrication process is identical to previous studies and is described in detail in [15] and [24]. The sample is patterned by a photolithography process and a subsequent 6 min etch in an argon ion beam etching system to remove the gold, silver, and the underlying $YBa_2Cu_3O_{7-x}$ layer. At the designated JJ positions, the gold and silver layers need to be removed to enable the direct writing He-FIB process. For this, a 10 s wet etch based on the potassium iodide and iodide solution TechniEtch is used. Previous studies have demonstrated that the $YBa_2Cu_3O_{7-x}$ film quality and its T_c are not significantly impaired by this type of etchant [25]. Our investigations confirm this study and show that T_c does not degrade after the use of TechniEtch.

The design used in this study, see the scanning electron micrograph in Fig. 1, consists of a meander structure with a total of 79 $YBa_2Cu_3O_{7-x}$ microbridges, each 2 μm wide and 10 μm long. The individual JJs are numbered from 1 to 79 and each JJ can be measured individually or with any number of neighboring JJs in a four-terminal sensing scheme. To perform the measurements, the sample is contacted via gold wire bonding. The gold layer on top of the $YBa_2Cu_3O_{7-x}$ film at the single bondpads is separated by small trenches. This configuration enables a four-terminal sensing scheme using only two superconducting supply lines, with the voltage connection on one part of the bondpad and current on the other. As an example, the voltage and current connections used for the JJ marked with an asterisk are shown in Fig. 1. Furthermore, the design includes u-shaped antennas at every supply line to optimize the coupling efficiency of the external high-frequency field to the JJ [26]. The positions of the JJs are indicated by green lines in Fig. 1. All JJs are written with the same He-FIB dose to create JJs with similar parameters. The field of view for the He-FIB patterning process is 30 µm × 30 µm, which allows direct writing of five JJs within one focusing step. The stage drift is below 1 nm s^{-1}, which, considering the irradiation time per JJ, is negligible. Additionally, the repeats are set to one, meaning the irradiation time is calculated for the beam to pass across each microbridge only once. The dose is calculated using measurement data from previous samples and an additional calibration sample with an identical meander array design, which employs several different He-FIB doses. The critical current density J_c and the resistivity ρ_n depend exponentially on the He-FIB dose D [10], [15]. This relation for the resistivity was also shown at 300 K by an early study on ion beam irradiation of bulk $YBa_2Cu_3O_{7-x}$ samples by Lang et al. [27]. Our calibration procedure yields the approximate empirical relations at 5 K

$$J_c \approx 2.34 \times 10^7 \frac{\mathrm{A}}{\mathrm{cm}^2} \cdot \exp\left(\frac{D}{-138\ \mathrm{ions/nm}}\right) \tag{4}$$

$$\rho_n \approx 1.05 \times 10^{-10} \Omega\,\mathrm{cm}^2 \cdot \exp\left(\frac{D}{165\ \mathrm{ions/nm}}\right). \tag{5}$$

The parameters I_c and R_n can be calculated with the help of the He-FIB dose D and the geometric properties of the JJs.

The critical current I_c should be several µA to avoid impairment by the noise level of the measurement setup. The choice of the He-FIB dose, and therefore the JJ parameters, is a trade-off between the optimal parameters for the design to be resonant at the desired frequency of 1 THz and an adequate f_c of the JJs. The design's resonant frequency depends foremost on the antenna size, but also on the surface impedance of the $YBa_2Cu_3O_{7-x}$ film and the feed point impedance, which in this case is indicated by the R_n of the individual JJs. Simulations of the resonant frequency of the used $YBa_2Cu_3O_{7-x}$ structures were performed using *CST Studio 2024*. Further information on the simulations and the procedure can be found in previous studies [26]. The simulations of the meander structure resulted in resonant peaks in the S_{11} parameters at 1 THz for R_n values of about 15 Ω. Calculating the dose and the resulting I_c value using (4) leads to an I_c of 60 µA. Since the measurements of the arrays will be conducted at 20 K, which is the lowest controllable stable temperature in the THz microscope setup [23], this I_c value is too low. This can be seen by calculating the thermal and Josephson energy, and the factor between them at 20 K [19]. Therefore, a different approach to selecting D must be chosen. Since high I_c values lead to low R_n values, a trade-off must

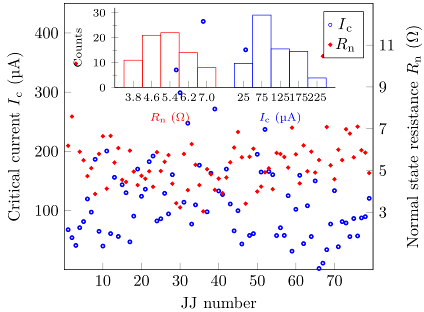

Fig. 2. I_c and R_n values of the single JJs inside the meander array versus their JJ number at 5 K. Inset shows a histogram of the distribution of the values.

also be considered here. The desired I_c is therefore selected as 150 µA at 5 K, which results in a dose of 695 ions/nm. According to (5) this results in R_n values of approximately 5 Ω for each JJ. This affects the amplitude of the S_{11} parameters. However, a peak at frequencies around 1 THz can still be observed. Using (2), f_c can be calculated. These parameters would result in an f_c value of 323 GHz at 5 K. We note, that the values of I_c and R_n can change with time after He-FIB irradiation; for details, see Ref. [28].

III. Results and Discussion

The samples are characterized using a pulse tube cryocooler setup with a base temperature of 3 K in a magnetically shielded environment made of mu-metal. Four-terminal sensing is employed for the measurements. A sinusoidal bias current with an amplitude ranging from 10 nA to 30 mA is applied, and the voltage drop across the JJs is measured. In this study, the value of I_c is determined when a threshold value of 10 µV is surpassed. R_n is determined by examining the differential resistance of the current-voltage curve at approximately $10 \cdot I_c$. In Fig. 2, the measurement results of the single JJs inside the meander array are plotted versus their assigned JJ number. All of these measurements were performed at 5 K to ensure comparability with previous data in less than ten days after the He-FIB writing process. Thus the measurements should not be affected by aging of the JJs [28].

The parameter spread of the 79 single JJs is pronounced with most I_c values ranging from 50 µA to about 300 µA and R_n values ranging from 3 Ω to 7 Ω. The inset of Fig. 2 shows a histogram of the distribution of the values. Nevertheless, the mean values over all JJs are near the desired values for I_c with 120 µA and R_n with 5.4 Ω. This leads to a mean value for f_c of 313 GHz. The standard deviations were calculated to be $\sigma_{I_c} = 78$ µA and $\sigma_{R_n} = 1.25$ Ω, which correspond to a spread of approximately 60% for the I_c values and 25% for the R_n values. Compared to the results in Ref. [17], [18], where a spread in I_c parameters at 77 K was estimated to be about 30% by a fitting model, our results reveal a larger spread. In Ref. [17], [18], no values for the scattering in R_n are provided. In Ref. [17], He-FIB-induced JJs in 10 µm to 20 µm wide bridges of a 32 nm thin $YBa_2Cu_3O_{7-x}$ film on $(LaAlO_3)_{0.3}(Sr_2\ TaAlO_6)_{0.7}$ were investigated. The differences in our results could be attributed to the larger thickness of the $YBa_2Cu_3O_{7-x}$ film, as helium ions tend to spread more as they penetrate deeper into the film [29]. Another important factor is the temperature at which the measurement was carried out. The spread in I_c decreases at higher temperatures, as shown in [24] for bicrystal JJs, which is particularly evident in our results at 5 K compared to 77 K. To ensure that the spread within the parameters does not result from variations in focusing steps during the He-FIB process, the JJs written during a single focusing step were analyzed individually and compared to those from other steps. However, this analysis did not reveal any correlations. However, small subarrays of JJs in the meander array can be found with similar parameters. Therefore I_c and R_n are investigated. Moreover, the relationship between the bias current and the resulting voltage must be considered, as the JJs are biased with the same current and need to exhibit Shapiro steps at the same current level. If all three parameters exhibit a spread of less than 10%, the result is considered similar. Using this method, up to four neighboring JJs with similar parameters can be found. These subarrays were measured and their properties at irradiation evaluated.

Using the described measurement setup, the JJ subarrays were irradiated with frequencies up to 40 GHz and input powers between −15 dBm and 15 dBm, using a *Rohde & Schwarz SMB100 A* signal generator. For this, an open semi-rigid cable is placed directly above the sample. The best results we obtained for the 40 GHz irradiation measurements were from the calibration sample with the meander structure. This sample, which includes an array of four JJs (named JJ12 to JJ15), each fabricated with a He-FIB dose of 600 ions/nm, was found to be a good candidate, with $I_c \approx 470$ µA and $R_n \approx 2.8\ \Omega$ (determined without irradiation). The bias current for the respective voltage is approximately 500 µA. It is possible to measure all of the JJs individually, in pairs (next to each other), in triplets, or all four JJs together during a single cooldown. The measurements were conducted at 20 K, as a trade-off between having a large I_c and a sufficient difference in thermal and Josephson energy. Irradiating the single JJs with 40 GHz leads to flat and wide Shapiro steps at the corresponding voltage of 82.7 µV. By comparing the responses of those single JJs, it can be seen that even though the dc parameters are very similar and the JJs are positioned directly next to each other, their behavior when irradiated is very different. This is probably due to the coupling of the high-frequency signals to the individual JJs in our measurement setup. The sample is wire bonded to a PCB and these wire bonds influence the coupling properties of the sample. This hypothesis was tested by measuring the identical JJs with the same settings, differing only in the way the wire bonds are placed. In this case, the JJs show different behavior. When a measurement is performed with all four JJs inside the array, the resulting current-voltage curve will contain the sum of the individual voltages of each JJ. Shapiro steps need to overlap at a certain bias current to synchronize. In this measurement, synchronization is only achieved with two JJs in series. The measurements of the single JJs and the pair of JJs are shown in Fig. 3.

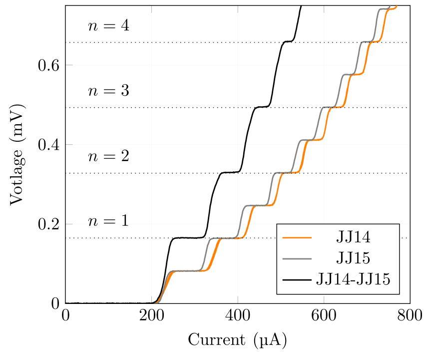

Fig. 3. Measurement of the single JJs *JJ3* and *JJ4* with 40 GHz and 10 dBm power from the signal generator excitation at 20 K are shown in orange and gray. Measurement of the pair of JJs combined is shown in black.

Since the Shapiro steps of the single JJs do have an overlap, the measurement of this pair of JJs shows a Shapiro step at the voltage $2 \cdot \mathrm{V}\,(40\ \mathrm{GHz}) = 165$ µV. Even the higher harmonic steps, up to the fourth, can be seen very clearly. The first Shapiro step has a width of 78 µA. The JJs used in this array have f_c values of about 500 GHz to 600 GHz, so $\Omega_{hf} < 0.1$, which may also explain why the other two JJs do not synchronize in this measurement [21]. By increasing the temperature, the I_c values should decrease while the R_n values stay nearly the same. So the f_c value would decrease as well, which could lead to an Ω_{hf} closer to 1 and therefore to a better synchronization. By reducing the I_c with T one has to take into account, that the measurement is more prone to noise due to appreciable $k_B T$ [16]. However, measurements of subarrays with more than two JJs have not yet shown Shapiro steps at the corresponding positioning when irradiated with 40 GHz.

Similar measurements have been conducted with irradiation of the sample with 1.04 THz using a THz microscope [23]. The measurements are conducted at 20 K. The most promising subarray consists of three JJs (JJ55 to JJ57) and has a spread of less than 7% in $I_c \approx 60$ µA, $R_n \approx 5.8\ \Omega$, and the required bias current ≈ 227 µA for the voltage $V(1.04\ \mathrm{THz}) = 2.15$ mV. These values result in an $f_c \approx 170$ GHz, and consequently, an $\Omega_{hf} \approx 6$, indicating that a significant amount of RF power is required for flat Shapiro steps [21]. Similar to the measurement at 40 GHz irradiation, it is possible to measure the JJs individually, in pairs, and all three JJs. Since Shapiro steps manifest as changes in the slope of the differential resistance, we will focus on this observable. Measurements of single JJs show a dip in the differential resistance versus voltage at the voltage corresponding to the irradiation frequency. The measurement of the two possible pairs (JJs 55–56 and 56–57) show synchronization of the JJs and thus a dip at 2.08 THz. In Fig. 4, the results of the measurement of the three JJs are shown. The differential resistance is plotted

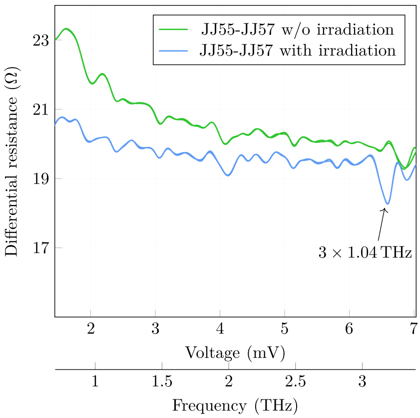

Fig. 4. Comparison of a measurement of an JJ array with three JJs with and without irradiation at 20 K. Differential resistance is plotted versus the frequency, which is calculated using the measured voltage. A synchronization of three JJs irradiated with 1.04 THz is obvious.

versus voltage, and for clarity, also versus frequency, which is calculated using (1). In this plot the differential resistance of the array with (blue) and without (green) irradiation is shown. From this, it can be derived that a synchronized Shapiro step in an array consisting of three JJs can be seen at 1.04 THz irradiation. Thus the Shapiro step is at a voltage of 6.45 mV. We expect that more pronounced Shapiro steps can be achieved with optimized antenna structures, as previously shown for single He-FIB JJs [15].

IV. Conclusion

In this work, we have demonstrated an approach to fabricate $YBa_2Cu_3O_{7-x}$ He-FIB JJ arrays, resulting in a superposition of two Shapiro steps at 40 GHz and three at 1.04 THz irradiation. Further, the spread in the individual JJ parameters and the requirements for synchronization of Shapiro steps of a meander array were investigated. It can be concluded that He-FIB $YBa_2Cu_3O_{7-x}$ JJs remain a promising candidate for high-T_c Josephson voltage standards. Future work will focus on reducing the parameter spread (e.g., using thinner films) and enabling the fabrication of arrays with more JJs, thereby achieving higher output voltages. Additionally, new designs will be investigated to improve coupling efficiency.

References

[1] S. Shapiro, "Josephson currents in superconducting tunneling: The effect of microwaves and other observations," *Phys. Rev. Lett.*, vol. 11, no. 2, pp. 80–82, 1963.
[2] (n.d.). [Online]. Available: www.nist.gov
[3] (n.d.). [Online]. Available: www.ptb.de
[4] A. Rüfenacht, N. E. Flowers-Jacobs, and S. P. Benz, "Impact of the latest generation of Josephson voltage standards in AC and DC electric metrology," *Metrologia*, vol. 55, no. 5, pp. S152–S173, 2018.
[5] R. Behr, O. Kieler, J. Kohlmann, F. Müller, and L. Palafox, "Development and metrological applications of Josephson arrays at PTB," *Meas. Sci. Technol.*, vol. 23, no. 12, 2012, Art. no. 124002.
[6] Y. Divin, O. Volkov, V. Pavlovskii, U. Poppe, and K. Urban, "Terahertz spectral analysis by AC Josephson effect in High-T_c bicrystal junctions," *IEEE Trans. Appl. Supercond.*, vol. 11, no. 1, pp. 582–585, Mar. 2001.
[7] A. M. Klushin, M. He, M. Y. Levitchev, V. V. Kurin, and N. Klein, "Optimization of the coupling of mm wave power to arrays of high-T_c Josephson junctions," *J. Phys. Conf. Ser.*, vol. 97, no. 1, 2008, Art. no. 012268.
[8] H. Hilgenkamp and J. Mannhart, "Grain boundaries in high-T_c superconductors," *Rev. Mod. Phys.*, vol. 74, pp. 485–549, 2002.
[9] S. A. Cybart et al., "Nano Josephson superconducting tunnel junctions in $YBa_2Cu_3O_{7-\delta}$ directly patterned with a focused helium ion beam," *Nat. Nanotechnol.*, vol. 10, no. 7, pp. 598–602, 2015.
[10] B. Müller et al., "Josephson junctions and SQUIDs created by focused helium-ion-beam irradiation of $YBa_2Cu_3O_7$," *Phys. Rev. Appl.*, vol. 11, no. 4, 2019, Art. no. 044082.
[11] I. A. Zaluzhnyy et al., "Structural changes in $YBa_2Cu_3O_7$ thin films modified with He^+-Focused ion beam for high-temperature superconductive nanoelectronics," *ACS Appl. Nano Materials*, vol. 7, pp. 15943–15949, 2024.
[12] E. Y. Cho et al., "$YBa_2Cu_3O_{7-\delta}$ superconducting quantum interference devices with metallic to insulating barriers written with a focused helium ion beam," *Appl. Phys. Lett.*, vol. 106, no. 25, 2015, Art. no. 252601.
[13] A. T. Cortez, E. Y. Cho, H. Li, D. Cunnane, B. Karasik, and S. A. Cybart, "Tuning Y–Ba–Cu–O focused helium ion beam Josephson junctions for use as THz mixers," *IEEE Trans. Appl. Supercond.*, vol. 29, no. 5, Aug. 2019, Art. no. 1102305.
[14] A. Cortez, E. Y. Cho, H. Li, D. Cunnane, B. Karasik, and S. A. Cybart, "High-frequency properties of Y-Ba-Cu-O Josephson junctions fabricated with helium ion beam irradiation," in *Proc. IEEE Int. Superconductive Electron. Conf.*, 2019, pp. 1–3.
[15] M. Pröpper et al., "THz properties of He-FIB $YBa_2Cu_3O_{7-x}$ Josephson junctions," *IEEE Trans. Appl. Supercond.*, vol. 34, no. 3, May 2024, Art. no. 1100505.
[16] A. M. Klushin et al., "Present and future of high-temperature superconductor quantum-based voltage standards," *IEEE Instr. Meas. Mag.*, vol. 23, no. 2, pp. 4–12, Apr. 2020.
[17] J. C. LeFebvre, E. Cho, H. Li, K. Pratt, and S. A. Cybart, "Series arrays of planar long Josephson junctions for high dynamic range magnetic flux detection," *AIP Adv.*, vol. 9, Oct. 2019, Art. no. 105215.
[18] J. C. LeFebvre and S. A. Cybart, "Large-scale focused helium ion beam lithography," *IEEE Trans. Appl. Supercond.*, vol. 31, no. 5, Aug. 2021, Art. no. 1100404.
[19] R. L. Kautz, S. P. Benz, and C. D. Reintsema, "Large-amplitude Shapiro steps and self-field effects in high- T_c Josephson weak links," *Appl. Phys. Lett.*, vol. 65, no. 11, pp. 1445–1447, 1994.
[20] K. Wiesenfeld, S. P. Benz, and P. A. A. Booi, "Phase-locked oscillator optimization for arrays of Josephson junctions," *J. Appl. Phys.*, vol. 76, no. 6, pp. 3835–3846, 1994.
[21] R. L. Kautz, "Shapiro steps in large-area metallic-barrier Josephson junctions," *J. Appl. Phys.*, vol. 78, no. 9, pp. 5811–5819, 1995.
[22] A. Klushin, E. Pestov, M. Galin, and M. Levichev, "High-temperature superconductor Josephson junctions for voltage standards," *Phys. Solid State*, vol. 58, pp. 2196–2202, Nov. 2016.
[23] M. Tollkühn, P. J. Ritter, M. Schilling, and B. Hampel, "THz microscope for three-dimensional imaging with superconducting Josephson junctions," *Rev. Sci. Instrum.*, vol. 93, no. 4, 2022, Art. no. 043708.
[24] D. Hanisch, M. Pröpper, P. J. Ritter, M. Tollkühn, M. Schilling, and B. Hampel, "High-T_c Josephson junction arrays for THz applications," *IEEE Trans. Appl. Supercond.*, vol. 33, no. 5, Aug. 2023, Art. no. 1501105.
[25] W. Eidelloth and R. L. Sandstrom, "Wet etching of gold films compatible with high T_c superconducting thin films," *Appl. Phys. Lett.*, vol. 59, pp. 1632–1634, Sep. 1991.
[26] P. J. Ritter et al., "Antenna designs for efficient coupling to Josephson junctions for THz microscopy," *IEEE Trans. Appl. Supercond.*, vol. 33, no. 5, Aug. 2023, Art. no. 1800705.
[27] W. Lang et al., "Ion beam irradiation of cuprate high-temperature superconductors: Systematic modification of the electrical properties and fabrication of nanopatterns," *Nucl. Instrum. Methods Phys. Res. Sec. B*, vol. 272, pp. 300–304, 2012.
[28] M. Karrer et al., "Temporal evolution of electric transport properties of $YBa_2Cu_3O_{7-\delta}$ Josephson junctions produced by focused-helium-ion-beam irradiation," *Phys. Rev. Appl.*, vol. 21, Jan. 2024, Art. no. 014065.
[29] J. F. Ziegler, M. Ziegler, and J. Biersack, "SRIM–The stopping and range of ions in matter (2010)," *Nucl. Instrum. Methods Phys. Res. Sec. B*, vol. 268, no. 11, pp. 1818–1823, 2010.

Publication 3

$YBa_2Cu_3O_7$ Josephson diode fabricated by focused-helium-ion-beam irradiation

Christoph Schmid,* Alireza Jozani,* Reinhold Kleiner, Dieter Koelle, and Edward Goldobin†
Physikalisches Institut, Center for Quantum Science, and LISA$^+$, Universität Tübingen, Auf der Morgenstelle 14, 72076 Tübingen, Germany

(Received 2 August 2024; revised 4 April 2025; accepted 23 June 2025; published 22 July 2025)

Using a focused He^+ beam for nanopatterning and writing of Josephson barriers, we fabricated specially shaped Josephson junctions of in-line geometry in $YBa_2Cu_3O_7$ thin film microbridges with an asymmetry ratio of critical currents of opposite polarities of approximately 7 at the optimum magnetic field. Those Josephson diodes were subsequently used as ratchets to rectify an applied alternating current into a dc voltage. We also demonstrate the operation of such a ratchet in the loaded regime, where it produces a nonzero dc output power and yields a thermodynamic efficiency of up to 75%. The ratchet shows record figures of merit: an output dc voltage of up to 212 μV and an output power of up to 0.2 nW. The device has an essential area of approximately 1 μm^2. For rectification of quasistatic Gaussian noise, the figures of merit are more modest; however, the efficiency can be as high as for the deterministic ac drives within some regimes. Since the device is based on $YBa_2Cu_3O_7$, it can operate at temperatures up to approximately 40 K, where more noise is available for rectification.

DOI: 10.1103/vqhx-16ss

I. INTRODUCTION

Superconducting diodes [1–4] and, in particular, Josephson diodes [5–11] have attracted a lot of attention in recent years. As any diodes, these devices exhibit non-point-symmetric current-voltage characteristics and, therefore, transport current in one direction better than in the other. Since these devices are superconducting, the main focus of attention is the asymmetry of the supercurrent transport—the devices have different critical currents $I_{c+} \neq |I_{c-}|$ in positive and negative directions. Thus, if one sends a current I with an absolute value between I_{c+} and $|I_{c-}|$, it will flow without dissipation in only one direction.

Systems with asymmetry (of the potential or driving force) are denoted as "ratchets." They have been investigated intensively theoretically and experimentally in the past [12–14]. A simple ratchet consists of a particle moving in a one-dimensional reflection-asymmetric potential under the action of a deterministic or stochastic force with zero time average. The ultimate goal is to rectify the applied force and produce a directed motion of the particle.

In Josephson systems, the asymmetric potential is the Josephson potential $U(\phi)$, along which a particle (Josephson phase) with coordinate ϕ moves with a velocity given by the time derivative of the Josephson phase $\dot{\phi}$. Because of the second Josephson relation, a finite velocity corresponds to a voltage across the junction. The maximum slopes of the Josephson potential in positive and negative directions are proportional to the critical currents I_{c+} and $|I_{c-}|$. Thus, for a Josephson diode with $I_{c+} \neq |I_{c-}|$, the corresponding Josephson potential is obviously not reflection-symmetric and we deal with the ratchet. In this respect, Josephson diodes and Josephson ratchets are very similar, and we will not make any distinction between them in this paper.

Different realizations of Josephson ratchets have been explored, including asymmetric superconducting quantum interference devices (SQUIDs) [15–20], Josephson vortex ratchets based on long junctions [21–24] or arrays [25–28], specially modulated Josephson junctions (JJs) [29], and tunable φ-JJ ratchets [30].

The key parameter that determines the figures of merit of Josephson diodes is the asymmetry of critical currents $\mathcal{A}$, which we define as a positive quantity between 1 and ∞:

$$\mathcal{A} = \begin{cases} |I_{c-}|/I_{c+} & \text{if } I_{c+} < |I_{c-}|, \\ I_{c+}/|I_{c-}| & \text{if } I_{c+} > |I_{c-}|. \end{cases} \quad (1)$$

Intuitively it is clear that the larger the asymmetry $\mathcal{A}$ is, the better the ratchet performs. A quantitative analysis [24, 31] shows that a large asymmetry allows one to achieve a wide operation range of driving current amplitudes, a large countercurrent (heavy load), against which rectification is still possible, and a high thermodynamic efficiency (ratio of output dc power to input ac power). So far the highest reported value for the asymmetry is around 10 [32], but in most cases the value is much lower.

*These authors contributed equally to this work.
†Contact author: gold@uni-tuebingen.de

TABLE I. Comparison of key parameters of Josephson diodes from the literature. $\mathcal{A}$ is the asymmetry (1), $\overline{V}$ is the maximum rectified voltage (for optimum drive amplitude I_{ac}), $\overline{P}_{out}$ is the maximum output power measured, η is the maximum thermodynamic efficiency reached, and A_e is defined as the area of the part of the device essential for its operation, excluding electrodes, parts that can be safely "cut off" without affecting the operation. If devices should be combined into an array, A_e is the area of one period of such an array. For many cited works we estimated A_e from the size of the minimum rectangle containing the part of the device essential for its operation. 2DEG, two-dimensional electron gas; BSCCO, ; YIG, yttrium iron garnet.

References	Type	$\mathcal{A}$	$\overline{V}$ (μV)	$\overline{P}_{out}$ (nW)	η (%)	A_e (μm^2)	T_{op} (K)
Carapella and Costabile [21]	ALJJ	1.2	5	···	···	44 500	6.5
Beck *et al.* [22]	ALJJ	2.2	20	···	···	5700	6
Sterck *et al.* [19,20]	Three-JJ SQUID	2.5	25	···	···	1125	4.2
Wang *et al.* [23]	ALJJ	2.8	100	···	···	800	4.2
Knufinke *et al.* [24][a]	ALJJ E3	1.6	40	16	25[b]	4900	4.2
Menditto *et al.* [30]	φ junction	2.5	150	···	···	2000	1.7
Golod and Krasnov [32][c]	In-line JJ	4	8	···	70[b]	7.2	7
Wu *et al.* [5]	$NbSe_2$|Nb_3Br_8|$NbSe_2$	1.07	800[d]	···	3.4[b]	3.7	0.02
Jeon *et al.* [6]	Nb|Pt + YIG|Nb	2.07	···	···	35[b]	4	2
Pal *et al.* [7]	Nb|Ti|$NiTe_2$|Ti|Nb	2.3	8[d]	···	40[b]	∼ 3	3.8
Baumgartner *et al.* [8]	Al|2DEG|Al	2	···	···	30[b]	7	0.1
Paolucci *et al.* [9]	Two-JJ SQUID	3	8	···	6[b]	72	0.4
Gosh *et al.* [10], Volkov *et al.* [11]	Twisted $Bi_2Sr_2Ca_1Cu_2O_8$ flakes	4	25[d]	···	60[b]	100	80
This work	In-line JJ	7	212	0.2	74	1.0	4.2–42

[a]In the work reported in Ref. [24], only $\overline{V}$ was measured. From Figs. 2 and 3, we determine that $I_{c-} = -0.5$ and $I_{c+} = 0.3$ in the unit of $I_0 = 2.8$ mA. We then find $I_{dc}^{opt} \approx -0.06$ corresponds to the maximum $\overline{P}_{out}$ from Eq. (18), and substitute this value into Eq. (17) to obtain the maximum $\overline{P}_{out}$. Note that the quantities in Eq. (17) are normalized. Therefore, to obtain the power in physical units, we multiply by $V_1 I_0 = 280$ nW, where $V_1 \approx 100$ μV.

[b]The efficiency was not measured experimentally but instead was *calculated* by us from the experimentally reported asymmetry using Eq. (10).

[c]Quoted asymmetry and other figures of merit are given for zero magnetic field. At the optimum magnetic field, the asymmetry is approximately 10.

[d]The authors used rectangular drive. For sine drive, the average voltage will be (substantially) lower.

Since the diodes are used for rectification, an important figure of merit is the maximum rectified voltage.

Previously demonstrated ratchets were rather large (see Table I), which hampers their integration into microelectronic or nanoelectronic superconducting circuits. Downsizing a single ratchet to submicrometer dimensions is desirable for building nanorectifiers of noise as well as for connecting many of them in series to obtain larger rectified voltages.

Operation over a wide temperatures range T is beneficial. Obviously, the upper limit of the operation temperature is given by the transition temperature T_c of the superconducting material used, so the use of high-T_c superconductors is very desirable.

An advantage of some of the diodes proposed recently is that they are based on specially engineered superconducting materials [1,2,5] and, therefore, can be structured down to the nanoscale, say, 50–100 nm. In addition, some of them [2,5,6] exhibit an asymmetry even at zero magnetic field. However, the reported asymmetry values are mostly low. In Table I we compare the figures of merit for Josephson diodes. The critical temperature T_c of the materials used is often below 4 K, which prohibits operation even in liquid He at $T = 4.2$ K. One notable exception is reported in Ref. [10].

In this work we report a Josephson diode with asymmetry $\mathcal{A} \approx 7$ and a small active device area of approximately 1 μm^2, implemented with $YBa_2Cu_3O_7$ (YBCO), enabling operation at temperatures up to approximately 40 K. To achieve a high I_c asymmetry, we use JJs of in-line geometry, which exhibit a skewed $I_c(B)$ dependence and show significantly different values of I_{c+} and $|I_{c-}|$ in an optimally chosen magnetic field.

II. FABRICATION

The fabrication of the devices starts on a 10 × 10 mm^2 chip, purchased from Ceraco GmbH. The chip consists of a 1-mm-thick (001)-oriented $(LaAlO_3)_3(Sr_2AlTaO_6)_7$ substrate, with a 20 nm CeO_2 buffer layer, followed by a $d =$ 30 nm YBCO film, both grown epitaxially. Subsequently, a 20-nm-thick Au layer was deposited for electrical contacting. Micropatterning was done in two steps. First, using Ar ion milling down to the substrate, we define a number of 200-μm-long and $W \approx 4$ μm wide microbridges (YBCO plus Au) that are connected to larger contact pads for wire bonding. Second, we use wet etching to remove the Au layer from the microbridges in the regions designated for focused-He-ion-beam nanostructuring and also between the pads to separate the voltage and current contacts.

To define the JJs and the circuit geometry, we used a focused He ion beam [33]. By writing a line across a YBCO bridge with a *moderate* irradiation dose $D \sim$ 500–700 ions/nm, the focused-He-ion-beam irradiation creates a Josephson barrier [34–38]. The corresponding JJ exhibits [36] a resistively shunted junction (RSJ)-like I-V characteristic (IVC) with Stewart-McCumber parameter $\beta_C \sim 1$. Typically $I_c(T)$ of such JJs vanishes with increasing T at $T \approx 40$ K [34,35]. Instead, by writing a line with a *high* dose $D \sim 2000$ ions/nm, one creates a barrier without supercurrent. Its resistance diverges as $T \to 0$, reaching at least few megaohms at our main working temperature of 4.2 K [36]. Transmission electron microscopy analysis shows that on the atomic scale the resistive barrier corresponds to amorphized YBCO along the irradiated line [36] and mechanically stressed crystalline YBCO in the 50–100 nm vicinity of the amorphized region [39]. Further, we use the term "amorphous resistive wall" (ARW) to remind the reader about both structural and electrical properties. Thus, one can use a focused He ion beam to draw both ARWs and JJs.

The JJ ratchets were then created in one focused-He-ion-beam nanofabrication step to produce JJ barriers and ARWs in the in-line JJ design, which is described in the next section. The dose for writing the JJ barriers was chosen to obtain the target j_c values; see below. The ARWs were always written with $D = 2000$ ions/nm.

III. DESIGN

One possibility to realize a highly asymmetric ratchet is to use a JJ with an in-line geometry, where the bias current is injected into and collected from one side of the JJ, which creates a self-field [40]. However, in our case of a very thin film, kinetic inductance rather than geometric inductance is dominant, which means that the bias current induces a phase gradient rather than a self-field. Such JJs in an externally applied magnetic field B exhibit a skewed point-symmetric $I_c(B)$ dependence. Thus, there are field values where the critical currents in the positive and negative directions are very different; see Appendix B for the theoretical background.

A helium-ion-microscope image of the device is shown in Fig. 1. The ARWs compel the bias current to flow as indicated by the thick arrows, i.e., the bias current I is injected into and extracted from the (left) side and flows parallel to the JJ barrier of length L and across it. The spacing between the barrier and the ARWs is denoted as the electrode width w. Usually, for such an in-line geometry one observes a significant self-field effect, i.e., a nonuniform magnetic field caused by and proportional to the bias current. This results in a skewed dependence of the critical current I_c on the magnetic field B applied perpendicular to the thin film plane [40]. For our very thin YBCO film with thickness $d \ll \lambda_L$ (typically $\lambda_L \approx 250$ nm for YBCO films), kinetic inductance dominates. Therefore, it is more correct to speak about a phase gradient (of the macroscopic wave functions in the superconducting electrodes) along the barrier instead of a magnetic field caused by the in-line bias configuration. Similar designs were proposed [41] as diodes very recently and used for Nb|Cu-Ni|Nb JJs [42] and YBCO grain-boundary JJs [43,44], but for different purposes.

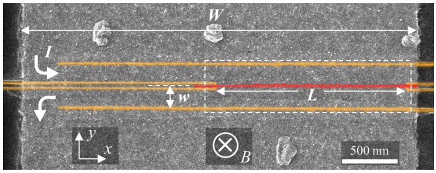

FIG. 1. Secondary electron helium-ion-microscope image of a reference microbridge (A15) of the same geometry as device A22 discussed in Sec. IV. For better visibility, A15 has been irradiated with a high-dose focused He ion beam producing an ARW also at the place of the Josephson barrier. The focused-He-ion-beam lines are colored to indicate where device A22 has ARWs (golden) written by a high-dose focused He ion beam and the Josephson barrier (red) written by a moderate-dose focused He ion beam. The thick arrows show the direction of bias current flow. The width of the whole YBCO bridge is W, the JJ length is L, and the electrode width, i.e., the distance between the JJ barrier and the upper and lower ARWs, is w. The dashed (white) rectangle shows the essential area A_e of the diode.

The planar thin-film JJs used in this work, even in the simplest geometry when the JJ crosses the whole bridge, are nonlocal [45]. Our geometry (see Fig. 1) is even more complicated than the one in Ref. [45].

A theoretical treatment of the $I_c(B)$ dependence for our JJ geometry has not been developed so far. Therefore, the estimations of target parameters for our JJ ratchets are possible only approximately, in the framework of the usual local model; see Appendix B. There we find that the key parameter that defines the asymmetry of the $I_{c\pm}(B)$ curves is the so-called *in-line geometry parameter*

$$f_I = \frac{1}{4\pi}\left(\frac{L}{\lambda_J}\right)^2; \tag{2}$$

see Appendix A for an estimation of the Josephson length λ_J. There it is shown that

$$\lambda_J^2 \propto \frac{w}{j_c \lambda_L^2}. \tag{3}$$

Further, having f_I, we can calculate the dependences of the normalized critical current $i_{c\pm} = I_{c\pm}/I_{c0}$ ($I_{c0} \equiv j_c L d$)

on the applied normalized magnetic flux $f = \Phi/\Phi_0$ ($\Phi_0 \approx 2.068 \times 10^{-15}$ Wb is the magnetic flux quantum) for different values of f_I. We find that with increasing f_I, the maximum asymmetry $\mathcal{A}_{\max}$, i.e., $\mathcal{A}$ at the optimum value $f_{\rm opt}$ of f, increases rapidly and diverges for $f_I \geq f_I^* = \pi/4$. This happens because the smaller critical current $\min(|I_{c\pm}(B)|)$ vanishes. Experimentally, this divergence is suppressed since there is always a finite background I_c value. Accordingly, we estimate practically achievable values for $\mathcal{A}_{\max} \sim 10$. For details, see Appendix B.

Guided by predictions of the local model, we chose the target parameters, such as D (i.e., j_c), L, and w, to achieve the desired asymmetry and reasonable critical current.

The JJ physical length L was chosen to have the in-line geometry parameter $f_I \approx \pi/4$, i.e., $L \approx \pi\lambda_J$, to achieve maximum possible asymmetry $\mathcal{A} \sim 10$ at the optimum flux bias point $f_{\rm opt}$; see Appendix B. In this way, the JJ also remains in the short JJ limit. Since one of our goals is to make the device as small as possible, we would like to have L as small as possible, i.e., as small as possible λ_J.

The width w between the ARWs and the JJ barrier should be chosen as small as possible to reduce λ_J and, accordingly, to reduce the size ($L \times w$) of the diode. However, w is limited by the mechanical damage around the ARWs.

Finally, the dose D was chosen to obtain j_c values that provide JJs with RSJ-like IVCs [36] at $B = 0$ and to have a reasonable maximum critical current $I_{c0} = j_c dL$ in the range 5–30 μA at $T = 4.2$ K. Such values of I_{c0} are easily measurable, and later allow us to investigate not only the limit of small thermal fluctuations $k_B T/E_J(T) \ll 1$ but also the limit of large thermal fluctuations in a reasonably broad temperature range within out target temperature range of 4.2–42 K. Here $E_J(T) = \Phi_0 I_{c0}(T)/2\pi$ is the temperature-dependent Josephson energy. We note that $j_c(T)$ affects λ_J.

In the end, we have fabricated and tested a set of several diodes with the parameters distributed around the target parameters of the local model.

IV. EXPERIMENTAL RESULTS

In total we fabricated 47 devices with $L = 500$–2000 nm, $w = 100$–1000 nm, and $D = 50$–700 ions/nm. Twelve of them worked well, i.e., showed nice IVCs and $I_c(B)$ dependences. Five of them showed asymmetry $\mathcal{A} > 2$. Here we present experimental data only for the device A22 with $L = 1750$ nm and $w = 200$ nm. The barrier was written with $D = 530$ ions/nm, which resulted in a maximum $I_{c0} \approx 14$ μA at $T = 4.2$ K (see below). Thus, $j_c \approx 27$ kA/cm^2 and $\lambda_J \approx 1.25$ μm at 4.2 K; see Appendix A for details.

A. Characterization

The electric transport measurements are done in a four-point configuration and were performed in liquid He at $T = 4.2$ K. The IVC of device A22 at $B = 0$ is shown in Fig. 2(a). The IVC is RSJ-like with symmetric critical currents and without hysteresis. To find the optimum working point of the ratchet, we measured the dependence $I_c(B)$. The field was applied perpendicular to the sample plane by means of a coil. The $I_c(B)$ dependence is shown in Fig. 2(b). The optimum working point corresponds to the maximum of $\mathcal{A}$; see the definition (1). Using the data from Fig. 2(b), we display $\mathcal{A}(B)$ in the same plot to determine the value of $B_{\rm opt}$, where $\mathcal{A}(B)$ has its maximum of approximately 7. Figure 2(a) also shows the IVC of the ratchet at $B = B_{\rm opt}$. The critical currents are rather asymmetric.

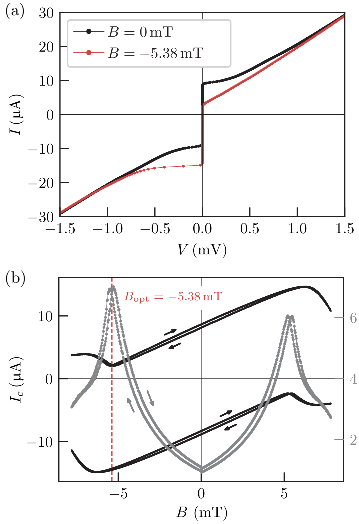

FIG. 2. Electric transport data for sample A22 taken at $T = 4.2$ K: (a) IVCs measured in both bias-current sweep directions at $B = 0$ (black) and at the optimum applied field $B_{\rm opt}$ (red). $I_{c+}(0) \approx |I_{c-}(0)| \approx 10$ μA, while $I_{c+}(B_{\rm opt}) \approx 2.0$ μA and $|I_{c-}(B_{\rm opt})| \approx 14.2$ μA, which results in $\mathcal{A}(B_{\rm opt}) \approx 7$. All $I_c(B)$ values are obtained with a voltage criterion of 1 μV. Both IVCs are somewhat rounded around the critical currents due to thermal fluctuations and nonuniformities of the JJ, so $I_{c\pm}$ could be determined experimentally only approximately. (b) $I_{c\pm}(B)$ measured in both B sweep directions (black) and $\mathcal{A}(B)$ (gray) numerically calculated from the $I_{c\pm}(B)$ data. The optimum field $B_{\rm opt} \approx -5.38$ mT.

B. Quasistatic deterministic drive

For demonstration of the ratchet operation in a quasistatic deterministic regime, we apply $B = B_{\rm opt}$ to induce the maximum $\mathcal{A}$ and drive the ratchet with a sinusoidal current [46]

$$I(t) = I_{ac} \sin(2\pi f t), \tag{4}$$

where we typically use $f = 200$ Hz, i.e., we operate in the adiabatic regime $f \ll f_c$ [18,19,47], with the characteristic frequency $f_c = I_c R/\Phi_0 \sim 300$ GHz, where $R \approx 50\ \Omega$ is the JJ normal resistance. For a continuously applied signal (4), we measure the voltage $\overline{V}$ averaged over one period of the drive [48]. By repeating the measurement of $\overline{V}$ for different values of I_{ac}, we obtain the *rectification curve* $\overline{V}(I_{ac})$ shown in Fig. 3(a) as the red curve, labeled with "idle," which means that the drive is a pure ac drive without any dc countercurrent, i.e., $I_{dc} = 0$. One can see that for very low amplitudes $I_{ac} \lesssim I_{c+}$ the rectification is absent as the ac bias point never reaches the voltage branches of the IVC during ac driving. For $I_{c+} \lesssim I_{ac} \lesssim |I_{c-}|$ the bias point reaches only the positive voltage branch of the IVCs during the positive semiperiod, which results in a finite $\overline{V}$ that grows with I_{ac} until $\overline{V}(I_{ac})$ reaches its maximum value $\overline{V}_{max}$ at $I_{ac,max} \approx |I_{c-}|$. Finally, at $I_{ac} \approx I_{c-}$ the bias point also reaches the negative voltage branch of the IVC during the negative semiperiod, and the average voltage drops with further increase of I_{ac} and asymptotically approaches zero for $I_{ac} \gg |I_{c-}|$ [49].

The rectification is *efficient roughly* for I_{ac} between I_{c+} and I_{c-} [50]. If one wants to construct a ratchet that rectifies a large range of input amplitudes, one should ideally have $I_{c+} \ll |I_{c-}|$ (or $|I_{c-}| \ll I_{c+}$), i.e., large $\mathcal{A}$. We observe a maximum rectified voltage $\overline{V} \approx 212\ \mu$V, which is one of the best among similar devices (see Table I).

Up to now our ratchet is idle, i.e., it does not produce any output power. In terms of a particle in an asymmetric periodic potential, this means that the particle is driven by a pure ac drive to the right, but stays roughly at the same energy. To produce work, one has to load the ratchet. One possibility [24] is to tilt the potential in such a way that the ratchet effect will transport the particle uphill. In this case one can also address the question of how strong the ratchet is, i.e., against which countertilt the ratchet can still transport the particle. Experimentally, it is rather easy to tilt the potential by applying an additional dc bias countercurrent to the JJ. If our rectified voltage $\overline{V} > 0$, then one needs a countercurrent $I_{dc} < 0$. Then the total applied current is given by

$$I(t) = I_{ac} \sin(2\pi f t) + I_{dc}. \tag{5}$$

The rectification curves

$$\overline{V}(I_{ac}) = \frac{1}{T} \int_0^T V(I(t))\ \mathrm{d}t \tag{6}$$

for several I_{dc} values are shown in Fig. 3(a). One can see that transport against the countercurrent still occurs, i.e.,

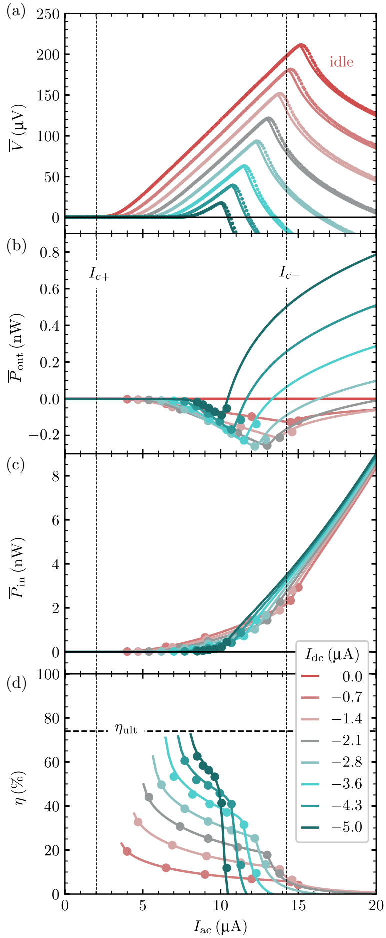

FIG. 3. Performance of the Josephson ratchet (sample A22) vs ac drive amplitude I_{ac} ($f = 200$ Hz) at $B = B_{opt}$ for different values of the countercurrent $I_{dc} \le 0$. (a) Rectification curves $\overline{V}(I_{ac})$, (b) output power $P_{out}(I_{ac})$, (c) input power $P_{in}(I_{ac})$, and (d) efficiency $\eta(I_{ac})$. Symbols show experimental data. Lines are calculated from the high-resolution experimental IVC as described in the main text.

$\overline{V} > 0$, although the average voltage (particle speed) and, accordingly, the maximum average voltage $\overline{V}_{max}$ decrease with increasing I_{dc}. The rectification range shrinks with increasing $|I_{dc}|$, and for large I_{ac} the transport reverses

($\overline{V} < 0$). The stopping current, i.e., the (minimum) countercurrent, for which the ratchet does not transport anymore in the easy direction for any I_{ac}, is theoretically given by [24] $I_{stop} = (I_{c+} - |I_{c-}|)/2 \approx -6.1$ μA, which agrees quite well with the data presented in Fig. 3(a). Note that the ratchet loaded with $I_{dc} < 0$ produces negative $\overline{V}$ at large I_{ac}. This motion in the difficult direction is simply caused by the applied I_{dc}, which overweights the ratchet effect.

Since the ratchet with $I_{dc} < 0$ transports the particle uphill, it produces an average output power

$$\overline{P}_{out} = \frac{1}{T}\int_0^T V(I(t))I_{dc}\,dt = \overline{V}I_{dc}. \tag{7}$$

Thus, to obtain $\overline{P}_{out}(I_{ac})$ plots, one should multiply each $\overline{V}(I_{ac})$ curve from Fig. 3(a) by the corresponding value of I_{dc}. The result is shown in Fig. 3(b). Note that since $I_{dc} \leq 0$, we formally get $\overline{P}_{out} \leq 0$, which means that we generate power rather than consume it. Obviously, the idle ratchet with $I_{dc} = 0$ produces $\overline{P}_{out}(I_{ac}) \equiv 0$. Then by increase of the countercurrent $|I_{dc}|$, the amplitude of $\overline{P}_{out}(I_{ac})$ curves first increases and then decreases in accordance with the product in Eq. (7), where the amplitude of $\overline{V}(I_{ac})$ decreases with $|I_{dc}|$ down to zero at I_{stop}, where $\overline{V}(I_{ac})$ and $P_{out}(I_{ac})$ change sign. Note that in the parts of the curves where $P_{out} > 0$, corresponding to parts with $\overline{V} < 0$ in Fig. 3(a), the ratchet consumes the power from the dc countercurrent source. Thus, the maximum output power in the $P_{out} < 0$ regime is expected for an intermediate load between 0 and I_{stop}.

Similarly, the input power is given by

$$\overline{P}_{in} = \frac{1}{T}\int_0^T V(I(t))I_{ac}\sin(2\pi f t)\,dt. \tag{8}$$

Equation (8) cannot be simplified in a similar way as Eq. (7). Therefore, to determine $\overline{P}_{in}$, one needs simultaneously measured $I_{ac}\sin(2\pi f t)$ and $V(t)$ profiles. They were measured for six different values of I_{ac} for each I_{dc} value. The results are presented in Fig. 3(c) as symbols. Roughly, one notes three regions in the plots. For low I_{ac}, the power vanishes as the ratchet never enters the voltage state. For intermediate values of I_{ac} [see the branches with a slight slope in Fig. 3(c)], the ratchet dissipates power only in the positive voltage branch during some part of the positive semiperiod of the drive. Finally, for large I_{ac} [see the branches with a strong slope in Fig. 3(c),] the ratchet dissipates even more power during both positive and negative semiperiods.

In the quasistatic regime of operation, all information on the ratchet performance and its figures of merit are contained in the IVCs. Therefore, having a high-resolution experimental $V(I)$, one can calculate all characteristics, such as $\overline{V}(I_{ac})$, $\overline{P}_{in}$, and $\overline{P}_{out}$, for different values of the load I_{dc} numerically, by "applying" the current $I(t)$ given by Eq. (5) to the IVC and calculating the integrals (6)–(8) numerically. In this way one can produce many points per curve. The results are presented in Fig. 3 as solid

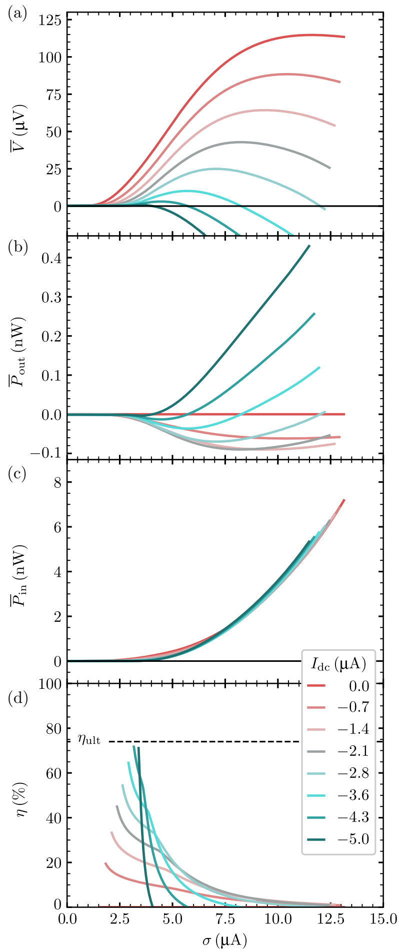

FIG. 4. Performance of the Josephson ratchet calculated from the IVC at $B = B_{opt}$ of sample A22 vs the noise amplitude σ of a quasistatic stochastic drive current for different values of the countercurrent $I_{dc} \leq 0$. (a) Rectification curves $\overline{V}(\sigma)$, (b) $\overline{P}_{in}(\sigma)$, (c) $\overline{P}_{out}(\sigma)$, and (d) $\eta(\sigma)$. For the calculations we used a 3σ cutoff during integration; see Eq. (C3) and the following text.

lines and show only a minor difference with experimental measurements.

Finally, having $\overline{P}_{\text{out}}$ and $\overline{P}_{\text{in}}$, one can calculate the *thermodynamic efficiency*

$$\eta(I_{\text{ac}}) \equiv -\frac{\overline{P}_{\text{out}}(I_{\text{ac}})}{\overline{P}_{\text{in}}(I_{\text{ac}})}. \tag{9}$$

Note that the *thermodynamic efficiency* η should not be confused with the "efficiency" given by

$$\eta_{\text{ult}} = \left|\frac{|I_{c-}| - |I_{c+}|}{|I_{c-}| + |I_{c+}|}\right| \equiv \frac{\mathcal{A}-1}{\mathcal{A}+1} \tag{10}$$

used in many publications. On the one hand, η_{ult} characterizes the degree of asymmetry of critical currents and can be expressed via $\mathcal{A}$ used in this work. On the other hand, η_{ult} represents the maximum possible, so-called ultimate [24,31], thermodynamic efficiency that can be reached for a given asymmetry theoretically.

A set of $\eta(I_{\text{ac}})$ curves for different load values is shown in Fig. 3(d). Each $\eta(I_{\text{ac}})$ curve has a sharp maximum at the beginning of the rectification window, as predicted by the model [24,31]. As a function of I_{dc}, the $\eta(I_{\text{ac}})$ curves reach their maximum amplitude for a large countercurrent $|I_{\text{dc}}|$ close to I_{stop}, where the rectification window is tiny. In this regime the value of η approaches its theoretical value η_{ult} (approximately 75% for device A22).

We note that the efficiency is not calculated for $I_{\text{ac}} < I_{c+}$. In this range, both $\overline{P}_{\text{out}} \to 0$ and $\overline{P}_{\text{in}} \to 0$, so η has a very large uncertainty. Any experimental or numerical error in $\overline{P}_{\text{in}}$ will result in a huge fluctuation of η. In other words, η will have error bars much larger than the value of η itself. Therefore, the calculation of η was not performed if $\overline{P}_{\text{in}}$ was smaller than a certain limit, typically 5 pW. This is a common problem for the evaluation of the performance of any ratchet operated with small drive amplitudes.

The rectification of the quasistatic Gaussian noise is presented in Appendix C.

V. CONCLUSIONS

We demonstrated the design, fabrication, and quasistatic operation of a Josephson diode "drawn" into a YBCO thin film microbridge using a focused He ion beam. The ratchet shows record figures of merit (see Table I), and its direction of rectification depends on the sign of the applied field. In particular, the ratchet occupies an *essential* area of approximately 1 μm^2, which is the smallest in Table I. At the optimum magnetic field, the ratchet shows an impressive asymmetry $\mathcal{A} \approx 7$, close to that of a similar design based on Nb [32,42]. As a consequence, it demonstrates a maximum rectified voltage $\overline{V} \approx 212$ μV for a sine drive and $\overline{V} \approx 115$ μV for a random Gaussian drive. In both cases the ratchet shows a large stopping force in accordance with the value of $\mathcal{A}$ (see Refs. [24,31]), and thermodynamic efficiency approaching the theoretical limit in certain regimes. However, there is a general trade-off between the maximum output power and maximum efficiency that occurs at different values of parameters such as the drive amplitude and the counterforce. The only ratchet in Table I that shows larger (estimated) output power is the one reported in Ref. [24]. There, the ratchet design was a large annular long Josephson junction (ALJJ) with very high I_c.

Preliminary measurements show that the ratchets discussed in this paper operate at temperatures up to approximately 40 K, where the critical currents of the JJ tend to zero, while the thermal energy increases by 1 order of magnitude. Detailed results for the noise-driven ratchet will be published elsewhere.

ACKNOWLEDGMENTS

This work was funded by the Deutsche Forschungsgemeinschaft via Projects No. GO-1106/6 and No. KL-930/17. A.J. thanks his father for financial support during his study. We thank M. Turad and R. Löffler for invaluable help with the Zeiss Orion NanoFab He ion microscope.

DATA AVAILABILITY

The data that support the findings of this article are openly available [51].

APPENDIX A: ESTIMATING λ_J

To estimate λ_J we use the usual expression [40]

$$\lambda_J = \sqrt{\frac{\Phi_0}{2\pi \ell_J j_c}}, \tag{A1}$$

rewritten explicitly isolating ℓ_J—the inductance per JJ length times the thickness d of the superconducting electrodes forming the JJ when the current flows along the Josephson barrier [unit of henries (volt seconds per ampere), like for inductance] [52]. Thus, in our planar case, the total inductance of the two pieces of superconducting films on both sides of the barrier is given by $L_\Sigma = \ell_J L/d$.

In our particular case $\ell_J = 2\ell$, where ℓ corresponds to one superconducting electrode. The JJ barrier thickness is considered to be negligible in comparison with the electrode width w. The total inductance L_{el} of a piece of superconducting electrode of length L and (film) thickness d is given by $L_{\text{el}} = \ell L/d$, i.e., $L_\Sigma = 2L_{\text{el}}$.

In our ultrathin-film limit ($d = 30$ nm, while the London penetration depth $\lambda_L \approx 250$ nm) we can safely assume that the inductance is purely kinetic. So when the current flows in the superconducting film along the barrier of the JJ, the associated kinetic energy is given by

$$E_k = n_s \frac{m v_s^2}{2} V', \tag{A2}$$

where $V' = Lwd$ is the volume of the film, while m, n_s, and v_s are the mass, concentration, and average velocity of "superconducting" electrons, respectively. Using the relation for the supercurrent density $j_s = n_s v_s e$, we can rewrite Eq. (A2) as

$$E_k = \frac{m j_s^2}{2 n_s e^2} Lwd = \frac{m I_s^2}{2 n_s e^2 w^2 d^2} Lwd = \frac{mL}{n_s e^2 wd} \frac{I_s^2}{2}, \tag{A3}$$

where we have introduced the supercurrent $I_s = j_s wd$, which assumes a homogeneous j_s in our electrodes with $w \ll \lambda_{\rm eff} = \lambda_L^2/d$. We recall that in the framework of the London theory

$$\lambda_L^2 = \frac{m}{\mu_0 n_s e^2}. \tag{A4}$$

Thus,

$$E_k = \mu_0 \lambda_L^2 \frac{L}{wd} \frac{I_s^2}{2}. \tag{A5}$$

The kinetic inductance is therefore given by

$$L_k = \mu_0 \lambda_L^2 \frac{L}{wd}, \tag{A6}$$

i.e.,

$$\ell = \mu_0 \lambda_L^2 \frac{1}{w}. \tag{A7}$$

For our $w = 200$ nm, we get $\ell_J = 2\ell = 0.79$ pH. This, according to Eq. (A1) with $j_c = 27\ \mathrm{kA/cm^2}$, gives $\lambda_J \approx 1.2\ \mu$m.

Quantitatively, the inductance of the JJ barrier of length L (Josephson inductance at infinitesimal current, see Ref. [40]) is given by

$$L_J = \frac{\Phi_0}{2\pi I_c} = \frac{\Phi_0}{2\pi j_c L d}. \tag{A8}$$

Assuming that $L \to \infty$ ($L \gg \lambda_J$), λ_J is the characteristic length across which the bias current injected from the edge is distributed and tunnels through the JJ barrier. At this length the Josephson inductance of the λ_J piece of the barrier is equal to the inductance of the λ_J piece of both electrodes, i.e.,

$$L_J|_{L=\lambda_J} = 2\, L_k|_{L=\lambda_J}\,.$$

Inserting L_k and L_J from Eqs. (A6) and (A8), we obtain

$$\frac{\Phi_0}{2\pi j_c \lambda_J d} = 2\mu_0 \lambda_L^2 \frac{\lambda_J}{wd}.$$

From this we obtain

$$\lambda_J^2 = \frac{\Phi_0 wd}{2\pi j_c d 2\mu_0 \lambda_L^2} = \frac{\Phi_0 w}{2\pi j_c 2\mu_0 \lambda_L^2} = \frac{\Phi_0}{2\pi j_c \ell_J},$$

i.e., exactly as given by Eq. (A1) with $\ell_J = 2\ell$ from Eq. (A7).

APPENDIX B: IN-LINE GEOMETRY

1. Derivation of $I_c(B)$

Following Ref. [40], we consider a JJ of in-line geometry spanning x from $-L/2$ to $+L/2$. The bias current I is injected into and collected from the left side of the superconducting electrodes. We assume that the JJ is short, i.e., $L \lesssim 4\lambda_J$, and, for now, we assume zero applied magnetic field. The bias current is distributed along the whole JJ length L to tunnel through the barrier. Since the JJ is short, we assume that the Josephson phase $\phi(x)$ is almost constant across the barrier. In this case, the Josephson current density across the barrier $j_s(x)$ is constant too. Then we write a current continuity (first Kirchoff) equation at an arbitrary point x inside the JJ:

$$I_L(x + \mathrm{d}x) - I_L(x) = j_s(x)\,\mathrm{d}x\, d,$$

which for $\mathrm{d}x \to 0$ gives

$$\frac{\partial I_L(x)}{\partial x} \equiv I_L'(x) = j_s(x) d, \tag{B1}$$

where $I_L(x)$ is the current flowing along the top superconducting electrode. Considering our in-line biasing scheme, the boundary conditions for $I_L(x)$ are

$$I_L(-L/2) = I, \quad I_L(+L/2) = 0. \tag{B2}$$

By solving Eq. (B1) with the boundary conditions (B2), we get an explicit expression for $I_L(x)$:

$$I_L(x) = -j_s d[x - L/2] = -I\left[\frac{x}{L} - \frac{1}{2}\right], \tag{B3}$$

where we have used the obvious fact that the whole bias current finally tunnels through the JJ, i.e., $I = j_s dL$.

The current $I_L(x)$ flowing through the kinetic inductance $\mathrm{d}L_k$ of the $\mathrm{d}x$ piece of the top (bottom) electrode creates a

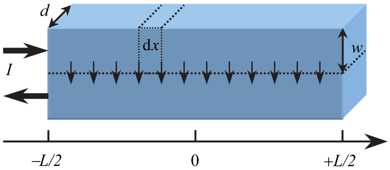

FIG. 5. JJ of in-line geometry consisting of two superconducting films and a very thin barrier (dotted lines). The arrows indicate the current I injected and collected at the left edge and flowing through the barrier.

phase difference of the macroscopic wave function of the electrode

$$\theta(x+\mathrm{d}x)-\theta(x)=\frac{2\pi}{\Phi_0}\mathrm{d}L_k I_L(x)=\frac{2\pi}{\Phi_0}\mu_0\lambda_L^2\frac{\mathrm{d}x}{wd}I_L(x),$$

which for $\mathrm{d}x\to 0$ gives

$$\theta'(x)=\frac{2\pi}{\Phi_0}\mu_0\lambda_L^2\frac{I_L(x)}{wd}, \tag{B4}$$

where $\mu_0\lambda_L^2$ is the specific kinetic inductance; see Appendix A.

By substituting Eq. (B3) into Eq. (B4) and solving it, we obtain

$$\theta(x)=\frac{2\pi}{\Phi_0}\frac{\mu_0\lambda_L^2}{wd}I\left(\frac{x}{2}-\frac{x^2}{2L}\right). \tag{B5}$$

For the moment we have omitted the integration constant as it will be added later when we consider and maximize the supercurrent.

The Josephson phase $\phi(x)$ is the difference of the phases $\theta_1(x)$ and $\theta_2(x)$ in electrodes 1 and 2. Since the electrode currents $I_{L1}(x)$ and $I_{L2}(x)$ flow in opposite directions, with accuracy of a constant one can write $\theta_2(x)=-\theta_1(x)$. Therefore, $\phi(x)=2\theta_1(x)$; see Eq. (B5). Following Ref. [40], we ignore the parabolic bending of the Josephson phase and keep only the linear term responsible for the global behavior, i.e.,

$$\phi(x)\approx\frac{2\pi}{\Phi_0}\frac{\mu_0\lambda_L^2}{wd}xI. \tag{B6}$$

This dependence is very similar to the linear Josephson phase created by an applied magnetic field B perpendicular to the film plane

$$\phi'(x)=\frac{2\pi}{\Phi_0}d_{\mathrm{eff}}B \quad\text{or}\quad \phi(x)=\frac{2\pi}{\Phi_0}d_{\mathrm{eff}}Bx=2\pi f\frac{x}{L}, \tag{B7}$$

where we have introduced the normalized flux $f\equiv\Phi/\Phi_0$, where $\Phi\equiv Bd_{\mathrm{eff}}L$ is the total magnetic flux threading the JJ. In our geometry, $d_{\mathrm{eff}}=2\lambda_L\tanh w/\lambda_L\approx 2w$. The linear Josephson phase in Eq. (B6) is proportional to the bias current I. In Ref. [40] this is called a "self-field effect." In our case the effect is exactly the same, but due to the kinetic nature of the electrode's inductance, the magnetic field induced by the bias current I as such is not present.

To obtain the total supercurrent, but now also including an applied magnetic field, we have to add the phase gradients resulting from both the bias current and the applied field. The ansatz reads

$$\phi(x)=2\pi(f+f_I i)\frac{x}{L}+\phi_0, \tag{B8}$$

where $i=I/I_{c0}$ is the normalized bias current and

$$f_I\equiv\frac{\mu_0\lambda_L^2\frac{L}{wd}I_{c0}}{\Phi_0}=\frac{L_K I_{c0}}{\Phi_0}=\frac{\Phi_{I_{c0}}}{\Phi_0} \tag{B9}$$

characterizes the strength of the "self-field" effect, i.e., the Josephson-phase gradient due to the bias current. It is defined as the pseudoflux $\Phi_{I_{c0}}$ through the kinetic inductance $L_k=\mu_0\lambda_L^2(L/wd)$ of the whole top electrode when one sends a current I_{c0} through it.

Following the standard procedure to find the total supercurrent

$$I_s(f,i,\phi_0)=d\int_{-L/2}^{+L/2} j_c\sin\phi(x)\,\mathrm{d}x,$$

with $\phi(x)$ given by Eq. (B8), and then maximization of $I_s(f,i,\phi_0)$ with respect to ϕ_0, we get for the normalized critical current $i_c=I_c/I_{c0}$

$$i_c(f,i_c)=\pm\frac{\sin[\pi(f+f_I i_c)]}{\pi(f+f_I i_c)}, \tag{B10}$$

where $I_{c0}\equiv j_c L d$ is the maximum possible critical current through the barrier at $f=f_I=0$. By using the definition (A1) of λ_J, one can rewrite the expression for f_I in a very simple and understandable form, namely,

$$f_I=\frac{1}{4\pi}\frac{L^2}{\lambda_J^2}. \tag{B11}$$

2. Optimum parameters

The final $i_c(f)$ dependence is given by the implicit expression (B10). For fixed values of f_I and f we solved this equation numerically to obtain $i_{c\pm}(f)$ plots for several different values of f_I (see Fig. 6). With increasing f_I, the $i_{c\pm}(f)$ plots depart from a symmetric Fraunhofer pattern ($f_I=0$ curve) and become skewed; however, they are still point-symmetric with respect to the origin. As f_I increases, the two critical currents $i_{c+}(f)$ and $i_{c-}(f)$ become rather different for $|f|$ somewhat below 1, thus giving high asymmetry. At $f_I>f_I^*=\pi/4\approx 0.785$, one of the $i_{c\pm}(f)$ curves

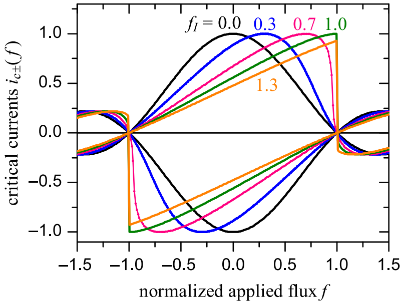

FIG. 6. Family of asymmetric $i_{c\pm}(f)$ curves for different values of f_I obtained by our solving Eq. (B10) numerically.

develops a discontinuous jump at $f = \pm 1$ from high i_c values to low ones.

To be more specific, in Fig. 7 we have plotted the dependence of the asymmetry $\mathcal{A}(f)$ for different values of f_I. There is an optimum applied field $f_{\rm opt}$, for which $\mathcal{A}$ has a maximum $\mathcal{A}_{\max} \equiv \mathcal{A}(f_{\rm opt})$. Moreover, $\mathcal{A}_{\max}$ and $f_{\rm opt}$ increase with increasing f_I monotonically, and for $f_I \geq f_I^*$ $\mathcal{A}(f)$ develops a jump at $f = 1$ related to the discontinuity of the $i_{c+}(f)$ branch.

Finally, to see which values of asymmetry can be reached in principle, we show $\mathcal{A}_{\max}(f_I)$ in Fig. 8(a). $\mathcal{A}_{\max}(f_I)$ rapidly increases with increasing f_I and formally diverges at f_I^*. The saturation value of $\mathcal{A}_{\max} \sim 600$ for $f_I \geq f_I^*$ is defined solely by numerical accuracy.

Thus, in the framework of the in-line JJ model introduced here, for optimum applied flux $f \approx 1$ and large enough in-line geometry parameter $f_I \geq f_I^*$, one can obtain almost unlimited asymmetry values.

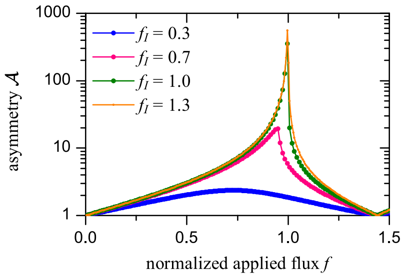

FIG. 7. Asymmetry parameter $\mathcal{A}(f)$ for different values of f_I obtained from the curves in Fig. 6 with the use of the definition (1).

3. Possible limitations

The model used above is an idealization. First, our initial assumption of a short JJ means that f_I defined by Eq. (B11) cannot be very large. However, we obtain very high $\mathcal{A}$ values already for $f_I = f_I^*$. This corresponds to $L = \pi\lambda_J$, which is still within the short limit. However, the numerical solution of the sine-Gordon equation to obtain $i_c(f, f_I)$ (not presented) shows that at $L \approx (3–5)\lambda_J$ the minimum critical current does not approach zero closely, so $\mathcal{A}_{\max}$ reaches values of about 5–6. Second, our approximation (linearization) of the Josephson phase in Eq. (B6) may be a reason for the extremely high $\mathcal{A}$ obtained. The huge values of $\mathcal{A}$ occur at $f_{\rm opt} \approx 1$ when one of the critical currents (almost) vanishes while the other one stays finite. However, when the bias current is small, the "self-field" term (both the linear one and the nonlinear one) plays no role for the branch with vanishing i_c. Instead, it may result in a certain small correction to the branch with

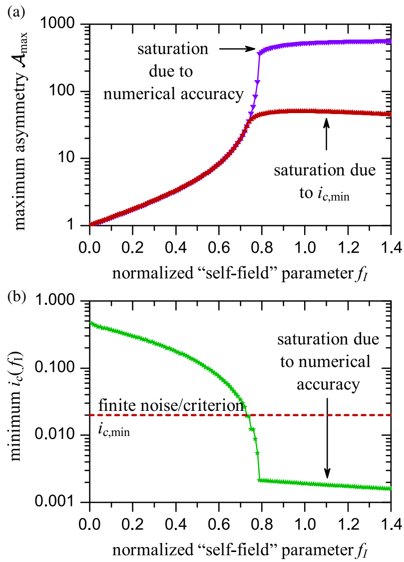

FIG. 8. (a) Maximum asymmetry parameter $\mathcal{A}_{\max}(f_I)$ taken at $f_{\rm opt}$ for each value of f_I. The violet curve is calculated according to the theoretical model. The bordeaux curve is calculated by our taking into account that $i_{c,\min}$ cannot become smaller than 0.02. (b) Minimum (by absolute value) critical current $i_{c,\min}$ at the optimum point $f_{\rm opt}$ as a function of f_I. The dashed line shows, as an example, the experimental limitation on $i_{c,\min}$, which was then used to calculate the bordeaux curve in (a).

high i_c. Altogether, high values of $\mathcal{A}$ weakly depend on the nonlinear term in Eq. (B5).

There are several experimental limitations that do not allow one to achieve very high values of $\mathcal{A}$ because it is very difficult experimentally to obtain vanishing $i_c(f)$ (one of the two) at $f_{\rm opt}$. In Fig. 8(b) we plot the smallest critical current $|i_{c,\min}(f_I)|$ taken at $f_{\rm opt}$. For $f_I \geq f_I{}^*$, $i_{c,\min}(f_I) \sim 0.002$, which again is defined by numerical accuracy. In experiments, for a number of reasons $i_{c,\min}$ cannot be so small. For example, nonuniformity in $j_c(x)$, typical for YBCO-based JJs, results in an $i_c(f)$ pattern where the minima are lifted relative to the $i = 0$ level. Another reason is that in experiments $I_c(B)$ is measured with some finite voltage criterion $V_{\rm cr}$ (typically 1–2 μV due to noise and limited resolution of the equipment), which results in a background I_c level $I_c^{\rm BG} \approx V_{\rm cr}R_n$, where R_n is the normal resistance of the JJ. If we assume that $i_{c,\min}(f_I)$ below 0.02 cannot be measured, then the maximum value of asymmetry $\mathcal{A}_{\max} \approx 1/0.02 = 50$ at best. In Fig. 8(b), as an example, we show this level by a dashed horizontal line. If the theoretical value $i_{c\pm}(f_I)$ becomes lower, we then use 0.02 for calculation of $\mathcal{A}_{\max}$. The result is shown in Fig. 8(a) (bordeaux curve). $\mathcal{A}_{\max}$ for $f_I \geq f_I{}^*$ is substantially reduced from infinity down to approximately 40.

APPENDIX C: QUASISTATIC STOCHASTIC DRIVE

In this appendix we demonstrate that one can rectify a noisy signal with zero average value and this does not violate any laws of thermodynamics if the spectrum of the noise is not white. We also study how the figures of merit change if one drives the diode stochastically rather than periodically. We start from the experimentally measured asymmetric IVC, and numerically calculate rectification of a random driving force $I(t) = \Xi(t)$ with a Gaussian distribution of the probability density

$$G(I,\sigma) = \frac{1}{\sqrt{2\pi}\sigma}\exp\left(-\frac{I^2}{2\sigma^2}\right). \qquad \text{(C1)}$$

Here the distribution width σ plays the role of the amplitude of the noise. If one has a realization of a random process $\Xi(t)$ with amplitude 1, the process $\sigma\,\Xi(t)$ has distribution width σ. We consider *quasistatic* noise, i.e., each random current value $\sigma\,\Xi(t_i)$ is applied and kept long enough to measure the voltage $V(\sigma\,\Xi(t_i))$ (IVC), then the next random current value $\sigma\,\Xi(t_{i+1})$ is applied, and so on. In other words, the bandwidth of this noise is much smaller than the typical Josephson frequencies and our measurement setup bandwidth. Then the average voltage $V_{\rm dc}$ is calculated. Note the difference between $V_{\rm dc}$ averaged over a long time and $\overline{V}$ averaged over one period. Because of quasistaticity, the result can be again obtained from the experimentally measured IVC numerically as

$$V_{\rm dc}(\sigma) = \lim_{T\to\infty}\frac{1}{T}\int_0^T V(\sigma\,\Xi(t) + I_{\rm dc})\,{\rm d}t = \lim_{N\to\infty}\frac{1}{N}\sum_{i=1}^{N} V(\sigma\,\Xi(t_i) + I_{\rm dc}). \qquad \text{(C2)}$$

Numerically, Eq. (C2) needs a long integration time to converge. However, for ergodic random processes this can be drastically simplified to a convolution of the Gaussian random distribution with the IVC:

$$V_{\rm dc}(\sigma) = \int_{-\infty}^{+\infty} G(I,\sigma)V(I + I_{\rm dc})\,{\rm d}I. \qquad \text{(C3)}$$

Note that the experimental $V(I)$ is available (measured) only in a certain limited current range. Therefore, to perform the integration in Eq. (C3), in practice we perform integration from -3σ to $+3\sigma$, thus cutting off the tails of the Gaussian distribution.

A set of rectification curves $V_{\rm dc}(\sigma)$ for different countercurrents $I_{\rm dc}$ is shown in Fig. 4(a). Qualitatively the curves look very similar to the $\overline{V}(I_{\rm ac})$ curves for a deterministic sinusoidal ac drive. However, the maximum rectified voltage in the idle regime became almost twice as small. The curves are also much smoother, which is understandable considering the Gaussian distribution of the noise. However, the stopping force does not change, which is easy to understand from the IVC. Namely, the applied countercurrent $I_{\rm dc}$ basically shifts the origin of the IVC so that the IVC becomes more symmetric. Roughly, the rectification vanishes when the positive and negative critical currents become equal, i.e., $I_{c+} - I_{\rm dc} \approx |-I_{c-} + I_{\rm dc}|$, regardless what kind of drive is applied.

Furthermore, a set of $\overline{P}_{\rm in}(\sigma)$, $\overline{P}_{\rm out}(\sigma)$, and $\eta(\sigma)$ curves for different values of $I_{\rm dc}$ is shown in Figs. 4(b)–4(d). One can see that the curves are similar to the ones with a sinusoidal drive. In particular, the efficiency $\eta(\sigma)$ for a heavy load still tends to the ultimate efficiency $\eta_{\rm ult}$.

Note that rectification of the quasistatic Gaussian noise does not contradict the second law of thermodynamics. Equilibrium thermal fluctuations produce a noise current with a Gaussian probability density and amplitude

$$\sigma = \sqrt{\frac{2k_BT\Delta f}{R}}, \qquad \text{(C4)}$$

where Δf is the bandwidth of the white noise. Quasistatic noise essentially means that $\Delta f \ll f_{\rm setup} \ll f_{\rm J}$. For example, for $\Delta f = 10$ kHz, according to Eq. (C4) the amplitude of the thermal noise $\sigma \sim 0.15$ nA, while we apply amplitudes at least 10^4 times larger (see Fig. 4). This essentially means that our noise is not thermal.

[1] Fuyuki Ando, Yuta Miyasaka, Tian Li, Jun Ishizuka, Tomonori Arakawa, Yoichi Shiota, Takahiro Moriyama, Youichi Yanase, and Teruo Ono, Observation of superconducting diode effect, Nature **584**, 373 (2020).

[2] Hideki Narita, Jun Ishizuka, Ryo Kawarazaki, Daisuke Kan, Yoichi Shiota, Takahiro Moriyama, Yuichi Shimakawa, Alexey V. Ognev, Alexander S. Samardak, Youichi Yanase, and Teruo Ono, Field-free superconducting diode effect in noncentrosymmetric superconductor/ferromagnet multilayers, Nat. Nanotechnol. **17**, 823 (2022).

[3] Yasen Hou, Fabrizio Nichele, Hang Chi, Alessandro Lodesani, Yingying Wu, Markus F. Ritter, Daniel Z. Haxell, Margarita Davydova, Stefan Ilić, Ourania Glezakou-Elbert, Amith Varambally, F. Sebastian Bergeret, Akashdeep Kamra, Liang Fu, Patrick A. Lee, and Jagadeesh S. Moodera, Ubiquitous superconducting diode effect in superconductor thin films, Phys. Rev. Lett. **131**, 027001 (2023).

[4] Alon Gutfreund, Hisakazu Matsuki, Vadim Plastovets, Avia Noah, Laura Gorzawski, Nofar Fridman, Guang Yang, Alexander Buzdin, Oded Millo, Jason W. A. Robinson, and Yonathan Anahory, Direct observation of a superconducting vortex diode, Nat. Commun. **14**, 1630 (2023).

[5] Heng Wu, Yaojia Wang, Yuanfeng Xu, Pranava K. Sivakumar, Chris Pasco, Ulderico Filippozzi, Stuart S. P. Parkin, Yu-Jia Zeng, Tyrel McQueen, and Mazhar N. Ali, The field-free Josephson diode in a van der Waals heterostructure, Nature **604**, 653 (2022).

[6] Kun-Rok Jeon, Jae-Keun Kim, Jiho Yoon, Jae-Chun Jeon, Hyeon Han, Audrey Cottet, Takis Kontos, and Stuart S. P. Parkin, Zero-field polarity-reversible Josephson supercurrent diodes enabled by a proximity-magnetized Pt barrier, Nat. Mater. **21**, 1008 (2022).

[7] Banabir Pal, Anirban Chakraborty, Pranava K. Sivakumar, Margarita Davydova, Ajesh K. Gopi, Avanindra K. Pandeya, Jonas A. Krieger, Yang Zhang, Mihir Date, Sailong Ju, Noah Yuan, Niels B. M. Schröter, Liang Fu, and Stuart S. P. Parkin, Josephson diode effect from Cooper pair momentum in a topological semimetal, Nat. Phys. **18**, 1228 (2022).

[8] Christian Baumgartner, Lorenz Fuchs, Andreas Costa, Simon Reinhardt, Sergei Gronin, Geoffrey C. Gardner, Tyler Lindemann, Michael J. Manfra, Paulo E. Faria Junior, Denis Kochan, Jaroslav Fabian, Nicola Paradiso, and Christoph Strunk, Supercurrent rectification and magnetochiral effects in symmetric Josephson junctions, Nat. Nanotechnol. **17**, 39 (2022).

[9] F. Paolucci, G. De Simoni, and F. Giazotto, A gate- and flux-controlled supercurrent diode effect, Appl. Phys. Lett. **122**, 042601 (2023).

[10] Sanat Ghosh, Vilas Patil, Amit Basu, Kuldeep, Achintya Dutta, Digambar A. Jangade, Ruta Kulkarni, A. Thamizhavel, Jacob F. Steiner, Felix von Oppen, and Mandar M. Deshmukh, High-temperature Josephson diode, Nat. Mater. **23**, 612 (2024).

[11] Pavel A. Volkov, Étienne Lantagne-Hurtubise, Tarun Tummuru, Stephan Plugge, J. H. Pixley, and Marcel Franz, Josephson diode effects in twisted nodal superconductors, Phys. Rev. B **109**, 094518 (2024).

[12] P. Reimann, Brownian motors: Noisy transport far from equilibrium, Phys. Rep. **361**, 57 (2002).

[13] Peter Hänggi and Fabio Marchesoni, Artificial Brownian motors: Controlling transport on the nanoscale, Rev. Mod. Phys. **81**, 387 (2009).

[14] H. Linke, Special issue on "Ratchets and Brownian motors: Basics, experiments, and applications", Appl. Phys. A **75**, 167 (2002).

[15] A. Th. A. M. de Waele and R. de Bruyn Ouboter, Quantum-interference phenomena in point contacts between two superconductors, Physica **41**, 225 (1969).

[16] I. Zapata, R. Bartussek, F. Sols, and P. Hänggi, Voltage rectification by a SQUID ratchet, Phys. Rev. Lett. **77**, 2292 (1996).

[17] S. Weiss, D. Koelle, J. Müller, R. Gross, and K. Barthel, Ratchet effect in dc SQUIDs, Europhys. Lett. **51**, 499 (2000).

[18] A. Sterck, S. Weiss, and D. Koelle, SQUID ratchets: Basics and experiments, Appl. Phys. A **75**, 253 (2002).

[19] A. Sterck, R. Kleiner, and D. Koelle, Three-junction SQUID rocking ratchet, Phys. Rev. Lett. **95**, 177006 (2005).

[20] A. Sterck, D. Koelle, and R. Kleiner, Rectification in a stochastically driven three-Junction SQUID rocking ratchet, Phys. Rev. Lett. **103**, 047001 (2009).

[21] G. Carapella and G. Costabile, Ratchet effect: Demonstration of a relativistic fluxon diode, Phys. Rev. Lett. **87**, 077002 (2001).

[22] M. Beck, E. Goldobin, M. Neuhaus, M. Siegel, R. Kleiner, and D. Koelle, High-efficiency deterministic Josephson vortex ratchet, Phys. Rev. Lett. **95**, 090603 (2005).

[23] H. B. Wang, B. Y. Zhu, C. Gürlich, M. Ruoff, S. Kim, T. Hatano, B. R. Zhao, Z. X. Zhao, E. Goldobin, D. Koelle, and R. Kleiner, Fast Josephson vortex ratchet made of intrinsic Josephson junctions in $Bi_2Sr_2CaCu_2O_8$, Phys. Rev. B **80**, 224507 (2009).

[24] M. Knufinke, K. Ilin, M. Siegel, D. Koelle, R. Kleiner, and E. Goldobin, Deterministic Josephson vortex ratchet with a load, Phys. Rev. E **85**, 011122 (2012).

[25] F. Falo, P. J. Martínez, J. J. Mazo, and S. Cilla, Ratchet potential for fluxons in Josephson-junction arrays, Europhys. Lett. **45**, 700 (1999).

[26] E. Trías, J. J. Mazo, F. Falo, and T. P. Orlando, Depinning of kinks in a Josephson-junction ratchet array, Phys. Rev. E **61**, 2257 (2000).

[27] F. Falo, P. J. Martínez, J. J. Mazo, T. P. Orlando, K. Segall, and E. Trías, Fluxon ratchet potentials in superconducting circuits, Appl. Phys. A **75**, 263 (2002).

[28] D. E. Shalóm and H. Pastoriza, Vortex motion rectification in Josephson junction arrays with a ratchet potential, Phys. Rev. Lett. **94**, 177001 (2005).

[29] V. M. Krasnov, V. A. Oboznov, and N. F. Pedersen, Fluxon dynamics in long Josephson junctions in the presence of a temperature gradient or spatial nonuniformity, Phys. Rev. B **55**, 14486 (1997).

[30] R. Menditto, H. Sickinger, M. Weides, H. Kohlstedt, D. Koelle, R. Kleiner, and E. Goldobin, Tunable φ Josephson junction ratchet, Phys. Rev. E **94**, 042202 (2016).

[31] E. Goldobin, R. Menditto, D. Koelle, and R. Kleiner, Model I–V curves and figures of merit of underdamped deterministic Josephson ratchets, Phys. Rev. E **94**, 032203 (2016).

[32] Taras Golod and Vladimir M. Krasnov, Demonstration of a superconducting diode-with-memory, operational at zero magnetic field with switchable nonreciprocity, Nat. Commun. **13**, 3658 (2022).
[33] We use a Zeiss Orion NanoFab He ion microscope with 30 keV He^+ ions.
[34] Shane A. Cybart, E. Y. Cho, T. J. Wong, Björn H. Wehlin, Meng K. Ma, Chuong Huynh, and R. C. Dynes, Nano Josephson superconducting tunnel junctions in $YBa_2Cu_3O_{7-\delta}$ directly patterned with a focused helium ion beam, Nat. Nanotechnol. **10**, 598 (2015).
[35] Ethan Y. Cho, Yuchao W. Zhou, Jennifer Y. Cho, and Shane A. Cybart, Superconducting nano Josephson junctions patterned with a focused helium ion beam, Appl. Phys. Lett. **113**, 022604 (2018).
[36] B. Müller, M. Karrer, F. Limberger, M. Becker, B. Schröppel, C. J. Burkhardt, R. Kleiner, E. Goldobin, and D. Koelle, Josephson junctions and SQUIDs created by focused helium-ion-beam irradiation of $YBa_2Cu_3O_7$, Phys. Rev. Appl. **11**, 044082 (2019).
[37] Ziwen Chen, Yulong Li, Rui Zhu, Jun Xu, Tiequan Xu, Dali Yin, Xinwei Cai, Yue Wang, Jianming Lu, Yan Zhang, and Ping Ma, High-temperature superconducting $YBa_2Cu_3O_{7-\delta}$ Josephson junction fabricated with a focused helium ion beam, Chin. Phys. Lett. **39**, 077402 (2022).
[38] M. Karrer, K. Wurster, J. Linek, M. Meichsner, R. Kleiner, E. Goldobin, and D. Koelle, Temporal evolution of electric transport properties of $YBa_2Cu_3O_{7-\delta}$ Josephson junctions produced by focused-helium-ion-beam irradiation, Phys. Rev. Appl. **21**, 014065 (2024).
[39] R. Hutt, C. Magén *et al.* (unpublished).
[40] A. Barone and G. Paternò, *Physics and Application of the Josephson Effect* (John Wiley and Sons, New York, 1982).
[41] C. Guarcello, S. Pagano, and G. Filatrella, Efficiency of diode effect in asymmetric inline long Josephson junctions, Appl. Phys. Lett. **124**, 162601 (2024).
[42] T. Golod, O. M. Kapran, and V. M. Krasnov, Planar superconductor-ferromagnet-superconductor Josephson junctions as scanning-probe sensors, Phys. Rev. Appl. **11**, 014062 (2019).
[43] R. Gerdemann, T. Bauch, O. M. Fröhlich, L. Alff, A. Beck, D. Koelle, and R. Gross, Asymmetric high temperature superconducting Josephson vortex-flow transistors with high current gain, Appl. Phys. Lett. **67**, 1010 (1995).
[44] T. Bauch, S. Weiss, H. Haensel, A. Marx, D. Koelle, and R. Gross, High-temperature superconducting Josephson vortex flow transistors: numerical simulations and experimental results, IEEE Trans. Appl. Supercond. **7**, 3605 (1997).
[45] V. G. Kogan, V. V. Dobrovitski, J. R. Clem, Yasunori Mawatari, and R. G. Mints, Josephson junction in a thin film, Phys. Rev. B **63**, 144501 (2001).
[46] The $I(t)$ waveform is generated by a programmable digital-to-analog converter card with an update rate of 10 kHz (samples per second).
[47] R. Bartussek, P. Hänggi, and J. G. Kissner, Periodically rocked thermal ratchets, Europhys. Lett. **28**, 459 (1994).
[48] Technically this is done by collection of 500 voltage samples with a sampling rate of 100 kHz by the programmable analog-to-digital converter card.
[49] According to the RSJ-like model [24] the linear rectification branch should start at I_{c+} and the maximum of the $\overline{V}(I_{ac})$ curve should appear exactly at I_{c+}. However, in Fig. 3(a) the $\overline{V}(I_{ac})$ curves seem to be shifted somewhat to the right relative to I_{c+} and I_{c-}. This is related to the rounding of our IVC near I_{c+} and I_{c-}, which is not captured by the model [24]. Namely, the value of the current I_{m+}, where the differential resistance reaches its maximum, is somewhat larger than I_{c+}. Similarly, $|I_{m-}| \gtrsim |I_{c-}|$. Thus, at $I_{ac} = I_{c+}$ we do have the onset of rectification; however, the voltage becomes substantial at $I_{ac} > I_{m+}$. Similarly, at $I_{ac} = |I_{c-}|$ the rectification curve starts bending down, but its maximum is reached at $|I_{m+}|$. In the RSJ-like IVC of the model [24], $I_{m\pm} = I_{c\pm}$.
[50] Formally, rectification occurs in an infinite range of $I_{ac} = I_{c+}$ to $I_{ac} = \infty$ where $\overline{V} > 0$. However, for $I_{ac} > |I_{c-}|$ the ratchet works in the so-called Sisyphus regime, where the particle moves in the asymmetric potential back and forth, dissipating a lot with a little net progress. Instead, for $I_{c+} < I_{ac} < |I_{c-}|$ the particle moves only in the easy (positive) direction and is blocked in the difficult (negative) direction.
[51] The data are available at https://doi.org/10.5281/zenodo.15806872.
[52] In a trilayer (strip-line) geometry, ℓ_J is known as the "inductance per square" of the superconducting (thin film) electrodes forming the JJ.

Publication 4

Reproduced with permission from
C. Schmid *et al.*, arXiv:2511.19197 (2025)

$YBa_2Cu_3O_7$ nano-constriction Josephson junctions and SQUIDs fabricated by focused helium-ion-beam irradiation

Christoph Schmid,[1] Christopher Buckreus,[1] David Haas,[1] Max Pröpper,[2] Robin Hutt,[1] César Magén,[3] Dominik Hanisch,[2] Max Karrer,[1] Meinhard Schilling,[2] Dieter Koelle,[1] Reinhold Kleiner,[1] and Edward Goldobin[1]

[1]*Physikalisches Institut, Center for Quantum Science (CQ) and LISA$^+$, Universität Tübingen, 72076 Tübingen, Germany*
[2]*Institut für Elektrische Messtechnik und Grundlagen der Elektrotechnik, Technische Universität Braunschweig, 38106 Braunschweig, Germany*
[3]*Instituto de Nanociencia y Materiales de Aragón (INMA), CSIC-Universidad de Zaragoza, 50009 Zaragoza, Spain*

(Dated: November 20, 2025 File: **He-FIB˙cJJs˙in˙YBCO˙v17.TEX**)

By focused 30 keV He ion beam irradiation, epitaxially grown $YBa_2Cu_3O_7$ (YBCO) thin films can be driven from the superconducting to the insulating state with increasing irradiation dose. A properly chosen dose suppresses superconductivity down to 4 K, while crystallinity is still preserved. With this approach we create areas of normal-conducting YBCO that can be used to define resistively shunted constriction-type Josephson junctions (cJJs) on the nanometer scale. We also demonstrate that the fabricated cJJs can be incorporated in direct current superconducting quantum interference devices and can be used as detector junctions in THz antennas.

Keywords: He-FIB, Josephson junction, constriction Josephson junction, nanowire, YBCO, YBCO resistors

I. INTRODUCTION

Constriction Josephson junctions (cJJs) – sometimes also denoted as superconducting nanowires or Dayem bridges – embody the paramount necessity when it comes to the down-scaling of Josephson devices below the 100 nm limit. JJs with a barrier usually have a moderate critical current density j_c such that upon down-scaling the junction width, the critical current I_c becomes suppressed by thermal fluctuations at temperatures $T \approx 4\,\mathrm{K}$, *i.e.* the Josephson energy $E_J = I_c\Phi_0/2\pi$ becomes comparable to or even less than $k_B T$; $\Phi_0 \approx 2.068\,\mathrm{fWb}$ is the magnetic flux quantum and k_B is the Boltzmann constant. For applications at higher temperatures, *e.g.*, using cuprate superconductors such as $YBa_2Cu_3O_7$ (YBCO), the problem is even more severe. Therefore, the best solution to increase $I_c \propto j_c$ is to use barrierless junctions, *i.e.*, cJJs. Another bonus of cJJs is that they are insensitive to moderate magnetic fields. Due to these advantages they were already successfully employed in conventional metallic superconductors like Al[1] and Nb[2–4]. This enabled the fabrication of superconducting quantum intereference nano-devices (nanoSQUIDs)[5,6] on chip[7], on lever[4,8] or on tip[9,10], or in photon-pressure devices[11,12] and qubits[13]. One of the most important parameters that define the operation of cJJs and the fabrication requirements is the superconducting coherence length ξ. cJJs with a constriction width $w \approx \xi$ show Josephson-like behavior with sinusoidal current-phase relation (CPR), but for larger w the behavior is inductance-like, with a linear CPR[14,15]. With that, the fabrication of cJJs in thin films made of Al ($\xi \approx 100\,\mathrm{nm}$)[16,17] or Nb ($\xi \approx 10 - 15\,\mathrm{nm}$)[18] is relatively easy or at least technologically feasible. However, for cuprate high-T_c superconductors with $\xi \approx 1\,\mathrm{nm}$ the fabrication of cJJs is rather challenging.

Many efforts on the fabrication of YBCO cJJs and nanowires were undertaken during the last decades. The first significant advancements in fabricating YBCO thin films with nanowires of approximately 200 nm in width and length were achieved using electron-beam lithography, metal stencils, and ion beam milling[19]. This fabrication technique dominated for decades and enabled the realization of some of the smallest superconducting structures[20–22], including nanowires as narrow as 50 nm. A major breakthrough came from the Chalmers group[23], which demonstrated reproducible YBCO nanowires with a width as small as 40 nm and a length of 50 nm. This achievement marked a new benchmark and led to a series of further investigations[24–28]. The same group successfully reduced the nanowire thickness as well, realizing grooved Dayem bridges[29]. More recently, encapsulating the YBCO thin film with protective layers turned out to be efficient against environmental and processing-induced degradation[30]. This provided 68 nm-wide nanowires with film thickness of only 5 nm. Another technically impressive method is the superlattice nanowire pattern transfer (SNAP) technique. It enabled the fabrication of microscaled nanowire arrays comprising 150 nanowires, each milled down to 15 nm wide and $\sim 30\,\mu\mathrm{m}$ long having $T_c \approx 20\,\mathrm{K}$)[31].

Focused ion beam (FIB) techniques have also proven to be highly effective for YBCO nanostructuring. Ga-FIB has been used to fabricate nanowires with widths of 55–120 nm[32–34], as well as to create variable-thickness bridges[35]. In the context of YBCO grain-boundary JJs[36], miniaturization down to widths of 80 nm has also been successfully demonstrated[37].

He-FIB irradiation represents a promising fabrication technique for modifying YBCO properties on the nanoscale without removing material by milling, but rather by local modification of the electric transport properties of the YBCO films[38]. One assumes, that the He ions induce mainly displacements of the loosely bounded chain-oxygens, reducting T_c of YBCO[39,40]. By irradiating along a line crossing a YBCO thin-film microbridge, typically 2–4 μm wide and 30–50 nm thick, using He-FIB one can fabricate a number of elements depending on the irradiation line-dose D_ℓ measured in the number of ions per nm of line length (ions/nm)[41–44]. For moderate line doses D_ℓ typically in the range roughly from 400 up to 1000 ions/nm, He-FIB irradiation induces a Josephson barrier. The critical current decreases with D_ℓ exponentially and becomes unmeasurable at 4.2 K for some $D_\ell > 1000$ ions/nm. In this range one obtains JJs with resistively-shunted junction (RSJ)-like I–V characteristics (IVCs)[41,42]. For high dose values $D_\ell \gtrsim 1500$ ions/nm one obtains highly resistive barriers with fully suppressed Josephson supercurrent at $T = 4.2$ K and above. Their resistance $R(T)$ increases strongly with decreasing T[42] reaching the MΩ range at 4.2 K. Scanning transmission electron microscopy (STEM) studies of such high dose barriers show that the crystal structure is destroyed (amorphized) within irradiated tracks. We denote such barriers as amorphous insulating barriers (AIBs)[42] and irradiation doses that are high enough to induce amorphization as overcritical doses. These AIBs have been used for lateral nanopatterning of YBCO thin film devices down to 50 nm linewidth[45]. Accordingly, AIBs can be used for defining the boundaries of electronic circuits and (SQUID) holes on the nanoscale. Various devices, with AIBs and JJs that were all written during one He-FIB run, have been demonstrated, *e.g.*, SQUIDs[42,45–47] or Josephson diodes[48].

An obvious approach to create ultra-narrow YBCO cJJs with widths down to only a few nm could rely on the use of AIBs. However, the lateral damage produced outside the He-FIB-induced amporphous tracks is significant on a length scale ~ 50 nm on both sides, see Appendix A for details. In this paper we present an alternative strategy to define ultra-narrow YBCO cJJs, approaching widths down to the FIB spot size of a few nm. Instead of narrow high-dose lines, we use He-FIB-induced resistive areas. The idea is to use doses that are equivalent to the moderate doses used for creating Josephson barriers, in the sense that amorphization is avoided. However, now the irradiated regions with suppressed superconductivity have an extension along current direction that is too large to allow for Cooper pair tunneling. This approach shall minimize lateral damage and hence bring the minimal width of a constriction roughly down to the He-FIB spot size.

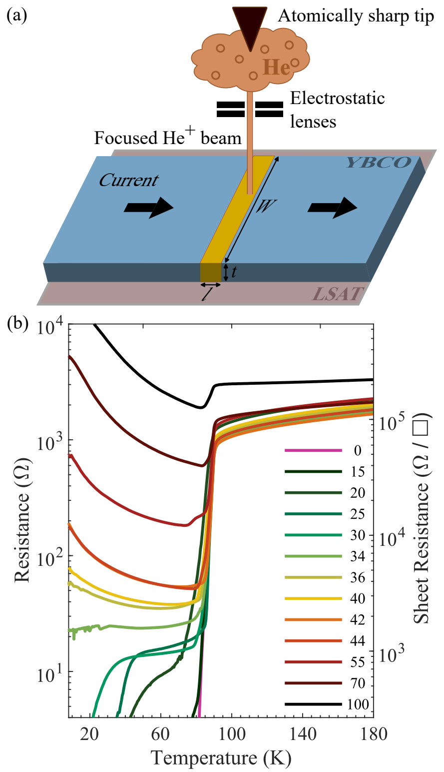

FIG. 1. (a) Sketch of an YBCO microbridge with He-FIB-irradiated area of length ℓ and width W. The YBCO film is $t = 30$ nm thick. (b) $R(T)$ curves of microbridges that contain areas ($\ell = 30$ nm, $W = 2\,\mu$m) irradiated with different areal doses D_a (color indicates D_a in ions/nm^2). R is measured at constant bias current $I = 1\,\mu$A. The right vertical axis shows RW/l, which below $T_{c,0}$ corresponds to the sheet resistance $R_\square$ of the irradiated region.

II. THIN FILM FABRICATION AND PREPATTERNING

c-axis oriented YBCO thin films with thickness $t = 30$ nm are epitaxially grown on a $10 \times 10\,\text{mm}^2$ $(LaAlO_3)_3(Sr_2AlTaO_6)_7$ (LSAT) substrate by pulsed laser deposition[49]. An ex-situ Ag (30 nm) plus Au (20 nm) capping layer is deposited and used for contact pads later on. Using optical lithography and Ar ion milling , the YBCO-Ag-Au trilayer is prepatterned into 144 microbridges, all 100 μm long and 2 μm wide connected on one side to a common ground and on the other to individual voltage and current pads. Then, using wet-etching process by means of TechniEtch ACI2 from MicroChemicals, the capping layer is removed in the areas to be irradiated by He-FIB and also between the contact pads to allow for 4-point transport measurements. In total, four of these chips were investigated.

III. RESISTIVE AREAS WRITTEN BY HE-FIB

For the investigation of the resistive areas, we irradiated a set of microbridges, each with a rectangular area across it, as shown in Fig. 1(a). For irradiation we used a He-FIB pixel spacing (pitch) $p = 1\,\mathrm{nm}$. We assume that the He-FIB has a Gaussian profile with a standard deviation $\sigma \approx 3\,\mathrm{nm}$, extracted from the STEM data in Ref.[42]. With that, the value for the pitch is a few times smaller than the estimated He-FIB spot-size 2σ. Each microbridge was irradiated with a different areal dose D_a ranging from 0 to $100\,\mathrm{ions/nm^2}$. The measured $R(T)$ curves of the microbridges are shown in Fig. 1(b). These curves demonstrate that He ion irradiation results in a superconductor-to-insulator transition as the dose increases, which confirms previous works[39,40,50]. For low dose values up to $30\,\mathrm{ions/nm^2}$, T_c decreases with increasing dose, shifting towards 8 K – our lowest measurement temperature for $R(T)$ measurements. At $D_\mathrm{a} \approx 34\,\mathrm{ions/nm^2}$ we do not observe a superconducting transition anymore and below $T_{c,0} \approx 89\,\mathrm{K}$ — the critical temperature of the unirradiated part of the YBCO microbridge — the resistance stays almost constant at $R \approx 22\,\Omega$. Assuming that below $T_{c,0}$ the resistance is entirely due to the irradiated region, we can estimate its sheet resistance as $R_\square = RW/\ell \approx 1.5\,\mathrm{k}\Omega/\square$, where the symbol $\square$ denotes a geometrical square area of thin film. With further increase of the dose, the resistance below $T_{c,0}$ increases and $R(T)$ becomes semiconductor-like reaching very high values at low T. Note that $R(D_a)$ curves at fixed $T < T_{c,0}$ show an exponential increase with D_a. This is probably compatible with Anderson localization and variable range hopping[51]. From our point of view, the most attractive dose for fabricaton of the resistors is around 35–40 $\mathrm{ions/nm^2}$. Here the values of the resistance are lowest and almost do not depend on T up to $T_{c,0}$. These YBCO resistors can also serve as circuit components, allowing straightforward integration into He-FIB–fabricated devices.

IV. CONSTRICTION JOSEPHSON JUNCTIONS

To define cJJs with a constriction width well below 100 nm we use He-FIB-induced YBCO resistors described in Sec. III. We create two triangular resistive areas with their tips almost touching each other, see the inset of Fig. 2(c). The distance between the tips defines the nominal constriction width w. For constrictions with $w \lesssim 30\,\mathrm{nm}$, the finite He-FIB spot size should be taken into account — the edges of the resistive areas are smeared on a scale $\sim \sigma$ of the He-FIB with a Gaussian cross-section profile. An effective areal dose $D_\mathrm{a,eff}(x, y)$ in each point can then be calculated as the convolution of the Gaussian beam profile with the pixel map defining the irradiation pattern. Figure 2(a) shows an example of a $D_\mathrm{a,eff}(x, y)$ profile, with Fig. 2(b) presenting the corresponding cross-sectional cut through the constriction.

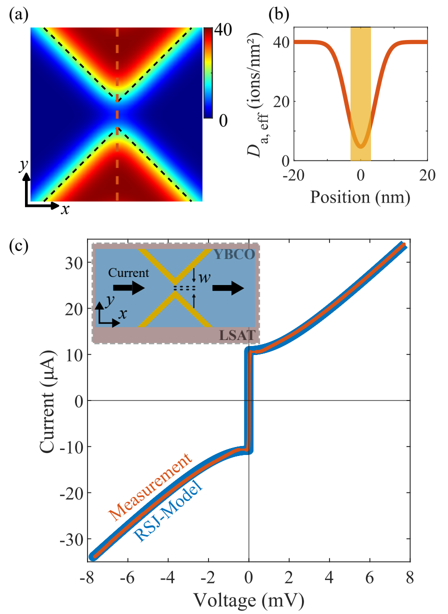

FIG. 2. YBCO cJJ: (a) Color plot $D_\mathrm{a,eff}(x, y)$ calculated for a constriction with $w = 6\,\mathrm{nm}$ and for a He-FIB with $\sigma = 3\,\mathrm{nm}$ in the $40 \times 40\,\mathrm{nm^2}$ region around the constriction. The dashed lines indicate the nominal edges of the irradiated areas (triangles) with the design distance $w = 6\,\mathrm{nm}$ between the tips. The $D_\mathrm{a,eff}(0, y)$ profile indicated by the orange dashed line is shown in (b). The yellow area indicates the cJJ width w. (c) The orange IVC describes a cJJ irradiated with $D_\mathrm{a} = 40\,\mathrm{ions/nm^2}$ and $w = 6\,\mathrm{nm}$, measured at $T = 4.2\,\mathrm{K}$. The blue IVC illustrates a RSJ-fit with a critical current $I_\mathrm{c} = 10.8\,\mu\mathrm{A}$ and a junction resistance $R_\mathrm{n} = 240\,\Omega$. The inset is a sketch of the bridge geometry, where the yellow regions indicate the He-FIB-irradiated resistive regions (100 nm wide) that define the banks of a cJJ with the nominal constriction width w.

Obviously, at the tips of the resistive areas the effective dose is somewhat lower than inside the resistive triangles. However, the dose inside the constriction is also non-vanishing as nominally assumed. Thus, the critical current density distribution $j_c(0, y)$ across the constriction may significantly deviate from a step-like profile, and we expect smearing of this profile on a length scale of several σ. Thus, the effective constriction width (defined as the region along the $(0, y)$) line where $T_c(y) > T$ can vary as a function of w and D_a and T and can even be made smaller than 2σ. Relying on the results presented in section III, we fabricated a set of cJJs using a dose of $D_\mathrm{a} = 40\,\mathrm{ions/nm^2}$ to create the resistive banks of cJJs. This dose is undercritical in terms of amorphization and

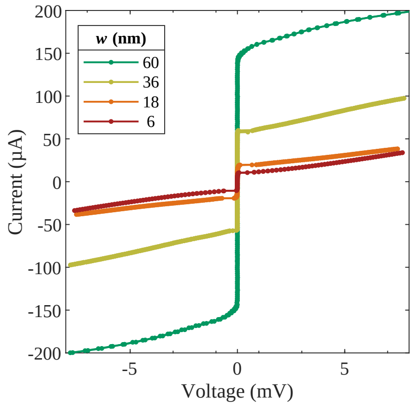

FIG. 3. IVCs (at $T = 4.2\,\mathrm{K}$) of YBCO cJJs with different constriction width w all irradiated with $D_\mathrm{a} = 40\,\mathrm{ions/nm^2}$.

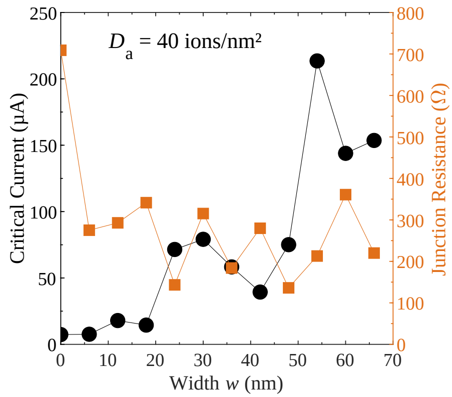

FIG. 4. Critical current $I_c(w)$ and junction resistance $R_\mathrm{n}(w)$ for YBCO cJJs irradiated with $D_\mathrm{a} = 40\,\mathrm{ions/nm^2}$, extracted from IVCs measured at $T = 4.2\,\mathrm{K}$.

provides an approximately constant resistivity over the whole temperature range from 5 K to $T_{\mathrm{c},0}$.

Using the geometry depicted in the inset of Fig. 2(c), we fabricated a series of cJJs with nominal constriction width w from 0 to 66 nm and characterized their electric transport properties at $T = 4.2\,\mathrm{K}$. Our best result in terms of downscaling is a cJJ with $w = 6\,\mathrm{nm}$ showing an RSJ-like IVC, see Fig. 2(c). IVCs of several other cJJs with different w are presented in Fig. 3. For increasing w the IVCs show a significant excess current I_ex and a linear, rather than RSJ-like hyperbolic branch above I_c, typical for superconductor-constriction-superconductor systems. To determine the junction resistance R_n, the slope of the IVC in the linear regime well above I_c is determined by fitting with $I = V/R_\mathrm{n} + I_\mathrm{ex}$ (not shown in the graph) and using R_n and I_ex as fitting parameters. At $w \gtrsim 48\,\mathrm{nm}$, the shape of the IVCs becomes flux-flow-like with a substantial rounding near I_c. The value of I_c was determined with a voltage criterion of $8\,\mu\mathrm{V}$.

In Fig. 4 we plot $I_c(w)$ and $R_\mathrm{n}(w)$ to summarize our findings. We observe a substantial spread in the cJJ parameters, similar to (or even larger than in) He-FIB barrier Josephson junctions[42,52]. While I_c shows an overall increase with increasing w, the resistance R_n stays more or less constant on the scale of the observed scattering. The reason for that is unknwon and under further investigation.

To test the high-frequency properties of the cJJs, in view of possible applications for YBCO voltage standards, we fabricated several cJJs in lithographically structured antennas. Under excitation with a far-infrared laser, we successfully observed Shapiro steps in the IVC. See Appendix B for details. We investigated IVCs at different T. The investigated cJJs demonstrate reliable operation over a wide temperature range and closely follow the theoretical model proposed by Bardeen[53]. For additional details, see Appendix C.

V. DC SQUID WITH TWO CONSTRICTION JUNCTIONS

Using the technique described above, we produced direct current (dc) nanoSQUIDs. Within a $2\,\mu\mathrm{m}$ wide microbridge, we centered a $100 \times 100\,\mathrm{nm^2}$ SQUID hole irradiated by He-FIB with a dose of $D_\mathrm{a} = 56\,\mathrm{ions/nm^2}$, to make sure that superconductivity is well suppressed. We used a pitch value of $p = 6\,\mathrm{nm}$, which results in $D_\mathrm{eff}(x, y)$ shown in Fig. 5(a). On two sides of the hole we created two cJJs as described in the previous section with $D_\mathrm{a} = 40\,\mathrm{ions/nm^2}$ (with finer $p = 1\,\mathrm{nm}$) and $w = 12\,\mathrm{nm}$. The cJJs are placed at a distance of $\approx 50\,\mathrm{nm}$ from the edge of the SQUID-hole to reduce the impact of mechanical stress (if any) on the constrictions. Figure 5(b) shows the circuit diagram of the SQUID, as outlined in more detail below. The IVC of the nanoSQUID, see Fig. 5(c), exhibits a maximum critical current of about $6.5\,\mu\mathrm{A}$ and $R_\mathrm{n} \approx 210\,\Omega$, at zero applied magnetic field perpendicular to the sample plane. The first minimum of $I_c(B)$ is obtained at $B = 10.6\,\mathrm{mT}$, where $I_c = 2.8\,\mu\mathrm{A}$. The IVC at this field is also shown in Fig. 5(c). The values of I_c are determined by using a 50 μV voltage criterion. The

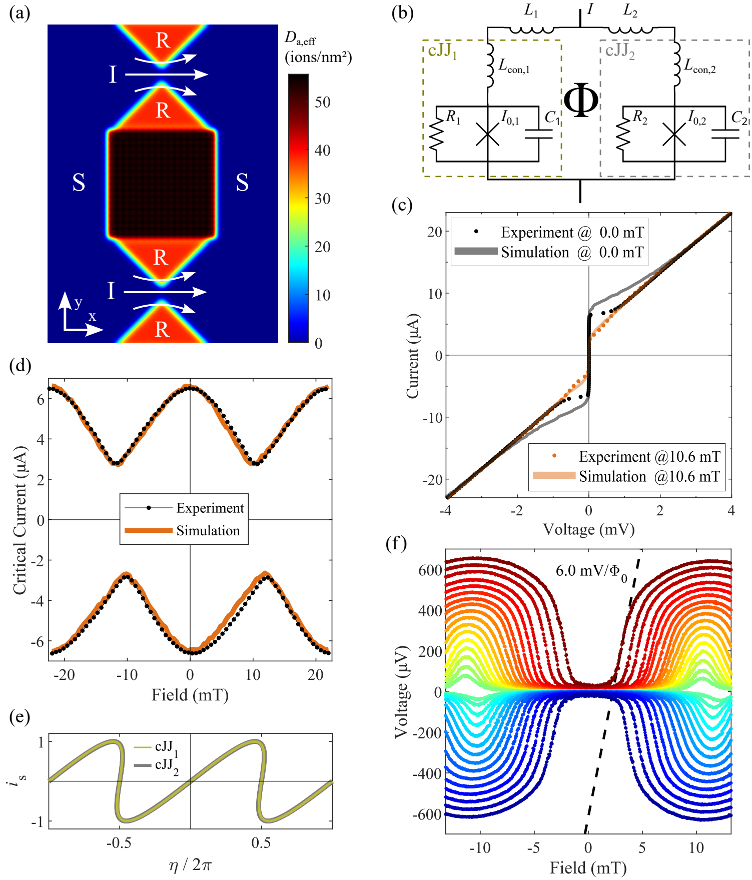

FIG. 5. YBCO dc SQUID with cJJs: (a) Calculated effective dose $D_{\mathrm{a,eff}}(x, y)$, assuming a Gaussian distribution of the He-FIB intensity with $\sigma = 3\,\mathrm{nm}$. (b) Circuit diagram of the dc SQUID used for simulations. (c) Experimental (dots) and simulated (lines) IVCs of the nanoSQUID at zero field (black) and at $B = 10.6\,\mathrm{mT}$ (orange). (d) Experimental (black) and simulated (orange) field modulation of positive and negative critical current. (e) Normalized current phase relations of the weak links, as extracted from simulations. (f) Voltage *vs.* applied magnetic field dependence at different bias currents through the nanoSQUID from $I = -6.33\,\mu\mathrm{A}$ (dark blue) to $I = 6.35\,\mu\mathrm{A}$ (dark red)). All measurements were performed at $T \approx 4.2\,\mathrm{K}$.

$I_c(B)$ modulation pattern, see Fig. 5(d), reveals an almost symmetric modulation with a modulation depth of $\Delta I_c/I_c \approx 58\%$.

From the period $\Delta B \approx 22.4\,\mathrm{mT}$ of the $I_c(B)$-modulation the effective area of the SQUID is estimated as $A_{\mathrm{eff}} \approx 9 \cdot 10^4\,\mathrm{nm}^2$, which is 6 times larger than the physical hole area $A_{\mathrm{hole}} = 1.5 \cdot 10^4\,\mathrm{nm}^2$, including the triangles forming the cJJ banks. This kind of flux focusing is typical for planar thin film structures. Numerical simulation of effective area[54] using 3D-MLSI[55] gives a 14 times larger area than A_{hole}. The origin of the discrepancy between measured and calculated flux focusing factor is currently not known. We have also measured $V(B)$ curves taken at different bias currents, see Fig. 5(f). The best transfer function of $6.0\,\mathrm{mV}/\Phi_0$ was obtained at $I = 6.35\,\mu\mathrm{A}$.

To compare our data with theoretical expectations and to exctract some unknown parameters we start from the circuit diagram in Fig. 5(b) and in essence solve the corresponding standard Langevin equations for the phase dynamics[56]. In the model each of the two SQUID arms contains a JJ with the noise free critical current $I_{0,1}$ (or $I_{0,2}$), which is shunted by a resistor R_1 (or R_2), which also generates a white noise according to the ambient temperature T and a capacitor C_1 (or C_2). The inductances of the SQUID arms are L_1 and L_2, respectively. In the standard model, the current-phase-relation of both JJs is assumed to be sinusoidal. In our case we expect that the CPR is skewed. Unfortunately, there is no unique expression describing the CPR's of all weak links microscopically. However, Likharev[14] proposed to model the constriction by a serial connection of an inductor $L_{\rm con}$ and an ideal JJ with sinusoidal CPR. We use this ansatz for our simulations. i.e. the SQUID dynamics can be described by the sinusoidal CPRs, but with an effective inductance of each SQUID arm $L_{\rm eff,1} = L_1 + L_{\rm con,1}$ and $L_{\rm eff,2} = L_2 + L_{\rm con,2}$. We then solve the dynamic Langevin equations for the Josephson phase differences ϕ_1 and ϕ_2 and calculate the dc voltages using the Josephson relation. We finally obtain the SQUID critical current by applying a proper voltage criterion. The simulations are performed in normalized units. We introduce the average JJ critical current $I_0 = (I_{0,1} + I_{0,2})/2$ and normalize other quantities using I_0. The parameters entering the model are the critical currents $I_{0,1}$ and $I_{0,2}$ *i.e.*, $i_{0,1}$ and $i_{0,2}$ in normalized units, the normalized SQUID inductance $\beta_L = 2I_0(L_1+L_2)/\Phi_0$, the noise parameter $\Gamma = 2\pi k_{\rm B}T/I_0\Phi_0$. Further, the normalized constriction inductances are $\beta^{\rm con}_{\rm L,1} = 2I_0L_{\rm con,1}/\Phi_0$ and $\beta^{\rm con}_{\rm L,2} = 2I_0L_{\rm con,2}/\Phi_0$ and the Stewart-McCumber parameter $\beta_C = 2\pi I_0R^2C/\Phi_0$, R is the average junction resistance and C is the average junction capacitance. As a result of fitting $I_c(B)$ we find $I_0 \approx 4.2\,\mu$A, resulting in $\Gamma = 0.043$. The SQUID inductance $L_1 + L_2$ is estimated using 3D-MLSI[55], resulting in a value of 23.6 pH and leading to $\beta_{\rm L} \approx 0.1$.

This value of $\beta_{\rm L}$ is much smaller than the effective dimensionless SQUID inductance $\beta^{\rm eff}_{\rm L} = \beta_{\rm L} + \beta^{\rm con}_{\rm L,1} + \beta^{\rm con}_{\rm L,2} \approx 0.9$ required for the best fit to the data. Thus, we conclude that the SQUID inductance is dominated by the constriction inductances. 3D-MLSI, solving the London equations, assumes a spatially constant Cooper pair density $n_{\rm s}$ and thus a spatially constant London penetration depth $\lambda_{\rm L}$. In the constriction regions $n_{\rm s}$ is likely to be reduced, and in addition microscopic processes like Andreev reflections may contribute to the distortion of the CPRs, leading to large values of $L_{\rm con,1}$ and $L_{\rm con,2}$. Further, for the best fit we used $i_{0,1} = I_{0,1}/I_0 = 1.1$ and $i_{0,2} = I_{0,2}/I_0 = 0.9$. The normalized constriction inductances were $\beta^{\rm con}_{\rm L,1} = 0.364$ and $\beta^{\rm con}_{\rm L,2} = 0.454$. For simplicity we assumed that the junction resistances are inversely proportional to $i_{0,1}$ and $i_{0,2}$, *i.e.*, we kept the product of the junction resistances and critical currents constant. We further assumed equal junction capacitances and used a Stewart-McCumber parameter $\beta_C = 0.2$.

Figure 5(c) shows (solid lines) the resulting simulated IVCs for both maximum and minimum critical current. The experimental curve for minimum critical current is reproduced well, while there are deviations for the IVC at maximum critical current. An increase of β_C to values around 1 would have caused a better agreement with this curve, however, would lead to a strong LC resonance visible as a bump in the IVC for $B = 10.6$ mT crossing the zero-field IVC in some voltage range, which is not observed. Thus, we rule out large values of β_C by means of pure fitting and also note that such a scenario would not match our weak-link geometry, where we expect at best very small stray capacitances. We assume that the significant deviations of the zero-field IVC arise from Joule heating or other nonequilibrium effects causing a suppression of the superfluid density in the weak link region. Finally, a comparison of the high-voltage regime of the experimental and simulated IVCs yields a characteristic voltage I_0R of about 1.5 mV, resulting in a dimensionless voltage criterion of 0.033, which was used for simulation of $I_c(B)$. Fig. 5(d) shows the simulated $I_c(B)$ patterns by the orange lines, both for positive and negative polarities. For the comparison the experimental data needed to be shifted slightly by 0.02 Φ_0 on the flux axis to account for residual magnetic fields in the setup. The agreement between the experimental curves and the simulated ones is good. Note that the data for negative currents are reproduced less well. This is, because the experimental curves are not exactly point symmetric while the simulated ones are. The fits have been made for postitive currents. Overall, the essential parameters for the $I_c(B)$ patterns (junction asymmetries and constriction inductances) leave very little degrees of freedom, only a few percent. In Fig. 5(e), we show the resulting skewed CPR, resulting from Likharev's ansatz, leading to the implicit expression.

$$I_k = I_{0,k}\sin\left(\eta_k - \frac{2\pi}{\Phi_0}L_{{\rm con},k}I_k\right), \text{ where } k = 1,2, \quad (1)$$

where I_k are the currents through the cJJs. The phases η_k are the sum of the phase drops across the constriction inductances and the ideal junctions, and the argument of the sine function yields the phase across the ideal JJ. In dimensionless units

$$i_k = \sin\left(\eta_k - \pi\beta^{\rm con}_{{\rm L},k}i_{0,k}i_k\right) = \sin\left(\eta_k - \pi l^{\rm con}_k i_k\right), \quad (2)$$

where $i_k = I_k/I_{0,k}$ is the bias current normalized to the critical current of *each* JJ and $l^{\rm con}_k = 2L_{{\rm con},k}I_{0,k}/\Phi_0$ are normilized inductances.

If, in Eq. (2), the parameter $\pi l^{\rm con}_k \equiv \pi\beta^{\rm con}_{{\rm L},k}i_{0,k} > 1$, then the CPR becomes multivalued. In our case we have $\pi l^{\rm con}_1 = \pi\cdot 0.364\cdot 1.1 \approx 1.26$ and $\pi l^{\rm con}_2 \approx \pi\cdot 0.454\cdot 0.9 \approx 1.28$ for both JJs. The corresponding normalized CPRs are plotted in Fig. 5(e), which are nearly identical.

VI. CONCLUSIONS

Using resistive areas created in a YBCO thin film by He-FIB irradiation, we fabricated cJJs with the nominal constriction size as small as $w = 6\,\mathrm{nm}$ and demonstrated its operation. For smallest w we observed an RSJ-like IVC with critical current $\sim 10\,\mu\mathrm{A}$ and characteristic voltage $V_c \approx 2.4\,\mathrm{mV}$ and no excess current at 4.2 K. For larger w excess current appears and dominates for $w > 20\,\mathrm{nm}$. Flux-flow like IVCs are observed for $w \approx 50\,\mathrm{nm}$ and above. $I_c(T)$ dependences demonstrate that cJJs can be used at temperatures up to 50–70 K. However, for this the constriction cannot be too small and the IVCs are not RSJ-like.

Further, we demonstrated the realization of a dc nanoSQUID, where both the two cJJs and the SQUID hole are written by He-FIB irradiation within a $2\,\mu\mathrm{m}$ wide YBCO microbridge. The SQUID shows a $I_c(B)$ modulation with the depth 58%, which can be explained by an additional constriction inductance. The $V(B)$ curves demonstrate a transfer function up to $6\,\mathrm{mV}/\Phi_0$. The size of the SQUID is defined by the microbridge width and can be further reduced.

ACKNOWLEDGMENTS

This work was funded by the Deutsche Forschungsgemeischaft (DFG) via project No. GO-1106/6 and GO-1106/7 and by the European Commission under H2020 FET Open grant "FIBsuperProbes" (Grant No. 892427). We also gratefully acknowledge support by the COST actions NANOCOHYBRI (CA16218), FIT4NANO (CA19140) and SUPERQUMAP (CA21144). We thank M. Turad and R. Löffler for invaluable help with "Orion Nanofab". The authors acknowledge the use of instrumentation as well as the technical advice provided by the National Facility ELECMI ICTS, at the node Laboratorio de Microscopias Avanzadas (LMA) of the Universidad de Zaragoza.

Appendix A: cJJs created by AIBs

Our first effort to make cJJs is illustrated in the inset of Fig. 6. An AIB with $D = 3000\,\mathrm{ions/nm}$ was drawn by He-FIB almost across the whole microbridge, except for a constriction of width $w = 1000, 500 \ldots, 50\,\mathrm{nm}$. Then, the critical current of each cJJ was measured and plotted as a function of w, see Fig. 6. $I_c(w)$, as expected, decreases linearly with w. However, the cJJs with $w < 100\,\mathrm{nm}$ (no data points shown) not only showed no critical current but had very high resistance, which is an indication of transport interruption through the constriction. To make sure that this is not caused by accidentally broken cJJs, we also made a linear fit of $I_c(w)$ data using the function

$$I_c(w) = J_c(w - w_0), \quad \text{(A1)}$$

see Fig. 6, where J_c is the critical current per junction width. The fit shows that the linear dependence does not arrive at the origin, but is shifted by $w_0 \approx 100\,\mathrm{nm}$. Thus, for all measured cJJs the effective width $w - w_0$ is systematically smaller then the design width w.

High-angle annular dark field (HAADF) STEM anal-

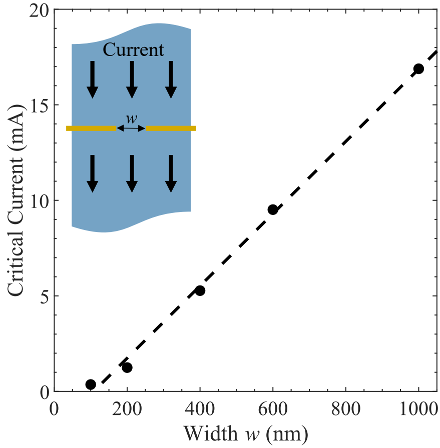

FIG. 6. Experimentally measured $I_c(w)$ of cJJs fabricated with He-FIB-induced AIBs with $D = 3000\,\mathrm{ions/nm}$ (dots). The dashed line shows a fit by the linear function $I_c(w) = J_c \cdot (w - w_0)$, which gives $J_c = 20\,\mu\mathrm{A/nm}$ and $w_0 = 108\,\mathrm{nm}$. The inset depicts the cJJs geometry formed by AIBs (horizontal yellow lines).

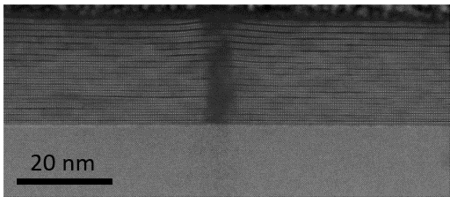

FIG. 7. Cross-sectional HAADF-STEM image of a YBCO lamella cut across (perpendicular to) the single line irradiated by He-FIB with a dose $D = 2000\,\mathrm{ions/nm}$. The bottom layer is LSAT, the middle layer is YBCO and the top layer is a Pt-C deposit grown by focused electron beam induced deposition to protect the YBCO film during TEM lamella preparation. In the YBCO layer one sees atomic planes, while the dark vertical column in the center corresponds to the amorphized YBCO.

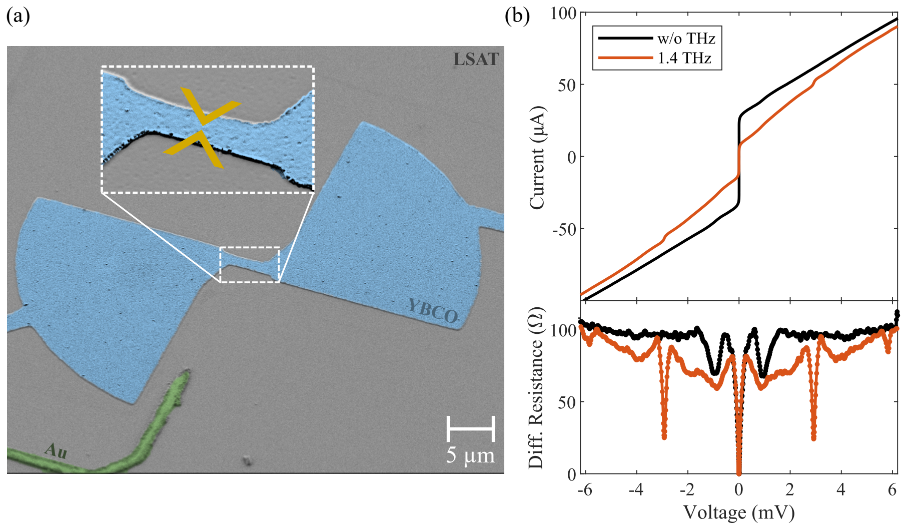

FIG. 8. (a) False-colored scanning electron microscopy image of the bow-tie antenna. The antenna has a 2 μm wide microbridge at the center, which is depicted in the inset. The yellow triangles indicate the He-FIB irradiation pattern which is used to create the 8 nm wide cJJ. The thin Au covered trace entering from the bottom left edge of the picture is used as a sacrificial structure for the He-FIB. (b) IVC and $R_{\mathrm{d}}(V)$ of the cJJ embedded into the antenna structure at $T = 20\,\mathrm{K}$. Black curves are measured without and orange curves with 1.4 THz excitation.

ysis of AIBs, illustrated in Fig. 7, was performed in a Thermo Fisher Scientific probe-corrected Titan 60-300, equipped with a CETCOR aberration corrector for the condenser systems, with a STEM probe size smaller than 1 Å. The cross sectional lamella specimen was prepared in a Thermo Fisher Scientific Helios 650 Dual Beam. The atomic resolution image evidences the bending STEM analysis of AIBs, see Fig. 7, showing a bending of YBCO atomic planes near amorphized region towards the surface of the sample. Obviously, in the amorphized region the YBCO atoms are not optimally packed. This, probably, leads to a mechanical pressure onto the neighboring still crystalline regions of YBCO, which results in the upbending. Visually, the bending takes place in an approximately 50 nm wide lateral vicinity on both sides of the AIB, which suggests that superconductivity is suppressed in this region. Sometimes one also observes cracks (not shown). Thus, AIBs are not suitable for the fabrication of nano-cJJs or any other nanostructures with lateral sizes $\lesssim 100\,\mathrm{nm}$.

Appendix B: cJJ under THz-Irradiation

The cJJs presented in section IV have rather high characteristic voltages $V_c > 2.5\,\mathrm{mV}$, making them attractive for THz applications such as voltage standards or detectors[44,57,58]. Here we demonstrate the appearance of Shapiro steps under irradiation in the THz range.

To perform this experiment, we have used a YBCO film with a microstructured bow-tie antenna, see Fig. 8(a). Then, using the procedure described above, we have patterned a cJJ with $w = 8\,\mathrm{nm}$ at the feed point of the antenna. We used $D_{\mathrm{c}} = 40\,\mathrm{ions/nm^2}$ and $p = 1\,\mathrm{nm}$ to draw the constriction banks. At $T = 20\,\mathrm{K}$ we obtained $I_{\mathrm{c}} = 28\,\mu\mathrm{A}$ and normal resistance of $R_{\mathrm{n}} \approx 100\,\Omega$, see Fig. 8(b).

The cJJ is investigated then as a THz detector, which operates in the frequency range of the far-infrared laser FIRL-100 from Edinburgh Instruments. In our particular case[59,60] the available laser emits simulataneosly at the frequencies of 1, 1.3 and 1.4 THz. By adjusting the position of the cJJ relative to the laser beam, one can choose the dominating frequency, which couples into the THz antenna. Under laser irradiation the IVC of the cJJ exhibits a smaller critical current and reveals a small Shapiro step at 2.9 mV, see Fig. 8(b). This exactly corresponds to the 1.4 THz mode of the laser. Calculating the differential resistance $R_d(V)$ from the IVC and comparing the peaks of the $R_d(V)$ obtained with and without irradiation allows us to observe even the second Shapiro step, which is hardly visible in the IVC. The appearance

$I_{c,0}$ (μA)	T_c (K)	$j_{c,0}$ (MA/cm^2)	A (nm^2)	w (nm)	D_a (ions/nm^2)	cJJ
5	37	3	180	6	47	A2
7	33	2	480	16	40	A12
14	42	8	180	6	47	A1
17	51	9	180	6	40	A4
31	48	17	180	6	40	A3
33	58	14	240	8	40	A5
34	52	10	360	12	47	A8
84	59	35	240	8	40	A6
150	72	31	480	16	40	A11
224	74	62	360	12	40	A10
275	68	76	360	12	47	A7
291	74	81	360	12	40	A9

TABLE I. Parameters of different YBCO cJJs listed in the order of the increasing fitting parameter $I_{c,0}$. Here, $I_{c,0}$ denotes the depairing current at $T = 0\,$K and T_c the critical temperature – both obtained from the best fit of the data using equation (C1). The current density $j_{c,0}$ is calculated with $I_{c,0}$ and the cross-section A of the cJJ. D_a and w are the fabrication parameters.

of Shapiro steps indicates that high-frequency radiation can be effectively coupled to cJJs and that these junctions display real Josephson (nonlinear) behavior, rather than merely acting as linear inductors.

Appendix C: Critical current *vs.* temperature

We have measured the $I_c(T)$ dependences for a set of cJJs embedded in the feed point of various microwave antennas, see Fig. 8 as an example. An overview of the fabrication parameters such as areal dose D_a and constriction width w, is presented in Tab. I. The $I_c(T)$ data, extracted from single IVCs at different temperatures with a voltage criterion of $50\,\mu$V are presented in Fig. 9. Note that values of $I_c < 0.3\,\mu$A are not reliable due to the thermal noise at $T = 4.2\,$K. Therefore we adopted the cut-off criterion $I_{cutoff}(T) = 0.3\,\mu\text{A} \cdot T\,/\,4.2\,\text{K}$ and disregarded all points having $I_c(T) < I_{cutoff}(T)$, see Fig 9(a). After such preprocessing, we tried to fit the data with the Bardeen equation[53]. This approach, which describes the temperature dependence of the depairing current of a superconductor in the dirty limit was already used in several reports on cJJs[3,61]. In short, the critical depairing current

$$I_c(T) = \frac{B_c(T)}{\mu_0\,\lambda_L(T)} \approx I_{c,0}\left[1 - \left(\frac{T}{T_c}\right)^2\right]^{\frac{3}{2}}, \qquad \text{(C1)}$$

where $I_{c,0}$ is the depairing current at $T = 0\,$K, T_c is the critical temperature. The expression (C1) uses well known empirical dependencies for the bulk critical field $B_c(T) = B_0\,(1 - (T/T_c)^2)$ and the London penetration depth $\lambda_L = \lambda_0\,/\,\sqrt{(1 - (T/T_c)^4)}$. Finer details like d-wave order parameter symmetry in YBCO are ignored for now.

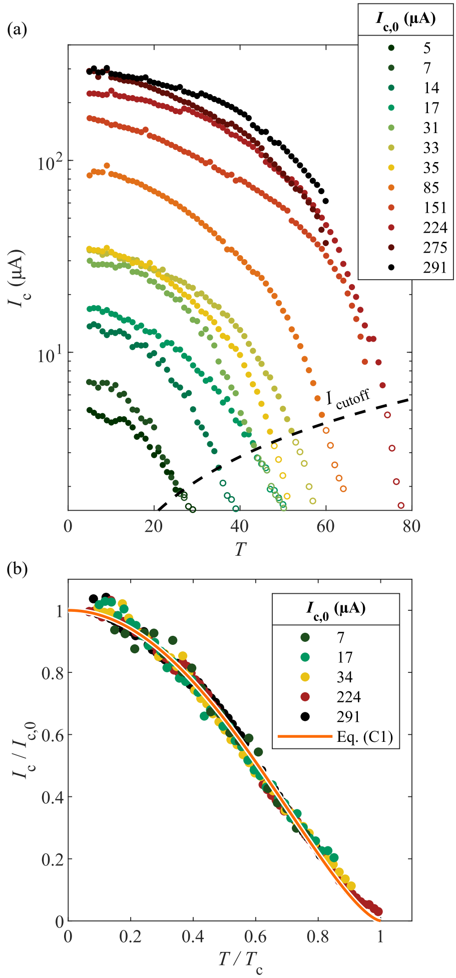

FIG. 9. (a) Experimentally measured $I_c(T)$ dependencies of the devices from Tab. I. The cut-off criterion $I_{cutoff}(T)$ (dashed line) defines the fitting range for Eq. (C1). The corresponding best-fit parameters for the considered data points (dots) are summarized in Tab. I, while the omitted data are marked by circles. The legend shows the depairing currents $I_{c,0}$. (b) A subset of the data from (a), showing the normalized critical current $I_c/I_{c,0}$ versus the normalized temperature T/T_c. The normalization factors $I_{c,0}$ and T_c corresponds to the best-fit values and are listed in Tab. I. Eq. (C1) is represented by the continuous orange line.

We used Eq. (C1) to fit our data with $I_{c,0}$ and T_c as fitting parameters. The fit boundaries for T_c were set as T_c = 30–87 K. A representive subset of devices compared with the fitting model is shown in Fig. 9(b). For lower critical currents, the noise contribution impacts huge parts of the acquired data. Truncating the data by applying the cut-off criteria for the critical current, the fitting procedure is limited to a narrow range of critical currents, limiting its validity. For higher critical currents the cut-off criteria barely shrinks the data. Nevertheless, the Bardeen model accurately captures the temperature dependence of the critical current over a broad temperature range.

We point out, that the nominal width of the patterned cJJs may not necessarily represent the effective width of the device. Due to possible fluctuations of the beam intensity and quality in addition to inhomogeinity in the film quality, we get I_c values which do not scale with the change in width and dose, cf Tab. I.

The depairing current density $j_{c,0}$ can exceed[24,62] 100 MA/cm^2. As shown in Tab. I, the $j_{c,0}$ values exhibit a considerable spread with the highest one being 81 MA/cm^2. The much lower values of $j_{c,0}$ may be due to an effective junction cross-section, which is lower than the nominal one. Alternatively, the smaller bridges may show some degradation which may lead to a suppression of the order parameter, and thus an increased value of λ_L and a reduced value of B_c.

In conclusion, the $I_c(T)$ behaviour is well described by the Bardeen expression (C1) for the depairing current vs T. For higher $I_{c,0}$ values, the devices can be used in applications at 50–70 K.

[1] R. Vijay, E. M. Levenson-Falk, D. H. Slichter, and I. Siddiqi, Approaching ideal weak link behavior with three dimensional aluminum nanobridges, Appl. Phys. Lett. **96**, 223112 (2010).

[2] O. Kennedy, J. Burnett, J. Fenton, N. Constantino, P. Warburton, J. Morton, and E. Dupont-Ferrier, Tunable Nb superconducting resonator based on a constriction nano-SQUID fabricated with a Ne focused ion beam, Phys. Rev. Appl. **11**, 014006 (2019).

[3] K. Uhl, D. Hackenbeck, J. Peter, R. Kleiner, D. Koelle, and D. Bothner, Niobium quantum interference microwave circuits with monolithic three-dimensional nanobridge junctions, Phys. Rev. Appl. **21**, 024051 (2024).

[4] T. Weber, D. Jetter, J. Ullmann, S. A. Koch, S. F. Pfander, K. Kress, A. Vervelaki, B. Gross, O. Kieler, U. Drechsler, P. R. Baral, A. Magrez, R. Kleiner, A. W. Knoll, M. Poggio, and D. Koelle, Advanced SQUID-on-lever scanning probe for high-sensitivity magnetic microscopy with sub-100-nm spatial resolution, Phys. Rev. Appl **24**, 054041 (2025).

[5] C. Granata and A. Vettoliere, Nano Superconducting Quantum Interference device: A powerful tool for nanoscale investigations, Phys. Rep. **614**, 1 (2016).

[6] M. J. Martínez-Pérez and D. Koelle, NanoSQUDs: Basics & recent advances, Phys. Sci. Rev. **2**, 20175001 (2017).

[7] S. K. H. Lam and D. L. Tilbrook, Development of a niobium nanosuperconducting quantum interference device for the detection of small spin populations, Appl. Phys. Lett. **82**, 1078 (2003).

[8] M. Wyss, K. Bagani, D. Jetter, E. Marchiori, A. Vervelaki, B. Gross, J. Ridderbos, S. Gliga, C. Schönenberger, and M. Poggio, Magnetic, Thermal, and Topographic Imaging with a Nanometer-Scale SQUID-On-Lever Scanning Probe, Phys. Rev. Appl. **17**, 034002 (2022).

[9] D. Vasyukov, Y. Anahory, L. Embon, D. Halbertal, J. Cuppens, L. Neeman, A. Finkler, Y. Segev, Y. Myasoedov, M. L. Rappaport, M. E. Huber, and E. Zeldov, A scanning superconducting quantum interference device with single electron spin sensitivity, Nat. Nanotechnol. **8**, 639 (2013).

[10] Y. Anahory, H. R. Naren, E. O. Lachman, S. B. Sinai, A. Uri, L. Embon, E. Yaakobi, Y. Myasoedov, M. E. Huber, R. Klajn, and E. Zeldov, SQUID-on-tip with single-electron spin sensitivity for high-field and ultra-low temperature nanomagnetic imaging, Nanoscale **12**, 3174 (2020).

[11] D. Bothner, I. C. Rodrigues, and G. A. Steele, Photon-pressure strong coupling between two superconducting circuits, Nat. Phys. **17**, 85 (2021).

[12] I. C. Rodrigues, D. Bothner, and G. A. Steele, Cooling photon-pressure circuits into the quantum regime, Sci. Adv. **7**, eabg6653 (2021).

[13] D. Rieger, S. Günzler, M. Spiecker, P. Paluch, P. Winkel, L. Hahn, J. K. Hohmann, A. Bacher, W. Wernsdorfer, and I. M. Pop, Granular aluminium nanojunction fluxonium qubit, Nat. Mater. **22**, 194 (2023).

[14] K. K. Likharev, Superconducting weak links, Rev. Mod. Phys. **51**, 101 (1979).

[15] A. A. Golubov, M. Yu. Kupriyanov, and E. Il'ichev, The current-phase relation in Josephson junctions, Rev. Mod. Phys. **76**, 411 (2004).

[16] W. M. J. Van Weerdenburg, A. Kamlapure, E. H. Fyhn, X. Huang, N. P. E. Van Mullekom, M. Steinbrecher, P. Krogstrup, J. Linder, and A. A. Khajetoorians, Extreme enhancement of superconductivity in epitaxial aluminum near the monolayer limit, Sci. Adv. **9**, eadf5500 (2023).

[17] D. López-Núñez, A. Torras-Coloma, Q. Portell-Montserrat, E. Bertoldo, L. Cozzolino, G. A. Ummarino, A. Zaccone, G. Rius, M. Martinez, and P. Forn-Díaz, Superconducting penetration depth of Aluminum thin films, Supercond. Sci. Technol. **38**, 095004 (2025).

[18] N. Pinto, S. J. Rezvani, A. Perali, L. Flammia, M. V. Milošević, M. Fretto, C. Cassiago, and N. De Leo, Dimensional crossover and incipient quantum size effects in superconducting niobium nanofilms, Sci. Rep. **8**, 4710 (2018).

[19] J. Schneider, H. Kohlstedt, and R. Wördenweber, Nanobridges of optimized $YBa_2Cu_3O_7$ thin films for superconducting flux-flow type devices, Appl. Phys. Lett. **63**, 2426 (1993).

[20] G. Papari, F. Carillo, D. Stornaiuolo, L. Longobardi, F. Beltram, and F. Tafuri, High critical current den-

sity and scaling of phase-slip processes in YBaCuO nanowires, Supercond. Sci. Technol. **25**, 035011 (2012).

[21] P. Larsson, B. Nilsson, and Z. G. Ivanov, Fabrication and transport measurements of $YBa_2Cu_3O_{7-x}$ nanostructures, J. Vac. Sci. Technol. B **18**, 25 (2000).

[22] F. Tafuri, D. Massarotti, L. Galletti, D. Stornaiuolo, D. Montemurro, L. Longobardi, P. Lucignano, G. Rotoli, G. P. Pepe, A. Tagliacozzo, and F. Lombardi, Recent Achievements on the Physics of High-T_C Superconductor Josephson Junctions: Background, Perspectives and Inspiration, J. Supercond. Nov. Magn. **26**, 21 (2013).

[23] S. Nawaz, R. Arpaia, T. Bauch, and F. Lombardi, Approaching the theoretical depairing current in $YBa_2Cu_3O_{7-x}$ nanowires, Physica C **495**, 33 (2013).

[24] R. Arpaia, S. Nawaz, F. Lombardi, and T. Bauch, Improved nanopatterning for YBCO nanowires approaching the depairing current, IEEE Trans. Appl. Supercond. **23**, 1101505 (2013).

[25] R. Arpaia, M. Arzeo, R. Baghdadi, E. Trabaldo, F. Lombardi, and T. Bauch, Improved noise performance of ultrathin YBCO Dayem bridge nanoSQUIDs, Supercond. Sci. Technol. **30**, 014008 (2016).

[26] R. Arpaia, D. Golubev, R. Baghdadi, R. Ciancio, G. Dražić, P. Orgiani, D. Montemurro, T. Bauch, and F. Lombardi, Transport properties of ultrathin $YBa_2Cu_3O_{7-\delta}$ nanowires: A route to single-photon detection, Phys. Rev. B **96**, 064525 (2017).

[27] S. Nawaz, R. Arpaia, F. Lombardi, and T. Bauch, Microwave response of superconducting $YBa_2Cu_3O_{7-\delta}$ nanowire bridges sustaining the critical depairing current: Evidence of Josephson-like Behavior, Phys. Rev. Lett. **110**, 167004 (2013).

[28] E. Trabaldo, R. Arpaia, M. Arzeo, E. Andersson, D. Golubev, F. Lombardi, and T. Bauch, Transport and noise properties of YBCO nanowire based nanoSQUIDs, Supercond. Sci. Technol. **32**, 073001 (2019).

[29] E. Trabaldo, S. Ruffieux, E. Andersson, R. Arpaia, D. Montemurro, J. F. Schneiderman, A. Kalaboukhov, D. Winkler, F. Lombardi, and T. Bauch, Properties of grooved Dayem bridge based $YBa_2Cu_3O_{7-\delta}$ superconducting quantum interference devices and magnetometers, Appl. Phys. Lett. **116**, 132601 (2020).

[30] H. Ma, H. Wang, Y. Wang, Z. Luo, Z. Li, Y. Wang, X. Du, C. Yang, J. Huang, C. Wu, N. Li, X. Wang, Y. Liu, and P. Li, Minimal Damage and Tunable Fabrication of Atomic-Scale Ultrathin $YBa_2Cu_3O_{7-\delta}$ Nanowires with High Uniformity, Small Struct. **6**, 2400661 (2025).

[31] K. Xu and J. R. Heath, Long, Highly-Ordered High-Temperature Superconductor Nanowire Arrays, Nano Lett. **8**, 3845 (2008).

[32] S. K. H. Lam, A. Bendavid, and J. Du, Hot spot formation in focused-ion-beam-fabricated $YBa_2Cu_3O_{7-x}$ nanobridges with high critical current densities, Nanotechnology **30**, 325301 (2019).

[33] M. Lyatti, M. A. Wolff, A. Savenko, M. Kruth, S. Ferrari, U. Poppe, W. Pernice, R. E. Dunin-Borkowski, and C. Schuck, Experimental evidence for hotspot and phase-slip mechanisms of voltage switching in ultrathin $YBa_2Cu_3O_{7-x}$ nanowires, Phys. Rev. B **98**, 054505 (2018).

[34] V. Rouco, D. Massarotti, D. Stornaiuolo, G. P. Papari, X. Obradors, T. Puig, F. Tafuri, and A. Palau, Vortex Lattice Instabilities in $YBa_2Cu_3O_{7-x}$ Nanowires, Materials **11**, 211 (2018).

[35] C. H. Wu, W. S. Kuo, F. J. Jhan, J. H. Chen, and J. T. Jeng, A Nanoscale-Localized Ion Damage Josephson Junction Using Focused Ion Beam and Ion Implanter, J. Nanosci. Nanotechnol. **15**, 3728 (2015).

[36] H. Hilgenkamp and J. Mannhart, Grain boundaries in high-T_c superconductors, Rev. Mod. Phys. **74**, 485 (2002).

[37] J. Nagel, K. B. Konovalenko, M. Kemmler, M. Turad, R. Werner, E. Kleisz, S. Menzel, R. Klingeler, B. Büchner, R. Kleiner, and D. Koelle, Resistively shunted $YBa_2Cu_3O_7$ grain boundary junctions and low-noise SQUIDs patterned by a focused ion beam down to 80 nm linewidth, Supercond. Sci. Technol. **24**, 015015 (2011).

[38] S. Cybart, R. Bali, G. Hlawacek, F. Röder, and J. Fassbender, Focused Helium and Neon Ion Beam Modification of High-T_c Superconductors and Magnetic Materials, in *Helium Ion Microscopy*, edited by G. Hlawacek and A. Gölzhäuser (Springer International Publishing, Cham (Switzerland), 2016) Chap. 17, pp. 415–455.

[39] W. Lang, M. Dineva, M. Marksteiner, T. Enzenhofer, K. Siraj, M. Peruzzi, J. D. Pedarnig, D. Bäuerle, R. Korntner, E. Cekan, E. Platzgummer, and H. Loeschner, Ion-beam direct-structuring of high-temperature superconductors, Microelectron. Eng. **83**, 1495 (2006).

[40] I. A. Zaluzhnyy, U. Goteti, B. K. Stoychev, R. Basak, E. S. Lamb, E. Kisiel, T. Zhou, Z. Cai, M. V. Holt, J. W. Beeman, E. Y. Cho, S. Cybart, O. G. Shpyrko, R. Dynes, and A. Frano, Structural changes in $YBa_2Cu_3O_7$ thin films modified with He^+-focused ion beam for high-temperature superconductive nanoelectronics, ACS Appl. Nano Mater. **7**, 15943 (2024).

[41] S. A. Cybart, E. Y. Cho, T. J. Wong, B. H. Wehlin, M. K. Ma, C. Huynh, and R. C. Dynes, Nano Josephson superconducting tunnel junctions in $YBa_2Cu_3O_{7-\delta}$ directly patterned with a focused helium ion beam, Nat. Nanotechnol. **10**, 598 (2015).

[42] B. Müller, M. Karrer, F. Limberger, M. Becker, B. Schröppel, C. J. Burkhardt, R. Kleiner, E. Goldobin, and D. Koelle, Josephson junctions and SQUIDs created by focused helium-ion-beam irradiation of $YBa_2Cu_3O_7$, Phys. Rev. Appl. **11**, 044082 (2019).

[43] M. Karrer, K. Wurster, J. Linek, M. Meichsner, R. Kleiner, E. Goldobin, and D. Koelle, Temporal evolution of electric transport properties of $YBa_2Cu_3O_{7-\delta}$ Josephson junctions produced by focused-helium-ion-beam irradiation, Phys. Rev. Appl. **21**, 014065 (2024).

[44] M. Pröpper, D. Hanisch, C. Schmid, P. J. Ritter, M. Neumann, E. Goldobin, D. Koelle, R. Kleiner, M. Schilling, and B. Hampel, THz properties of He-FIB $YBa_2Cu_3O_{7-x}$ Josephson junctions, IEEE Trans. Appl. Supercond. **34**, 1 (2024).

[45] E. Y. Cho, Y. W. Zhou, J. Y. Cho, and S. A. Cybart, Superconducting nano Josephson junctions patterned with a focused helium ion beam, Appl. Phys. Lett. **113**, 022604 (2018).

[46] E. Y. Cho, H. Li, J. C. LeFebvre, Y. W. Zhou, R. C. Dynes, and S. A. Cybart, Direct-coupled micro-magnetometer with Y-Ba-Cu-O nano-slit SQUID fabricated with a focused helium ion beam, Appl. Phys. Lett. **113**, 162602 (2018).

[47] H. Li, E. Y. Cho, H. Cai, Y.-T. Wang, S. J. McCoy, and S. A. Cybart, Inductance investigation of $YBa_2Cu_3O_{7-\delta}$ nano-slit SQUIDs fabricated with a focused helium ion

beam, IEEE Trans. Appl. Supercond. **29**, 1 (2019).

[48] C. Schmid, A. Jozani, R. Kleiner, D. Koelle, and E. Goldobin, $YBa_2Cu_3O_7$ Josephson diode fabricated by focused-helium-ion-beam irradiation, Phys. Rev. Appl. **24**, 014041 (2025).

[49] M. Schilling, A. Guillaume, J. M. Scholtyssek, and F. Ludwig, Design of experiments for highly reproducible pulsed laser deposition of $YBa_2Cu_3O_{7-\delta}$, J. Phys. D: Appl. Phys. **47**, 034008 (2013).

[50] N. Sarkar and S. A. Cybart, Design Rules for Resistors, Capacitors and Inductors Fabricated From Single Layer Y-Ba-Cu-O Thin Films With Focused Helium Ion Beam Irradiation, IEEE Trans. Appl. Supercond. **33**, 1 (2023).

[51] J. Lesueur, L. Dumoulin, S. Quillet, and J. Radcliffe, Ion-beam induced metal insulator transition in YBCO films, J. Alloys Compd. **195**, 527 (1993).

[52] M. Pröpper, D. Hanisch, C. Schmid, M. Neumann, P. J. Ritter, M.-A. Tucholke, E. Goldobin, D. Koelle, R. Kleiner, M. Schilling, and B. Hampel, High-T_c Josephson junction arrays fabricated by He-FIB, IEEE Trans. Appl. Supercond. **35**, 1 (2025).

[53] J. Bardeen, Critical Fields and Currents in Superconductors, Rev. Mod. Phys. **34**, 667 (1962).

[54] Effective area A_{eff} is calculated as fluxoid $\tilde{\Phi}$ induced around the SQUID hole (output of the simulation) divided by the applied field B (input parameter), *i.e.*, $A_{\text{eff}} = \tilde{\Phi}/B$.

[55] M. Khapaev, A.Yu. Kidiyarova-Shevchenko, P. Magnelind, and M.Yu. Kupriyanov, 3D-MLSI: Software package for inductance calculation in multilayer superconducting integrated circuits, IEEE Trans. Appl. Supercond. **11**, 1090 (2001).

[56] C. D. Tesche and J. Clarke, Dc SQUID: Noise and optimization, J. Low Temp. Phys. **29**, 301 (1977).

[57] R. Behr, O. Kieler, J. Kohlmann, F. Müller, and L. Palafox, Development and metrological applications of Josephson arrays at PTB, Meas. Sci. Technol. **23**, 124002 (2012).

[58] A. Rüfenacht, N. E. Flowers-Jacobs, and S. P. Benz, Impact of the latest generation of Josephson voltage standards in ac and dc electric metrology, Metrologia **55**, S152 (2018).

[59] M. Tollkühn, P. J. Ritter, M. Schilling, and B. Hampel, THz microscope for three-dimensional imaging with superconducting Josephson junctions, Rev. Sci. Instrum. **93**, 043708 (2022).

[60] P. Ritter, M. Tollkühn, M. Schilling, and B. Hampel, Characterization of Multi-Frequency Emission of Far-Infrared Laser with Josephson Junctions in a THz Microscope, in *IRMMW-THz* (2022) pp. 1–2.

[61] G. De Simoni, C. Puglia, and F. Giazotto, Niobium Dayem nano-bridge Josephson gate-controlled transistors, Appl. Phys. Lett. **116**, 242601 (2020).

[62] W. Lang, I. Puica, M. Peruzzi, K. Lemmermann, J. D. Pedarnig, and D. Bäuerle, Depairing current and superconducting transition of YBCO at intense pulsed currents, Phys. Status Solidi C **2**, 1615 (2005).

Acknowledgements

Now it's done, and I can hardly believe it. I still remember it as if it were yesterday: collecting the data for my master's thesis — all that was left was to write it up.

I didn't know where to go yet, but a PhD — me? No. That changed when Dieter strolled into the office with the offer of a PhD position. One more different challenge before diving into the working life of industry. Reinhold and Dieter gave me the opportunity in their group to pursue the PhD path with self-initiative. Through moments of despair in the lab or the cleanroom, but also moments of joy and success when something finally worked, I was able to learn a great deal and gain valuable experience. Many thanks for the years of support.

Kenny, Christopher, Moritz, Felix, David, Jonathan, Judith, Noor, and Alireza — students who made it possible to pursue the multitude of ideas and possibilities of which my work represents only a part. Students who often supported and enriched me, who contributed greatly to my personal and professional development in collegial teamwork and solution-oriented problem-solving. I learned some valuable lessons for my life. Most of all, you have greatly enriched my path, and I hope I was able to supervise you well on your way in our group.

Over my many years in research, the helium ion microscope was definitely my constant companion. Without the care of the instrument scientists Ronny and Markus, it would have turned into nothing but a pile of problems after a few years. With PLD, ESV, sputtering and etching systems, Ga-FIB, SEM, AFM, XRD, µMLA, Dektak, and many more, you enabled me to acquire the skills to fabricate, characterize, and pattern my samples independently. Thank you very much for your enduring patience and willingness to help.

My thanks also go, of course, to my colleagues, some of whom have become friends beyond work. Thank you for sharing experience and knowledge, for valuable tips and innovative ideas, and for the warm way we treated each other. A special thanks goes to Kenny, Farnaz, and Edward, who took the time at the end of my work to give my dissertation its final polish. The family-like atmosphere among us often saved me from discouraging phases of research and is by no means something to be taken for granted. Through welcome distractions while enjoying a birthday cake, an after-work beer at a barbecue, or abshaken at a Clubhaus party, I experienced beautiful moments with you. These are all memories I look back on full of joy.

Last but not least, I would like to thank everyone outside of my working life who enriches my life day after day and provides the balance I need alongside my work — my dear friends, my dear family. Thank you for your psychological and moral support.
I'm glad to have you in my life.